m Anno 2008_Numero 01

miscellanea INGV

Unità Funzionale Gravimetria e Magnetismo
Sezione di Catania - INGV

2006 Annual Report

01

Istituto Nazionale di
Geofisica e Vulcanologia

Anno 2008_Numero 01

miscellanea INGV

UNITÀ FUNZIONALE GRAVIMETRIA E MAGNETISMO
SEZIONE DI CATANIA – INGV
2006 ANNUAL REPORT

Gennaro Budetta, Daniele Carbone, Alessia Ciraudo, Gilda Currenti, Ciro Del Negro, Gaetana Ganci, Salvatore Giudice, Filippo Greco, Alexis Herault, Rosalba Napoli, Danila Scandura, Antonino Sicali, Annamaria Vicari

INGV (Istituto Nazionale di Geofisica e Vulcanologia, Sezione di Catania)

01

This report is part of a monograph series of activity reports being prepared by the *Unità Funzionale Gravimetria e Magnetismo (UFGM)* of the INGV-Catania. Considered preliminary, these reports are subject to revision as new data become available.

SUGGESTIONS FOR READERS

Readers who want a broader overview of volcano geophysics at the Mount Etna and Stromboli Island are encouraged to consult the references cited at the end of this report. Additional information about the main active Sicilian volcanoes can be obtained by visiting the Sezione di Catania - INGV Web site (URL: <http://www.ct.ingv.it>).

Cover photograph: South-East Crater of Mt Etna on 19 July 2006 (courtesy of Filippo Greco, INGV-CT).

CONTENTS

FOREWORDS

The *Unità Funzionale Gravimetria e Magnetismo (UFGM*) is a division of the Istituto Nazionale di Geofisica e Vulcanologia (*INGV*) – Sezione di Catania. The *UFGM* was established in 2001. The *Division* is focused on the quantitative interpretation of gravity, magnetic and electrical data in volcano geophysics and the development of mathematical models of volcanic processes for hazard assessment.

It relies upon the expertise gained during recent volcanic unrests in Sicily, as well as upon the most efficient resource allocation coming out from more and more closely integrated and coordinated activity planning.

It originates from the fact that the *Volcanology* has become increasingly quantitative evolving from an empirical to a more quantitative approach in the study of eruptive phenomena.

It derives from the need of devising elaborated mathematical models to track the spatial and temporal evolution of volcanic processes based on geophysical observations.

The *UFGM* has the mission to gather new information about volcanic processes, integrate this information into a comprehensive and predictive understanding of eruptive phenomena, and communicate this understanding in order to increase volcanic eruptions awareness.

The *UFGM* contributes, together to the other *Divisions* of *INGV-Sezione di Catania*, to the work of *Civil Protection* authorities to enhance a common strategy to fight volcanic threat. Within a multidisciplinary context and capitalizing on previous and ongoing research, it aims to improve volcanic risk assessment and management capacities in active volcanic regions.

Logo of the *Unità Funzionale Gravimetria e Magnetismo* (*UFGM*).

The plans for the future are the development of new methodologies, risk criteria, protocols, procedures and scenarios to evaluate and manage volcanic hazards and risks. It is the task of the *UFGM* to improve tools and prevention methods useful for end users such as territorial planning, innovative risk mapping and help the development of mitigation guidance.

The intention of the *UFGM* is also to provide a connection between basic research at the university and the practical applications of the results. Therefore, the close cooperation with the *University of Catania* is especially important for intensifying the research and training of excellent PhD students and extending our European activities by new cooperation projects.

Now we would like to wish you a pleasant reading of our annual report. Please feel free to contact us if you are interested in any of our new projects, or talk to us about proposals of a possible cooperation. We are always open to any new ideas and suggestions.

Head of Division:

Ciro Del Negro
Phone +39 095 716 58 23
Email: delnegro@ct.ingv.it

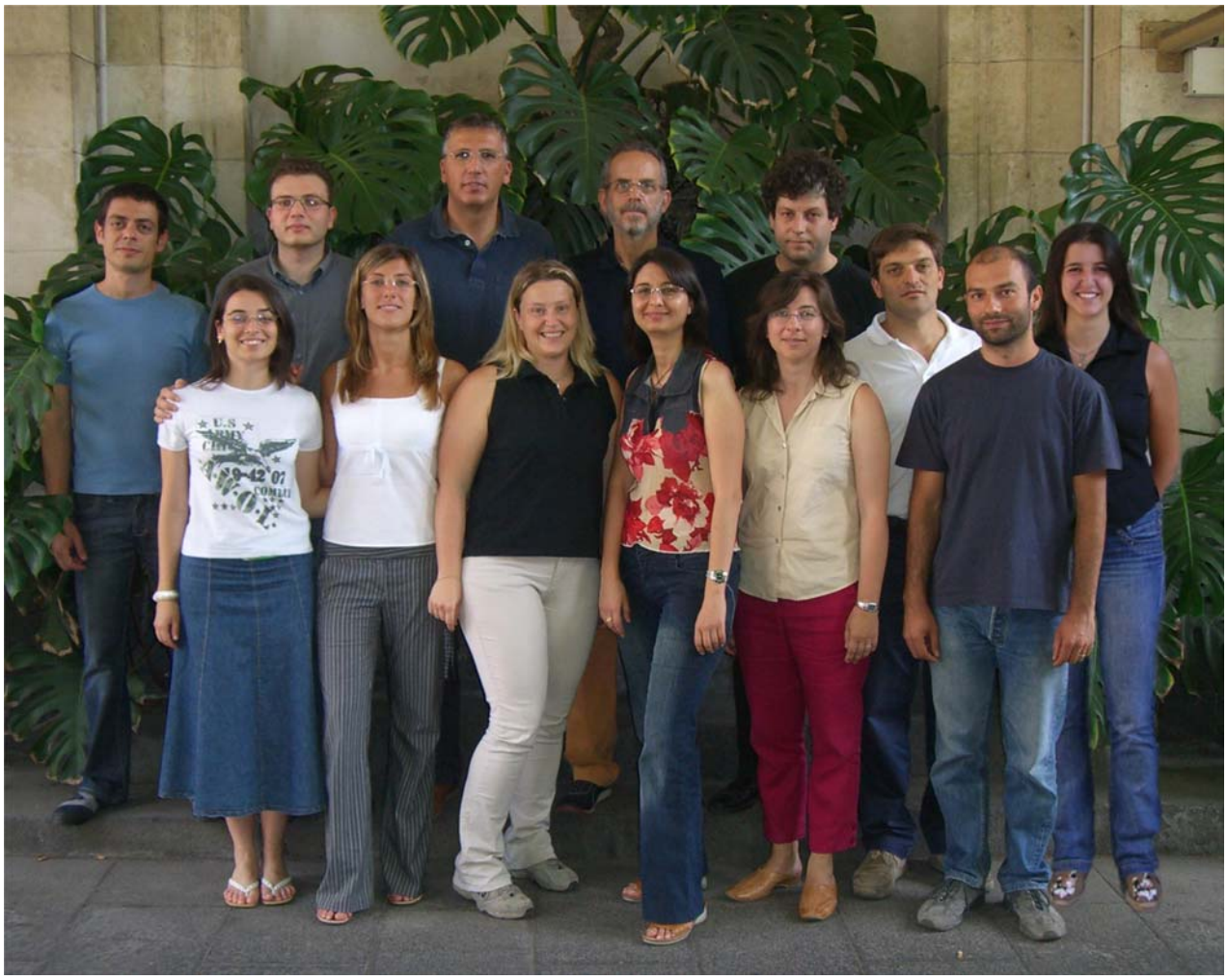

UFGM people: Daniele Carbone, Alessia Ciraudo, Salvatore Giudice, Gaetana Ganci, Ciro Del Negro, Annamaria Vicari, Gennaro Budetta, Gilda Currenti, Rosalba Napoli, Alexis Herault, Filippo Greco, Antonino Sicali, Danila Scandura.

INTRODUCTION

The *Unità Funzionale Gravimetria e Magnetismo (UFGM*) is dedicated to improve the efficiency of gravity and magnetic monitoring networks, to better the capacity of predicting unrests through the observation and interpretation of complete sets of geophysical parameters, and to develop innovative methods for simulation and modelling techniques useful for volcano hazard assessment.

The volcano eruptions create some of nature's most dramatic displays. Depending on their magnitude and location, they also have the potential for becoming major social and economic disasters. In the face of these dangers, the *UFGM* keeps track of the status of main active volcanoes in Sicily.

Sight from south of Mt Etna on 22 December 2006.

This is a complex task that starts with fundamental research on the processes controlling the way volcanoes erupt. Research provides the basic concepts that underlie the various methods of volcano data collection and interpretation. The oversight continues with three operational components: *assessment* of hazard based on past history, *monitoring* of early warning signals that can indicate incipient eruptions, and design of *crisis response* strategies when large eruptions take place. A final *outreach* stage is necessary to inform civil defense officials and the public at large about the risks they face from volcanoes.

South-East crater at Mt Etna on 05 September 2006.

The primary areas of application of the *UFGM* include the *Applied Research*, the *Volcano Monitoring* and the *Hazard Mitigation*.

The extraordinary breadth of *UFGM* reflects the interdisciplinary approaches required to understand complex systems like the volcanoes. The diverse expertise of researchers in different geophysical methods is brought together and is addressed towards advancing the state of art in interpretation of complete sets of geophysical data for volcanological problems.

Valle del Bove at Mt Etna on 12 November 2006.

One of the main tasks of *Volcano Geophysics* is to reveal quantitatively the structure and dynamics of the volcanoes. In this task field measurements are the starting point. However, field data alone are not enough for making any quantitative interpretation, but in addition

theoretical responses (model responses) are needed and for realistic volcano models they are obtained by numerical modeling. And finally, by examining together field data and model data, the quantitative statement of the structure and dynamics of the volcanoes can be made by solving the geophysical inverse problem. This makes numerical modeling and inversion so important and basic area in geophysical research.

Mathematical models have become key tools, not only to forecast the dynamic of the volcanic activity, but also to interpret a wide variety of geophysical observations, which have provided further insights into the complex dynamics of eruptive processes. *Computer simulations* make complex processes easier to comprehend, and invisible relations become visible. Expensive and time-consuming experiments can be substituted by simulations.

Effusive vent on the flank of the South-East crater at Mt Etna on 26 October 2006.

Geophysical properties of volcanoes have a wide range of spectrums and time scales that require a variety of instruments and techniques for their study. Only the integrated instruments and techniques can yield a complete and reliable information on those properties, which would then lead to a better understanding of volcanic activities and mechanisms of eruptions.

The *UFGM* has evolved an interdisciplinary approach, developing new measurement techniques and integrating field and remotely sensed observations with physical modeling to improve our understanding of magma plumbing systems and conduit dynamics, and of the environmental impact of volcanic activity.

The unifying aim is to understand fundamental processes controlling the timing and vigor of eruptions that occur in the shallow parts of volcanic plumbing systems, using:

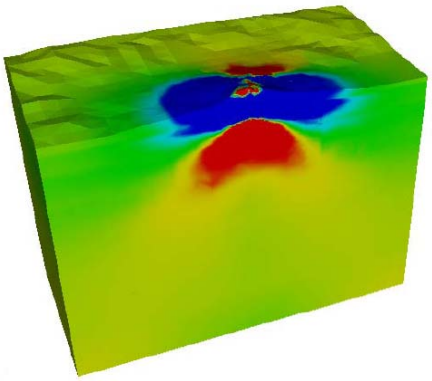

Static stress change due to an intrusive dike computed using a Finite Element Model.

- The *continuous geomagnetic studies* as an effective volcano-monitoring tool. The magnetic data not only allowed the timing of intrusive events to be described in greater detail but also, together with other volcanological and geophysical evidences, permitted some constraints to be set on the characteristics of propagation of shallow dikes.

- *Gravity monitoring* of active volcanoes. The development of microgravity for volcano monitoring has contributed substantially to both eruption prediction and our understanding of magmatic processes.

- Studies on *stress interaction* between magmatic intrusions and tectonic processes. The calculate of the variations in the Coulomb stress at Etna supplied a quantitative esteem of the reactivation of the main seismogenetic structures.

- *Lava flow modeling*. Simulations of lava emplacement processes have established new criteria for predicting lava flow morphology based on their eruption rates and physical properties.

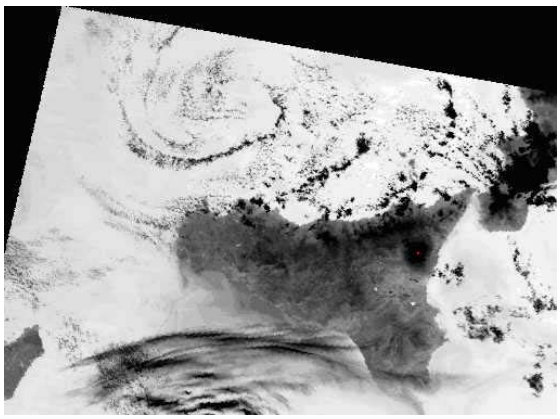

Satellite imagine on 26 October 2006.

- *Remote sensing*. The *UFGM* encompasses expertise in remote sensing used to extract information about ongoing eruptions, particularly using thermal infrared to identify phenomena during real-time monitoring, to quantify eruption rates, and to determine lava tunnels.

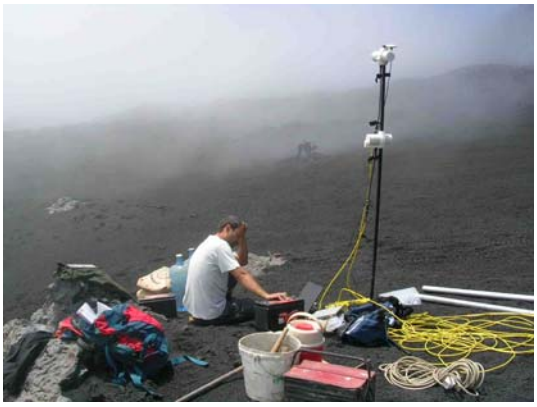

Preliminary gradiometric measurements for choosing a new magnetic site on Mt Etna.

In 2006, the organization of the *UFGM* was consolidated and strengthened around existing three *Laboratories* and three *Working Groups*.

The *UFGM* makes use of the *Laboratory of Gravimetry* (*GravLab*) and the *Laboratory of Geomagnetism* (*MagLab*) for the development and management of gravimetric, magnetic and electric monitoring networks of the main active volcanoes in Sicily (Etna and Stromboli), and of the *Laboratory of Technologies and Dynamic Systems for the Volcanoes Geophysics* (*TecnoLab*), for the enhancing of research and training of excellent PhD students working full-time in the volcano monitoring.

At present, the monitoring systems working at *Mt Etna* consist of (i) a gravimetric network composed of 71 benchmarks for discrete measurements and 3 continuously running remote controlled stations, (ii) a network of 9 scalar and 2 vector magnetometers and (iii) a geoelectrical network comprising 4 stations for measuring self-potential signals. At the moment it is operating in *Stromboli Island* a network of 3 magnetic gradiometers, 1 continuously running gravimeter and 1 station for measuring self-potential signals. These devices allowed to observe and evaluate in near real time the modifications of typology and activity level of gravimetric and magnetic fields at *Mt Etna* during the 2001, 2002, 2004 and 2006 eruptive events and at *Stromboli Island* during the 2002-03 eruption.

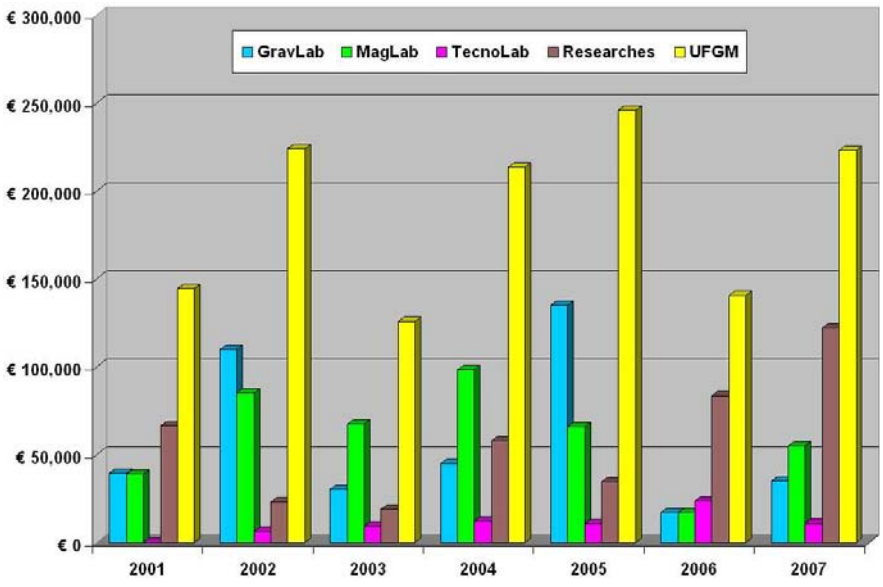

Operating budget development from 2002 to 2007.

Within the *UFGM* structure, the *Working Groups* (*WGs*) are responsible for coordinating interdisciplinary activities in three major areas of research: (i) identification and characterization of precursor signals (*Analysis Working Group*), (ii) modeling of pre-eruptive processes by using multiparameter data (*Modeling Working Group*), and (iii) numerical simulation and hazard assessment of eruptive phenomena (*Simulation Working Group*). The *WGs* are the crucibles for the interdisciplinary synthesis that lies at the core of *UFGM*'s mission.

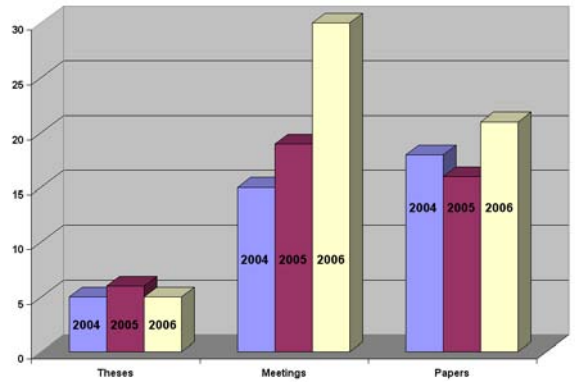

Development of publications from 2004 to 2006.

Budget and Personnel development

The year 2006 was a year of confirmed continuity at high level for the *UFGM* at INGV-Catania, it again brought significant growth with respect to personnel, researches, and publications. However, the operating budget of the UFGM has drastically decreased in 2006 with respect to the last years. As already expected, there was a sharp reduction of the investments for monitoring activity. Nevertheless, bottom appears to have been touched by now. Already now, considerable growth rates for 2007 have been secured.

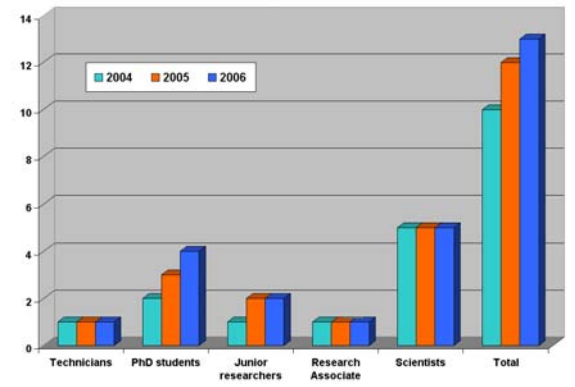

Personnel development at the *UFGM*.

In 2006, 13 colleagues were working at the *UFGM*, among who were 5 scientists, 2 junior researchers, 1 research associate and 1 technician. Additionally, there were 4 PhD students, a fact which shows that the support of young scientists has remained exemplary, especially in cooperation with the Departments of Engineering and Mathematics of the University of Catania. Our productivity coefficient was 1.75.

In September 2006, the *UFGM* organized the Workshop on gravity, magnetic, electric and electromagnetic methods in seismology and volcanology (*MGMEESV*) in Catania. At least 90 scientists accepted our invitation. They have given an additional impetus to establishment of a regular inter-association forum for comprehensive study of seismic and volcanic phenomena by potential field methods. Interesting insights into their new research areas were offered, and of course an intensive exchange of ideas took place. We plan to turn this meeting into a permanent event.

Talk during of the MGMEESV Workshop.

Purpose and scope

This report summarizes the volcano monitoring and research developed by our *Laboratories* and *Working Groups* during 2006. *Monitoring* is focused on the time changes of local gravimetric and magnetic fields which occurred at Etna and Stromboli. A methodology for the compilation of a new kind of map showing the hazard related to lava invasion in predefined study areas of Etna volcano is also presented. *Research* includes the last advances in (i) the noise reduction in gravity and geomagnetic time series using multivariate methods, (ii) the joint modeling of interdisciplinary geophysical data in a viscoelastic medium, and (iii) the near-real-time forecasting of lava flow hazards: using infrared satellite data to drive cellular automata flow simulations.

If you have any comments or questions regarding our research, publications, or software, please contact any member of the division.

Contact:

Gennaro Budetta
Phone +39 095 716 58 27
Email: budetta@ct.ingv.it

MONITORING ACTIVITY

The primary focus of *UFGM* monitoring activities is to investigate the dynamics of the volcanoes and to mitigate the effects of paroxysmal events. The forces and processes acting before, during, and after eruptions are highlighted through the study of gravity and magnetic anomalies, as well as other geophysical indicators.

Field areas spread throughout the main active Sicilian volcanoes. Within *INGV-Catania*, we work closely with specialists in tectonics, geodesy, geochemistry, and seismology to solve recalcitrant problems. We also take advantage of our special geographical location: our institute is very close to the objects of our research.

Gravity surveys carried out during 2006 reveal the presence of some small anomalies both in the summit area of the volcano and in the central part of the East-West profile. In the same period, gravity data continuously recorded didn't show any long period anomalies. On the contrary, from the beginning of July gravity sequences recorded at BVD station show anomalies with 2 days period and amplitude of about 20 μGal attributable to sub-superficial mass redistributions

Between January and April 2006, a slow and continuous decrease in the magnetic field total intensity was observed at the CST and BVD stations located on the southern side of the Etna volcano, while at the north an increase of few nanotelas was recorded at BCN and PDG stations. The observed time scale and polarity of the observed anomaly could bring into play the thermomagnetic effect produced by demagnetization of a source located near the summit craters. A variation of this trend, attributable to a change of the source location was observed at all stations in the middle of April. Moreover, at the beginning of November 2006 a large and sharp decrease of the geomagnetic field was detected at the station of MFS which could be of thermomagnetic origin engendered by lava flows emitted by an effusive vent on 6 November, which threatened this station and stopped at about 30 m from the magnetic sensor.

At Stromboli continuously magnetic observations reveal a slow and continuous decrease of about 4 nT at SLN station, whose time scale suggests a thermomagnetic effect induced by the presence of shallow fluids.

Self potential signals recorded both at Etna and Stromboli didn't show any geophysical electromagnetic changes.

More details of these monitoring volcanic activities on *Mount Etna* and *Stromboli Island* are provided below.

Explosive activity at South-East crater of Mt Etna on 24 November 2006.

GRAVITY MONITORING OF ETNA VOLCANO

Gravity network

The Etna gravity network (Fig. 1) covers the volcano edifice at elevations ranging between 450 and 3100 m s.l.m. and is composed of: a) 71 benchmarks for discrete measurements, constitued of 4 integrated subarrays (E-O Profile; Summit Profile; Main Network; Basal Reference Network) and b) 3 continuously recording stations (PDN; BVD; SLN). During the 2006, 16 surveys were carried out (Tab. 1) using the Scintrex CG-3M gravimeter. The surveys were performed, with different sampling frequencies, at all the subarrays of the discrete gravity network (Tab. 1). In July an additional measuring campaign was carried out at eight benchmarks located along the Zafferana - Piano Provenzana line. Only during the campaign performed in June the Scintrex CG-3M gravimeter was calibrated along the Catania – Enna calibration line.

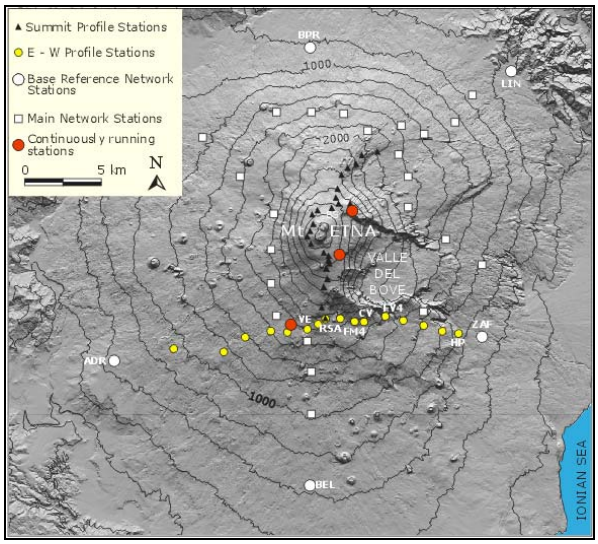

Fig. 1 - Map of Mt Etna showing (a) benchmarks on the Main Network (white squared), (b) the Summit Profile (black triangles), (c) the East-West Profile (yellow circles), (d) the Basal Reference Network (white circles) and (d) the continuously recording gravity stations (red circles).

Main array

Gravity changes during the June 2005 – June 2006 period are shown in the contour map of Figure 2 which integrates data from all the stations of Etna's gravity network. The gravity field is mainly characterized by a positive anomaly centered in the North-East part of the volcano showing a wavelength of about 5 km and amplitude up to 40 μGal. The summit area is moreover affected by a negative gravity anomaly. The most frequently acquired data along the Summit Profile suggest that the negative anomaly centered in the summit craters depends on a general decreasing trend of the gravity field which affects the summit area from 2003.

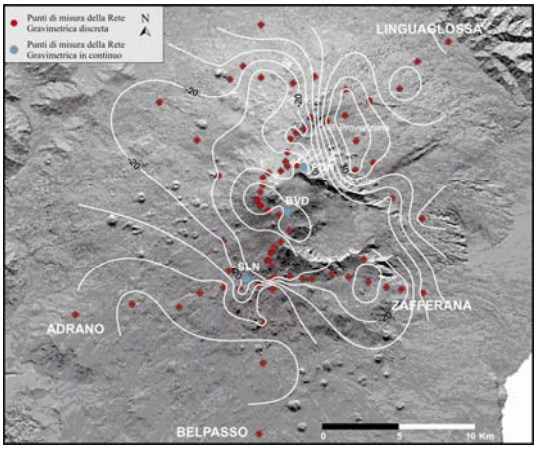

Fig. 2 - Gravity anomalies observed by the main network (at 10 μGal intervals) at Etna during June 2005-June 2006. Gravity measurement error is estimated at ± 20 μGal; a greater measurement error affects the gravity changes along the Summit Profile (± 25 μGal). The most important gravity changes (+ 40 μGal) are observed in the North-East part of the volcano.

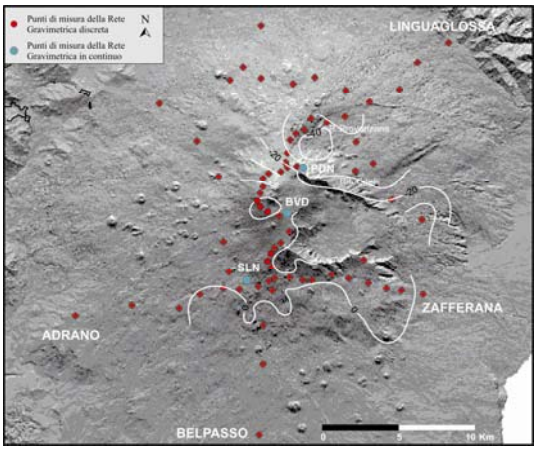

Fig. 3 - Gravity anomalies observed along the East-West Profile, the Summit Profile and the profile from Zafferana to Piano Provenzana (at 10 μGal intervals) at Etna during June 2006-July 2006. Gravity measurement error is estimated at ± 20 μGal; a greater measurement error affects the gravity changes along the Summit Profile (± 25 μGal).

Figure 3 shows the gravity sequences collected by some benchmarks of the network at Mt Etna (E-W, N-S and the profile from Zafferana to Piano Provenzana) between June and July 2006. The only significant variation about the gravity anomaly is the reverse in sign observed in the North-East flank of the volcano between June 2005 and June 2006. No remarkable gravity change is highlighted by the frequently acquired data along the Summit Profile during the following months.

East-West profile (Adrano - Rifugio Sapienza – Zafferana Etnea)

Monthly surveys are carried out along the East-West Profile which runs from Zafferana to Adrano and it's composed by 18 benchmarks. Between March 2006 and December 2006 (period including the eruptive activity), a significant gravity decreasing (-60 µGal) was recorded along the measurement points placed in the central and eastern part of the profile (from TG and FV; Fig. 4).

Period	E-WProfile	Summit Profile	Main Network	Basal Network	Calibration line
March 2006	*				
May 2006	*				
June 2006	*	*	*	*	*
July 2006	*	*			
September 2006	*	*			
October 2006	*	*			
November 2006	*				
December 2006	*				

Tab. 1 - Gravity surveys carried out during 2006 on Etna and along the CT-EN calibration line.

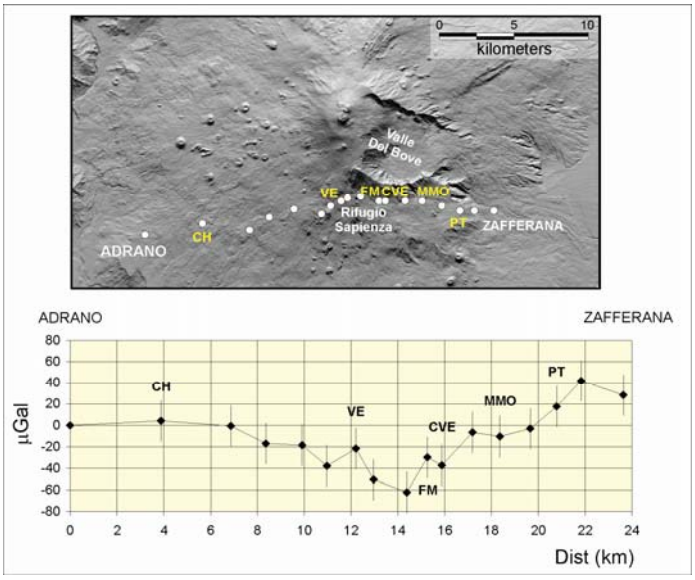

Fig. 4 - Gravity changes observed along the E-W Profile which runs from Zafferana to Adrano between March and December 2006 (error bar ± 20 µGal). The data reported are referred to the Adrano station.

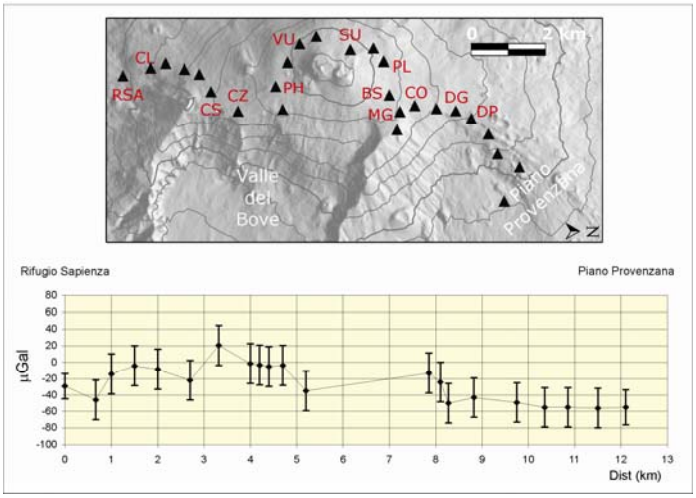

Fig. 5 – Gravity changes observed along the North-South Profile which runs from Piano Provenzana to the Rifugio Sapienza across the summit zone during June-July 2006 time interval (the error along this profile is typically ±15 µGal). All the sequences refer to the Rifugio Sapienza benchmark whose gravity value, in the considered period, is lowered of about 30 µGal. The gravity decreases in the northernmost benchmarks of the profile are also shown.

North South summit profile

No meaningful gravity changes were observed in the last three years along the Etna Summit Profile of 28 benchmarks, arranged along a North-South line runs about 13 km from Piano Provenzana to the Rifugio Sapienza crossing the summit zone. Instead, between June and July 2006 time-interval, a sudden gravity decrease of about -40 µGal centred in the northernmost benchmarks of the profile was observed (as shown in Figure 3). Significant gravity changes of this anomaly did not take place during the surveys carried out in September and October 2006 (Fig. 5).

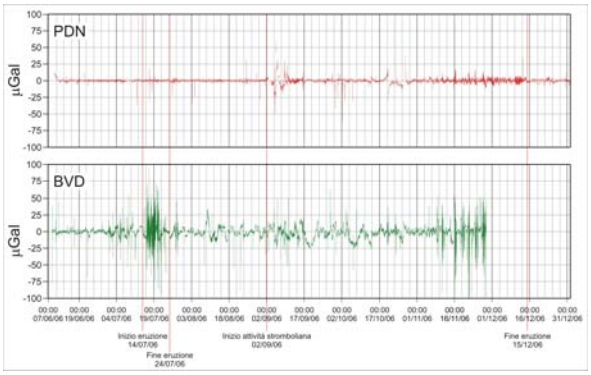

Fig. 6 - Gravity sequences from Pizzi Deneri (PDN, upper plot) and Belvedere (BVD; lower plot) continuous gravity station during 01 June – 31 December 2006 period. The long period components have been removed from both sequences. Since the beginning of July 2007, on BVD gravity signal a component with a period of about 2 days and amplitude of about 20 µGal was observed. The increase of the noise amplitude on both signals highlight the more intense volcanic episodes.

Continuous gravity network

Since June 2006, Pizzi Deneri (PDN) and Belvedere (BVD) continuous gravity stations have been working nearly uninterruptedly.

In Fig. 6 the gravity sequences from PDN and BVD stations during 01 June – 31 December 2006 period, after removing the best linear fit and the Earth tide, are shown. From both sequences, the long period components, affected by the external temperature, have been removed.

Since the beginning of July 2007 (about two weeks before the start of the eruption), on BVD gravity signal (placed about 500 meters from eruptive fissures) a component with a period of about 2 days and amplitude of about 20 µGal was observed. No meaningful gravity changes were observed on 14th of July when the eruption took place. During the same period, the gravity changes observed at PDN station (about 3 kilometers from eruptive fissures) were negligible.

The most evident features on PDN gravity signal are the gravity variations observed during the first half of September, after the beginning of the strombolian activity, and the clear increase of the noise amplitude encompassing the eruption (Fig. 6).

SOURCE	Radius (m)	Volume (m^3)
S1	10	4.000
S2	25	65.000
S3	50	500.000
S4	75	2.000.000
S6	100	4.000.000
Density = 2500 Kg/ m^3		

Table 2 – Gravity effect at BVD and PDN stations due to a spherical source with radius ranging from 10 to 100 meters placed at a variable depth (from 0 to 3000 meters a.s.l.) beneath the eruptive fissure.

Experimentation of Microg LaCoste PET 27 gravimeter

On 18 October a new Microg LaCoste PET 27 gravimeter was installed in Serra La Nave site (SLN). The signal acquired by this new gravimeter showed a high correlation with the most intensive phases of the eruption. Many events until 50 µGal of amplitude were recorded contemporaneously to noise increasing in PDN and BVD signals. In the Figures 8 and 9 two gravimetric events recorded contemporaneously at the three station in the period considered are shown.

Fig. 7 – Multimethod station at Belvedere site on Mt Etna.

Subsequent verifications, among which the employment of a second instrument continuously running in a site near at SLN, showed that the events observed to SLN station are due to instrumental effects, and they are not real gravimetric field variations. The mechanical

system of this instrument is the same of the other instruments working, or that has been worked, on Etna (zero-length spring system). These last never shown this kind of behavior. This means that it is possible to exclude a mechanical system problem of the gravimetric sensor. Two different hypotheses, actually under check, were made.

The first hypothesis regards a bad working of the electronic part (data acquisition system) of the instrument. It is possible that the gravimetric signal can be influenced by the ground inclination signals (and so, it can change its mean level in function of the noise increasing of clinometer signals) and/or other signals sensible to the ground oscillations (i.e. standard deviation of the gravimetric signal). A heavy restructure of the data acquisition system was performed in the early of December.

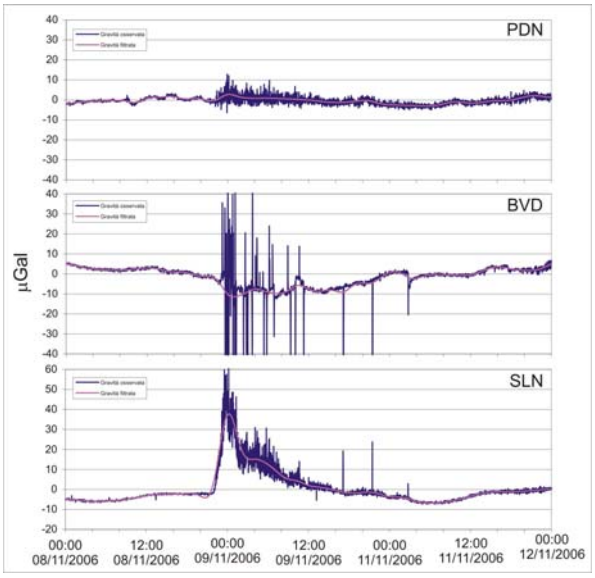

Fig. 8 – Comparison (1datum/minute) between gravimetric signals recorded to PDN (in the top), BVD (in the centre) and SLN (in the bottom) from 00:00 (GMT) of 8 November 2006 to 00:00 (GMT) of 12 November 2006. Data are corrected from the effects of: (a) earth tide; (b) instrumental drift and (c) temperature. Also, in the figure data filtered (violet traces; low-pass filter T= 4 hours) are shown for evidencing only the long period components of the signals.

The second hypothesis regards the possibility that during the preliminary phases of experimentation in Serra La Nave, the instrument was not perfectly in vertical. Effectively, the transport from USA to Italy could have done to change the calibration constants of the two tilt sensors. Due to the complicated geometry of the astatized spring gravimeters, the sensibility of an instrument is influenced by the inclination along the direction of the “long level” and, therefore, it is essential that the instrument is leveled for working correctly. A check performed in the middle of December shown that the calibration constants of clinometer signals were changed. New values of the constants were computed, and the instrument was leveled. The instrument was installed again in SLN. Actually it is in continuous acquiring. The recorded sequences must be analyzed for understanding if the interventions done until now have produced the desired effects.

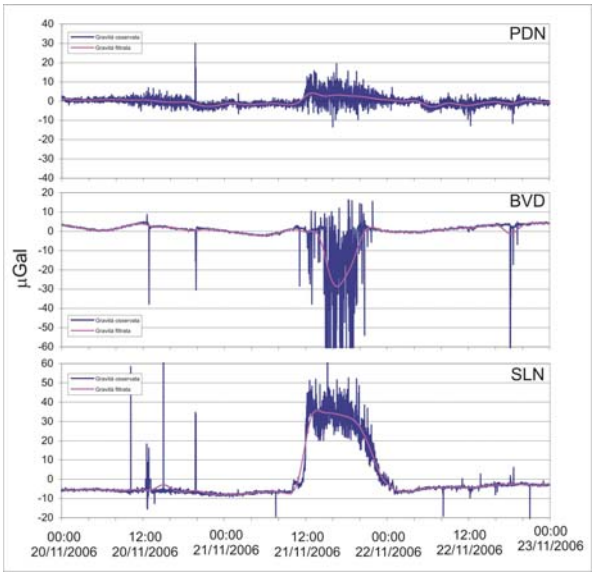

Fig. 9 –Comparison (1datum/minute) between gravimetric signals recorded to PDN (in the top), BVD (in the centre) and SLN (in the bottom) from 00:00 (GMT) of 20 November 2006 to 00:00 (GMT) of 23 November 2006. Data are corrected from the effects of: (a) earth tide; (b) instrumental drift and (c) temperature. Also, in the figure data filtered (violet traces; low-pass filter T= 4 hours) are shown for evidencing only the long period components of the signals.

Contacts:

Daniele Carbone
Phone +39 095 716 58 25
Email: carbone@ct.ingv.it

Filippo Greco
Phone +39 095 716 58 25
Email: greco@ct.ingv.it

MAGNETIC MONITORING OF ETNA VOLCANO

Magnetic network

During 2006 the magnetic network of Mt. Etna was strengthened combining vectorial magnetometers (resolution of 0.1 nT) with scalar sensors installed at ESL (1700 m a.s.l) and PDN (2870 m a.s.l) magnetic stations (Fig. 1). New magnetometers are at full dynamic; this means that they measure both the variations and the static component.

The double measure of quality should permit a more quantitative treatment of the data and then they make easier the attempt to constrain the source dipole and/or to trace their evolutions in the time. The characterization of these signals can be a useful instrument both for improving the monitoring of active volcanoes as well as developing a greater understanding of the pre-eruptive mechanisms which produce them.

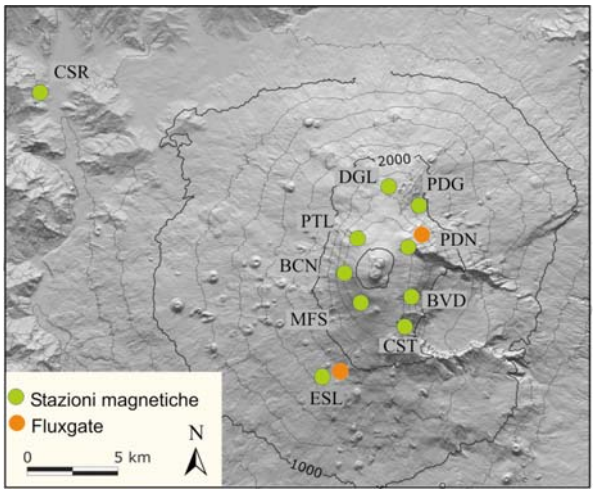

Fig. 1 – Location of the remote stations of the magnetic network of Etna.

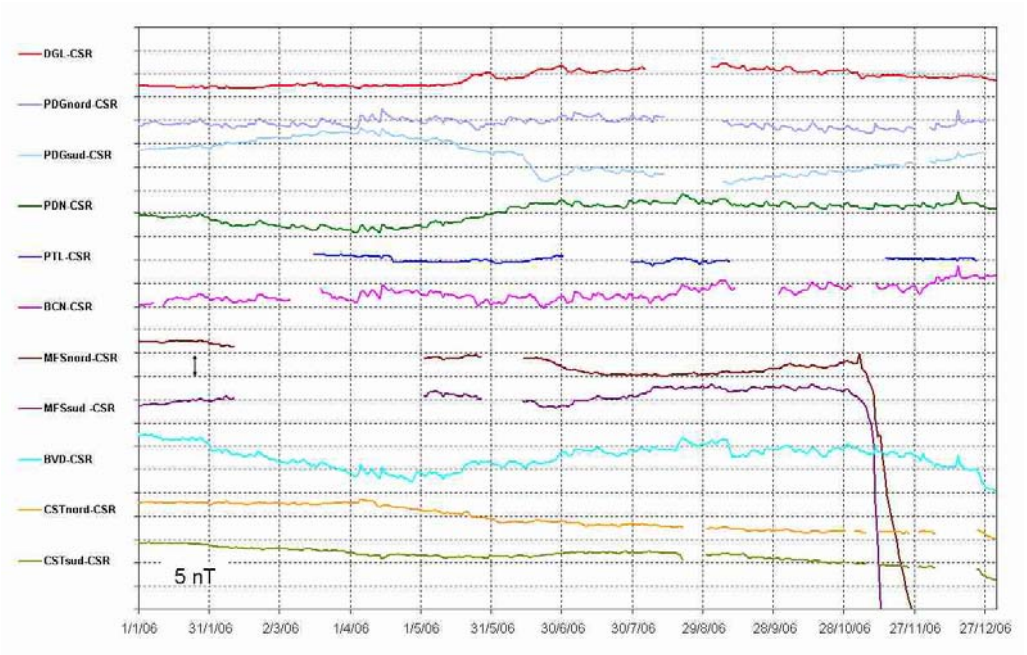

Fig. 2 – Daily mean values of total magnetic field intensity at CST, BVD, MFS, BCN, PTL PDN, PDG and DGL, with respect to CSR station.

Fig. 3 – Maintenance of the BVD station during the 2006 winter.

Magnetic observations

During 2006, the stations of the magnetic network of Etna have worked correctly and with continuity. Only in the stations MFS and PTL the continuity of the measurements has been compromised, respectively, from power supply problems and from the malfunctioning of the magnetometer.

In Fig. 2 the daily mean values of total magnetic field intensity, observed at CST, BVD, MFS, BCN, PTL, PDN, PDG and at DGL are shown. Magnetic field measurements are differentiated with respect to the reference station CSR (Mt. Nebrodi) to isolate local magnetic variations and to cancel common noise due to external sources. Daily averaging of these differentiated data further reduces the standard deviations to less than 1 nT, although in correspondence of strong external activity (geomagnetic K index values more than 5; Fig. 4), the abnormal transient magnetic variations, induced by the different magnetic responses of sites, could be more than 3 nT.

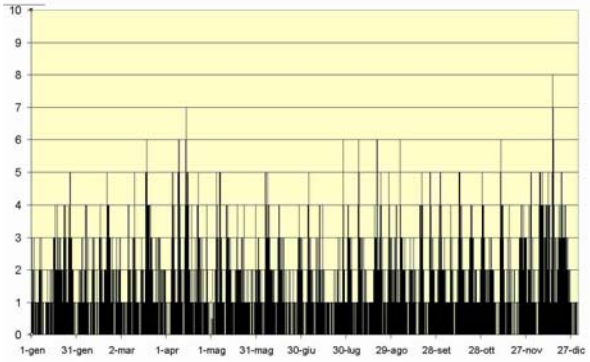

Fig. 4 - Geomagnetic K index values.

Since the beginning of 2006 a constant and continuous decrease of total magnetic field intensity was recorded at CST and BVD stations, instead the BCN and PDG stations show an increase. The observed time scale and polarity of anomaly could bring into play the thermomagnetic effect produced by demagnetization of a source located near the summit craters. This situation is unchanged until the mid April, when a different trend to all stations has been observed. In particular, a reversal trend with an increase of about 5 nT and an increase of the rate variation of - 1,5 nT/month are observed at BVD and CST stations, respectively. Also the variations relationship to the stations isn't constant and, in particular, a change of slope is evident since the 14 April 2006 (Fig. 6). This variation could be explained for a change of the source position.

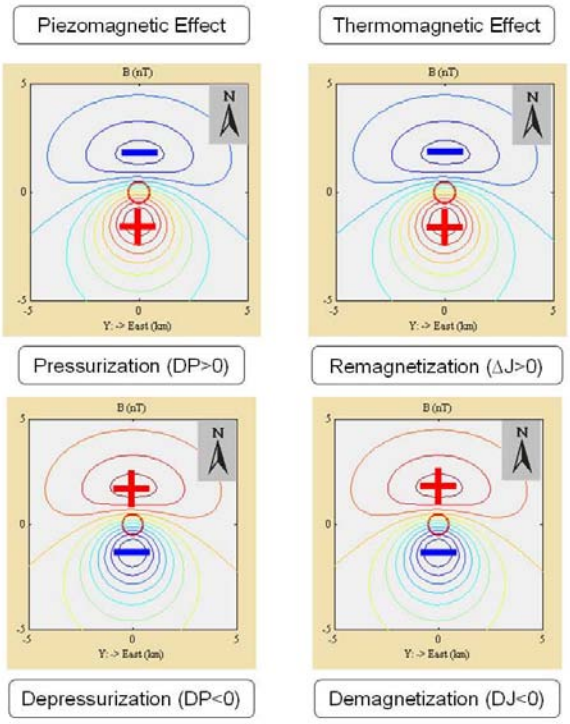

Fig. 5 – Polarity of anomalies produced by piezomagnetic and thermomagnetic effects.

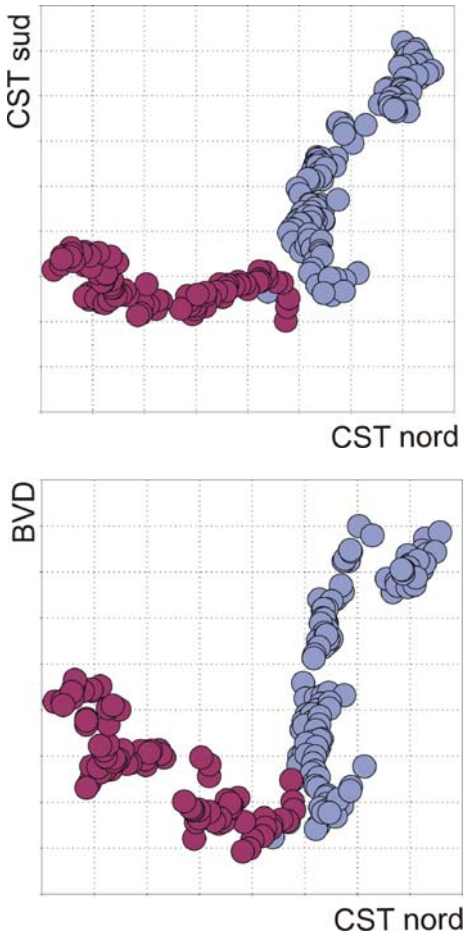

Fig. 6 – Rates of the geomagnetic variations observed at CST and at BVD.

On the basis of the polarity and the amplitude of the observed anomalies at the magnetic stations in April, the source seems to be localized near the SE crater. Indeed the maximum variation of amplitude is observed at BVD (-10nT). Assuming a spherical geometry, it was possible to valuate the source depth by the analysis of the ratio between the variations of the magnetic stations of CST, BCN, MFS in comparison with those observed at BVD. The obtained esteems (Fig. 7) show a depth ranging between 1000 and 1500 m. Moreover, the polarity reversal observed at BVD suggests the establishment of a piezomagnetic phenomena connected to the pressurization of the source.

In the same period the stations located in the northern side show significant variations. In particularly, at the PDG gradiometric station, located near the NE rift, the two sensors show a different behavior. The signal recorded at PDG south shows an increase of about 5 nT from January to April, successively an opposite trend that reach the peach (-0.6 nT/day) between the 13th and the 23rd of June was recorded. Finally, between September and December an increase of about 5 nT was recorded. On the other hand, the PDG north sensor doesn't show significant variations during the whole year. The different behavior of two sensors could be due to the proximity of PDG south to the NE rift structures and to a possible movement of them.

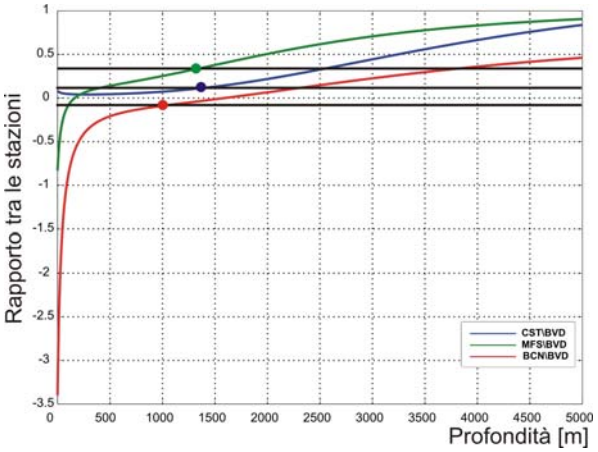

Fig. 7 – Ratios of the geomagnetic variations observed (circles) and calculated (lines) at the CST, MFS and BNC as a function of the source depth.

From the end of January till mid June also PDN shows an anomaly trend in comparison to the long period variations attributed to seasonal phenomena and in comparison to the trend of 2005, while the DGL station, located about 2 km far doesn't show significant variations.

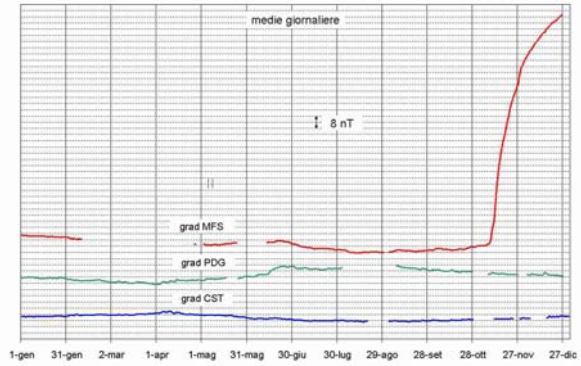

Fig. 8 – Variations of the magnetic gradients at CTS, MFS and PDG from January to December 2006.

Considerations

At last, it is worth noting the strong variation observed from the 6th of November at MFS. Both the sensors of the station record a quick and continuous decrease of the total magnetic field intensity, with variation rate of -10 nT/day for MFS south sensor, and of -4 nT/day for the MFS north sensor. The phenomena, had reached a maximum variation of about -250nT and -100 nT respectively at MFS south and MFS north (Fig. 8). The observed time scale could be probably caused to the thermomagnetic effect produced from the demagnetization due to the lava flow emitted, from the first hours of the 6th of November, to the effusive vent located at 3050 m. Lava flow stops at about 50 meters from MFS south.

Contacts:

Rosalba Napoli
Phone +39 095 716 58 24
Email: napoli@ct.ingv.it

Antonino Sicali
Phone +39 095 716 58 49
Email: sicali@ct.ingv.it

SELF-POTENTIAL MONITORING OF ETNA VOLCANO

Potential field investigations of volcanic unrest

Volcanic unrest is thought to be triggered by the arrival of new magma into a subsurface region. But not all unrest periods have culminated in a volcanic eruption and it may be that aqueous fluid migration at depth results in similar signals. Therefore, the problem is how to discriminate signals from magma movement from signals originating from fluid flow and thus to assess the likelihood of an impending eruption and related hazards. Processes such as magma migration and emplacement, tectonic and hydrothermal activity can trigger seismicity, ground deformation, thermal variations and changes in the potential fields around a volcano. Unrest can be the first sign of the reactivation of a volcanic system, which may lead into eruption. However, the sub-surface beneath active volcanoes is complex and identifying the causative source of unrest is not straightforward.

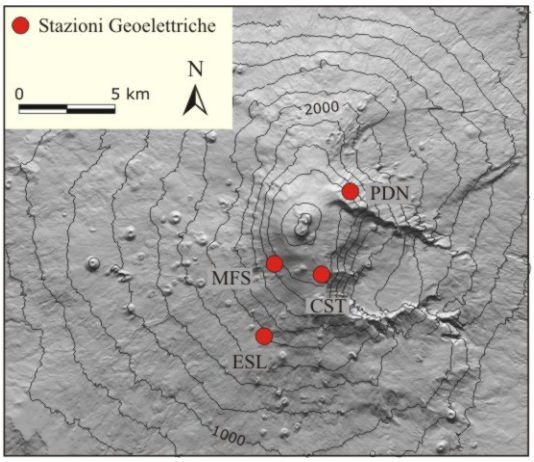

Fig. 1 - Location of the 4 remote stations of the electrical network of Etna.

Over the last years, several geoelectrical methodologies have been applied for studying and monitoring a wide variety of volcanic phenomena. Recent studies revealed that self-potential (SP) anomalies (up to some hundreds of mV) are observed on active volcanic areas, suggesting that the SP anomalies are likely related to thermoelectric and electrokinetic processes due to hydrothermal circulations.

SP studies can be appropriate for monitoring the thermal and hydrothermal states of volcanoes. Therefore, we aim at investigating unrest by quantifying changes in the potential field via the combination of self-potential, gravimetric and magnetic investigations. The combination of these techniques enables the quantification of mass and density changes in the subsurface in addition to changes in the electric properties of the ground. Moreover, continuous SP time series data will shed light on high frequency changes.

Electrical network

A new geoelectrical monitoring network has been installed on Etna volcano in October 2004. The remote stations are equipped with an unpolarizable multi-electrodes (Pb-$PbCl_2$) array to detect the time variation of SP along at least two perpendicular directions. The configuration dipole allows evaluating the electric field irrotationality by calculating the algebraic sum of the measures carried out on the channels to remove every offset caused by the measurement residual errors.

During 2006, the electrical network of Etna (Fig. 1) have worked with regularity. The measurement points are constituted by five Pb-$PbCl_2$ pipe non-polarizing electrodes are buried at 0.5 m depth. The measuring dipoles, 50 and 100 m long, are orthogonally oriented along NS and EW directions (Fig. 2). By this dipole arrangement, noise from electrode instability, rain fall and nearby sources can be detected. The sample rate is generally 5 minutes.

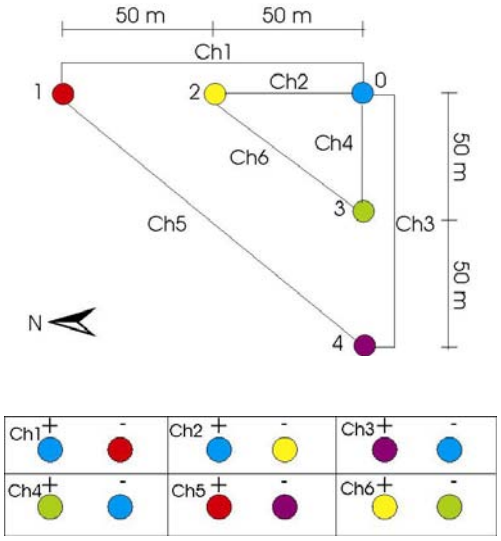

Fig. 2 – Dipole scheme of the SP stations.

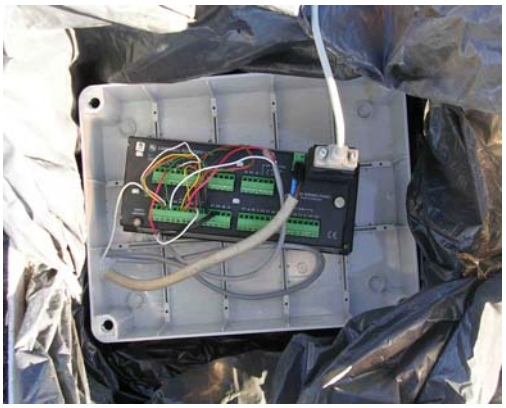

Fig. 3 – Data logger used in SP stations.

Measurements of Self Potential

Signals recorded from January to November 2006 are shown in Fig. 4. The natural fluctuations are reduced applying a time variant non-stationary approach. This technique is based on a predictive analysis which allows for evaluating time variant statistical parameters. The technique has already been tested, successfully, for the magnetic signals and permits to identify possible electromagnetic changes related to seismic and volcanic events. However, from a preliminary analysis no significant anomalies were observed.

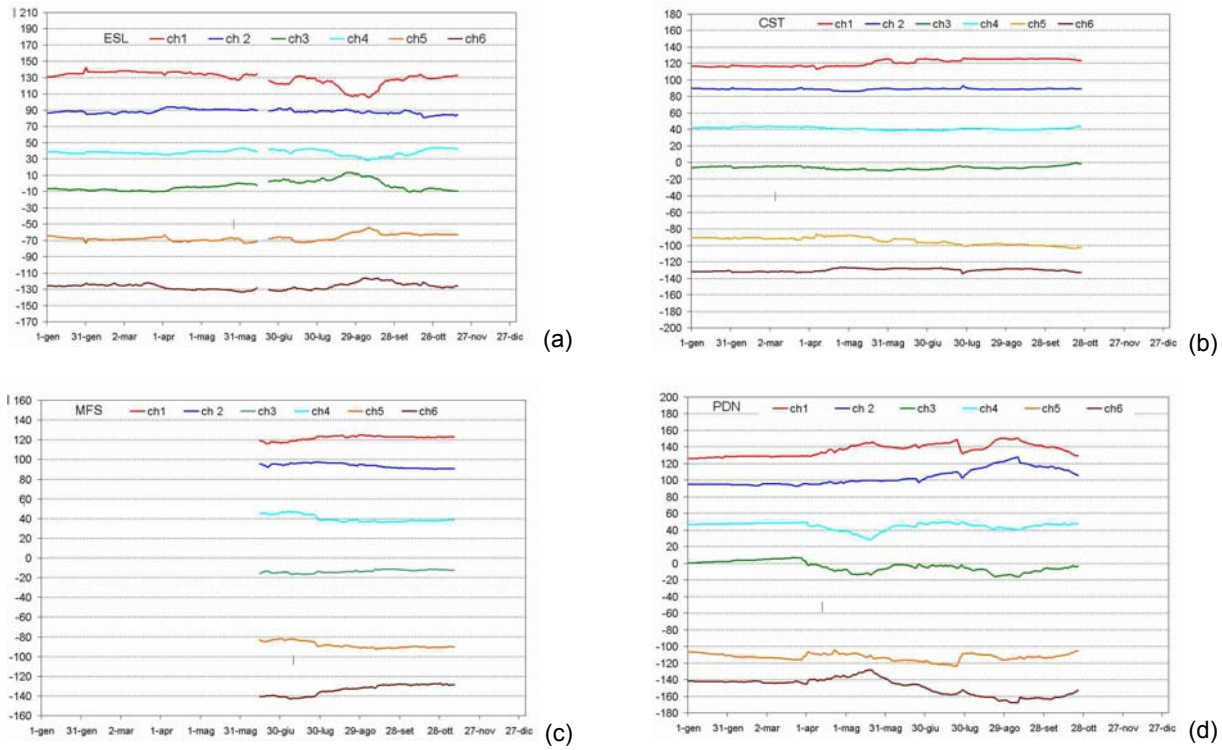

Fig. 4 – Daily means of SP signals recorded at ESL, CST, MFS and PDN stations along two orthogonal directions (ch1, ch2, ch3, ch4) and along diagonals (ch5, ch6).

Contacts:

Rosalba Napoli
Phone +39 095 716 58 24
Email: napoli@ct.ingv.it

Gilda Currenti
Phone +39 095 716 58 24
Email: currenti@ct.ingv.it

MONITORING OF STROMBOLI ISLAND

Multiparametric monitoring system

Between 2003 and 2005 a multiparametric system aimed at volcanic monitoring has been set in Stromboli island (Fig. 1). The system consists of 3 gradiometric stations measuring the total magnetic field, 1 station measuring self potential and a continuously recording gravimeter (ODF) settled near to Firenze University Observatory. During 2006 Stromboli data acquisition system worked regularly and signals recorded at various stations seem to be well-correlated. Only at SPL magnetic station frequent malfunctioning occurred, so that we had to disable the station in June.

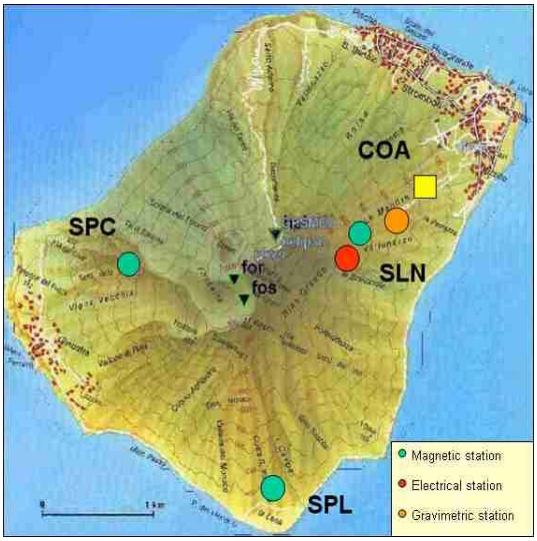

Fig. 1 - Sketch map of Stromboli island showing the sites of the continuously running stations.

Continuous gravity data

Gravimetric signal recorded at ODF (Osservatorio dei Fiorentini) station between May and December 2006, correct from earth tide effects and instrumental drift, is shown in Fig. 2. The lowest frequency component has been removed from the signal, too.

Gaps in the sequence are due to instrumental effects produced by teleseismic or anthropic source. A preliminary analysis of the acquired sequence has shown no gravity field variation with a period greater than one day which exceeding the relevance threshold that can be expected taking into account the conditions at the site are far from being ideal.

Fig. 2 - Gravity variations observed at ODF continuous gravity station between May and December 2006

The data sequence shows anomalies having features similar to variations already observed in the past at this station (Fig. 3). They are sharp variations (last few minutes) of the signal level and their amplitude is of a few μGal peak to peak. Even though hypothesis about the source of these variations have been done, and in particular a link with the ascent of big gas bubbles along the central main pipe has been assumed, an exhaustive study aimed at the validation of these hypothesis isn't finished yet.

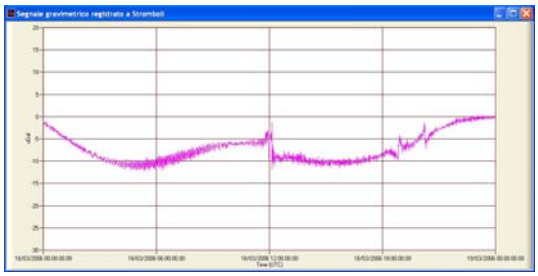

Fig. 3 – Gravity variations observed at ODF continuous gravity station during March 2006.

Magnetic observations

During 2006, magnetic stations of Stromboli worked regularly except SPL where the continuity of measurements was severely compromised by numerous failures of the gradiometer which was deactivated in June. The daily mean differences of the magnetic field gradients at SPL, SPC and SLN stations from January to December 2006 are shown in figure 4. The differences show at SPC station an annual periodic geomagnetic component whose amplitude is negligible, while a slow and continuous decrease of about 4 nT clearly appears at SLN up to the end of July. In Fig. 5 are shown the daily means of total intensity variations observed at SPL, SPC and SLN, relative to CSR. Intense transient magnetic variations are detected in correspondence of strong external activity.

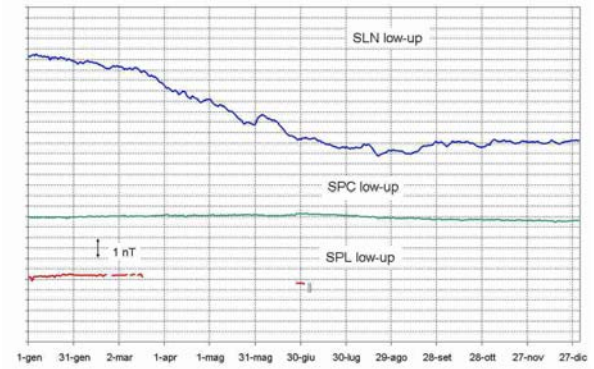

Fig. 4 – Daily means of the magnetic field gradient calculated from January to December 2006 at SPL, SPC and SLN stations.

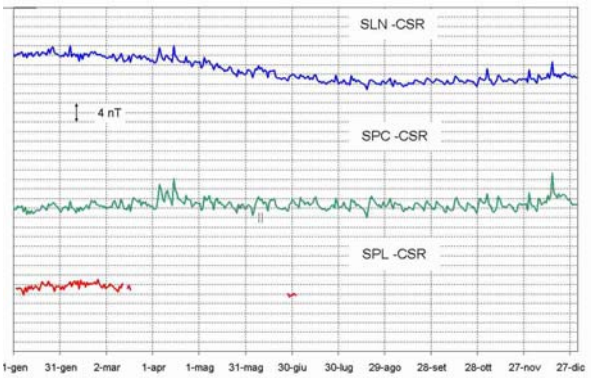

Fig. 5 – Daily mean differences of the total magnetic field recorded at SPL, SPC and SLN, with respect to CSR.

Measurements of Self Potential

The self potential (*SP*) signals represent the measure of the potential voltage difference between two points on earth surface due to the presence of an electric field produced by natural sources distributed in the subsoil. In near surface geophysics the most relevant phenomenon which could originate the self-potential anomalous field is known as electrofiltration or streaming potential. It refers to the electrical signals produced when a fluid flows in a porous rock as a consequence of a pore pressure gradient.

The phenomenon is generated by the formation in the porous ducts of a double electrical layer between the bounds of the solid, that absorb anions of the electrolyte, and cations distributed in one diffused layer, near the boards. When the fluid, subordinate to pressure gradient, flows, it transports a part of the cations, provoking on one side an excess of positive charges. Then, it develops an electric field induced along the length of the duct and the associated potential differences (streaming potential), that it is generated to the ends of the duct.

The streaming potential is expressed by the following formula:

$$\Delta V = C\,\Delta P = \frac{\zeta \rho \varepsilon}{4\pi\eta}\Delta P$$

where ζ is the zeta potential, that is the potential defined on the slipping plane between mobile and immobile charges, η is the dynamic viscosity of the electrolyte, ε is the dielectric constant of electrolyte, ρ is the resistivity of electrolyte, ΔP is the gradient of pressure and C is the coefficient of streaming potential.

On 1 June 2005 the first station for measuring self potential (SP) signals was installed at Stromboli Island in correspondence of the magnetic station of SLN (Fig. 1). The array is characterized by five Pb-PbCl2 electrodes put at 70 cm depth. The purpose of this SP station is to detect electrical anomalous patterns associated with local seismicity. This station was installed as part of a cooperative program with V. Lapenna of the CNR-IMAA in Potenza, Italy. During 2006 the station for measuring self potential (SP) signals worked regularly and continuously. The daily means of SP signals recorded from June 2005 to March 2006 are shown in Fig. 6. In this period no significant geophysical changes are recorded.

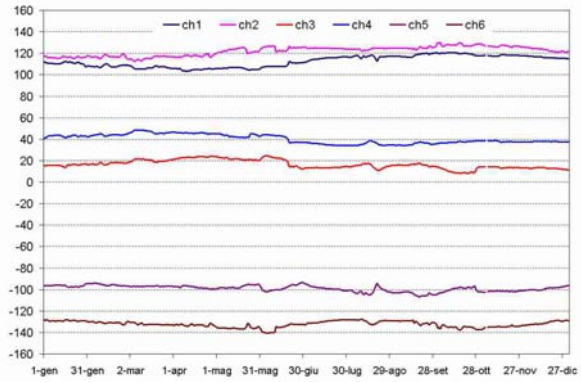

Fig. 6 – Daily means of SP signals recorded at SLN station along two orthogonal directions (ch1, ch2, ch3, ch4) and along diagonals (ch5, ch6).

Contacts:

Filippo Greco
Phone +39 095 716 58 25
Email: greco@ct.ingv.it

Rosalba Napoli
Phone +39 095 716 58 24
Email: napoli@ct.ingv.it

RESEARCH PAPERS

Over the last decade, the *volcanology* has become increasingly quantitative evolving from an empirical to a more quantitative approach in the study of volcanic processes. Within this framework, new modern techniques of volcano monitoring have been also implemented by *UFGM* in order to mitigate the volcanic hazard on *Mt Etna* and *Stromboli Island*. The amount of available data produced represents a huge database. However, a significant amount of work is still required to understand the volcano behavior and hazard issues. Furthermore, many studies so far conducted have been only scarcely finalized to a quantitative assessment of hazard despite the important implications they have.

Different kinds of hazard affect the two volcanoes and the surrounding areas: short-lived explosions, ash clouds, lapilli/ash fallout and lava flows, earthquakes triggered by magma intrusions, landslide and tsunami. Each of these scenarios should be preceded and accompanied by variations of geophysical parameters. Nevertheless, strong improvements are required for the evaluation of the statistical significance and the interpretation of geophysical variations. Therefore, during the 2006 the studies for identifying and characterizing *precursory signals* have represented a fundamental issue of *UFGM*. They would drastically improve our capability to forecast the volcanic phenomena, in terms of both time occurrence and magnitude. Moreover, as physical volcanology has better defined its methods and objectives, elaborated *mathematical models* have been devised to track the spatio-temporal evolution of eruptive processes based on geophysical observations.

However, despite the frequent occurrence of eruptive activity, significant steps forwards still need to be done in the quantification of its hazards. Even if, about *lava flows*, the production of accurate lava flow invasion maps at Etna have represented an important step for the assessment of the medium and long-term hazard associated to this phenomenon. Similarly, the development of reliable quasi real-time lava flow models allowed to forecast different scenarios of lava propagation and to plan the appropriate mitigation measures during the 2006 Etna eruption.

Short papers describing the researches conducted at *UFGM* during the 2006 are attached below.

MFS magnetic station on Mt Etna before being destroyed by the lava flow on 29 March 2007.

ADAPTIVE NEURO-FUZZY INFERENCE SYSTEM FOR DENOISING GRAVITY AND GEOMAGNETIC SIGNALS

Rosalba Napoli and Filippo Greco*

Isitituo Nazionale di Geofisica e Vulcanologia, Sezione di Catania
** Email: napoli@ct.ingv.it*

Abstract

One of the main problems of signal analysis is discriminating between the components of the signal related to the volcano activity from variations due to other sources. To date filtering noise is a very complex problem since the spectrum of each noise component has wide intervals of superposition and, some times, traditional filtering techniques provide unsatisfactory results. Here, the adaptive neuro-fuzzy inference system (ANFIS) was proposed to remove noise effects from gravity and geomagnetic signals continuously recorded by the permanent monitoring networks on the Etna volcano. Results suggest a good efficiency of the proposed approach which is able of finding and effectively representing the underlying factors or sources, and allow local features of the signal to be detected.

Key words: gravity data, geomagnetic data, ANFIS, Etna volcano.

Introduction

Gravity and geomagnetic signals recorded in volcanic areas are severely influenced by meteorological variables, i.e. pressure, temperature and humidity, whose disturbances can make the detection of volcanic source effects more difficult. For all practical purposes, volcano monitoring is concerned with detection of gravity and geomagnetic anomalies attributable to the dynamics of a volcano and removal of variations with no geophysical significance.

Temporal gravity changes in volcanic areas are related to sub-surface mass-redistributions and/or surface elevation changes in response to magmatic activity, and their amplitude, wavelength and duration depend on several parameters such as the size, depth and evolution rate of the sources. The expected gravity changes due to volcanic sources range in amplitude between 10 and 1000 μGal (1μGal = 10^{-8} ms^{-2}) with a spectrum varying from 1-10 s to more than 1 yr. To isolate gravity residuals, due to sub-surface mass-redistribution it is necessary to remove the effects of non volcanic sources (i.e. luni-solar gravitational effects, atmospheric contribution, instrumental drift, ground tilt etc). Unluckily, the behavior of spring gravity meters have proven to be severely influenced by meteorological variables (i.e. pressure, temperature and humidity; Andò and Carbone, 2001, 2004, 2006; Carbone et al., 2003; El Wahabi et al., 1997; Warburton and Goodking, 1977) especially when used in the adverse environmental conditions often encountered at active volcanic areas. The correction formulas are instrument-specific and often frequency-dependent. Obviously, frequency-domain filters cannot be applied to remove the effects of these perturbations since the spectrum of each noise component has wide intervals of superposition.

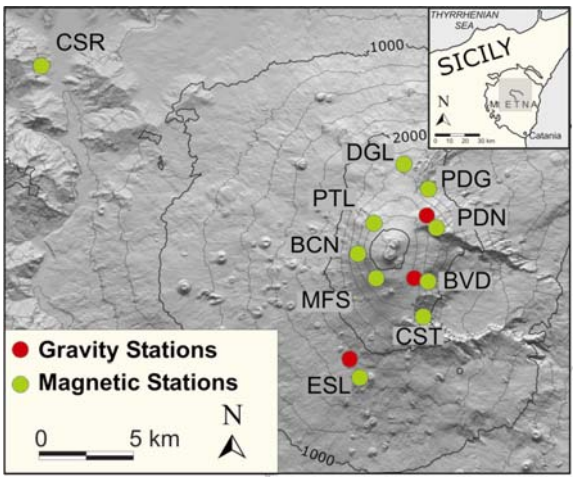

Fig. 1 - Schematic map showing the locations of the continuous gravity and magnetic stations operating on Mt Etna.

Geomagnetic changes attributable to the dynamics of a volcano are usually very small, within 1~10 nT, while changes up to a few hundreds nanoteslas are caused by natural geomagnetic fluctuations of external origin. The most frequently used and reliable method to remove them is the classical differential technique, based on simultaneous simple differences among the magnetic field amplitudes recorded at several points on a volcano. Unfortunately, this technique does not allow properly reducing the geomagnetic signal to the level of a few nanoteslas, which is the apparent

upper limit of detectability of magnetic anomalies associated with volcanic activity (Davis et al, 1981). To increase the detectability of volcano-related magnetic field changes, methods of predictive filtering (Davis et al., 1981) and adaptive type approach (Currenti et al., 2004) have been suggested to reduce transient fields, which could be of the same order as the volcanomagnetic signal to be detected. However, even if the effects of external and transitory fields are properly eliminated, periodic variations in the geomagnetic total intensity, probably caused by seasonal changes in the heterogeneous magnetization of near-surface rocks due to a diffusion of atmospheric temperature changes into the ground (Utada et al. 2000), have clearly been observed in the magnetic reduced signals (e.g., Johnston, 1989; Zlotnicki et al., 2000; Del Negro et al 2004).

In order to remove noise effects from gravity and geomagnetic time series recorded by the permanent monitoring networks of Etna volcano we propose the application of a nonlinear autoregressive model based on the application of an Adaptive Neuro-Fuzzy Inference System (ANFIS), whose intrinsic learning features seem to be particularly suitable for such a task.

Preliminary analysis

The continuously monitoring systems working at Etna (Fig.1) were set up in 1998 (Del Negro et al. 2002; Carbone et al., 2003). Simultaneously with gravity and magnetic signals, atmospheric and ground temperature, pressure and humidity are acquired at each station. The definition of a background level for each signal requires a long and continuous data series acquired in unperturbed (i.e. quiescent period) conditions, therefore we used data gathered on Etna when no significant volcanic activity was observed. As a first step, we reduced gravity data for the effect of Earth Tide and instrumental drift (Torge, 1989). The effect of Earth Tides is modeled through the Eterna 3.30 data processing package (Wenzel, 1996). To correct the data for the main effect of instrumental drift a best linear fit was removed from the sequences. For geomagnetic signals we have used the difference of the geomagnetic fields measured by magnetic stations located in the volcanic area with respect to the reference station (CSR).

Considering that effect of meteorological variables mainly affects the long period components (Carbone et al., 2003; Del Negro et al 2004), we computed hourly averages and used time series generally of about 6 months or more. In order to define the correlation between gravity, geomagnetic data, and meteorological variables (temperature, pressure and humidity), we performed analysis both in the frequency (Fig. 2) and in time domain for each time series investigated. Both gravity and geomagnetic signals show a strong correlation with temperature.

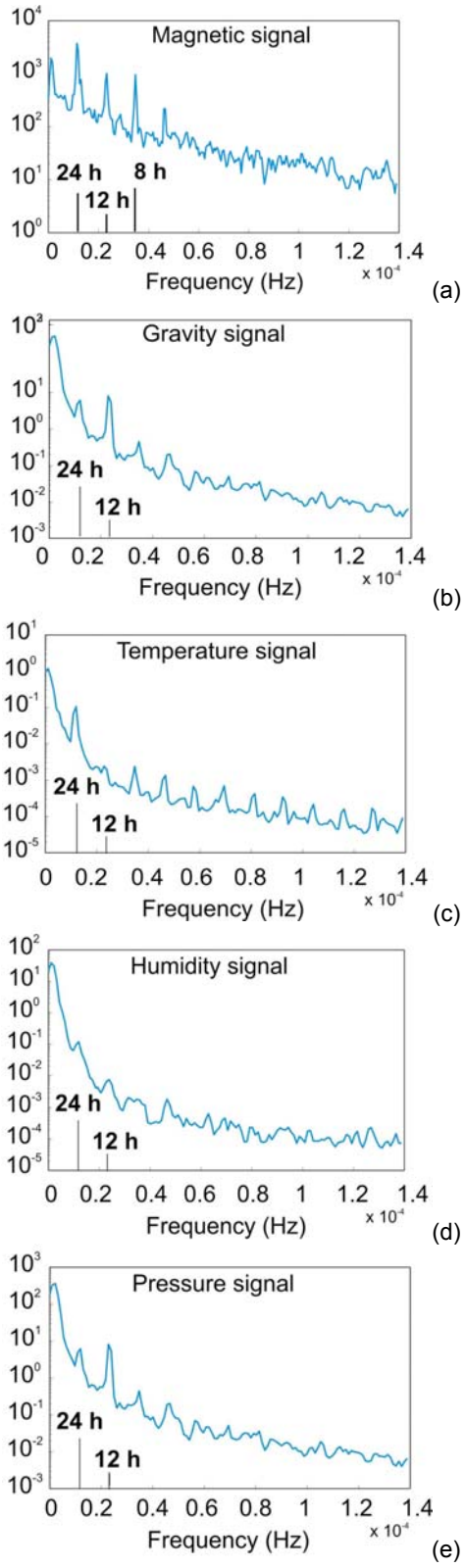

Fig. 2 – Power spectral densities of analyzed signals: (a) geomagnetic; (b) gravity; (c) temperature; (d) humidity; (e) pressure.

In particular, gravity data are anti-correlated and show a considerable time lag up of to 900 hours. As regards geomagnetic data, it is worth noting that the significant correlations found between differences of geomagnetic signals and temperature, over a time lag of about 10 hours, are not so marked when we considered the raw signals. Correlations were also observed between gravity signal and pressure with a time delay of about 200 hours, and between geomagnetic data and humidity. Conversely low correlation indexes were obtained between gravity sequences and humidity, and between geomagnetic data and pressure for all values of the time delay. These correlations were taken into consideration during the implementation of the model for reducing geophysical signals for the effect of meteorological variables.

The ANFIS non linear approach

In order to denoise gravity and geomagnetic signals from effects of temperature, pressure and humidity we implemented an adaptive network based on fuzzy inference system (ANFIS). The denoising scheme (Fig. 3) is based on the idea of existence of a time interval in which the signal y(t) is not affected by a volcanic source. Furthermore, we assume that this process is stationary. In this hypothesis, a residual signal r(t), can be computed as:

$$r(t) = y(t) - y'(t)$$

where y'(t) is the estimated value of y(t). This residual in absence of effects due to the volcanic sources, that might involve mass redistribution and/or variations of the local geomagnetic field, will be limited in amplitude to typical ranges depending on the considered signals. Knowledge of the magnitude of the residuals in "quiet periods" allows to recognizing and isolating the anomalies due to volcanic sources.

The development environment adopted was the Matlab Neuro-Fuzzy tool. The model uses three bell shaped membership functions and a Sugeno model structure of the rule base. Based on results of correlation analysis the most promising candidates as input variables were the temperature (*T*) and pressure (*P*) for the gravity signal and the temperature and humidity (*H*) for geomagnetic signals. Once the input variables have been chosen, it is necessary to define the structure of the autoregressive model. The structure for modeling the effects of temperature and pressure in the gravity signals is defined as follows:

$$y(t) = f(T(t), T(t-m), T_{mean}(t-m), P(t), P(t-n), P_{mean}(t-n))$$

where f is the non-linear model estimated by neuro-fuzzy algorithm; t is the present time index; T and P represent temperature and pressure, respectively; m and n represent appropriate time delays obtained by the cross-correlation analysis; $T_{mean}(t-m)$ and $P_{mean}(t-n)$ are the mean values of temperature and pressure within the intervals [t-m, t] and [t-n, t].

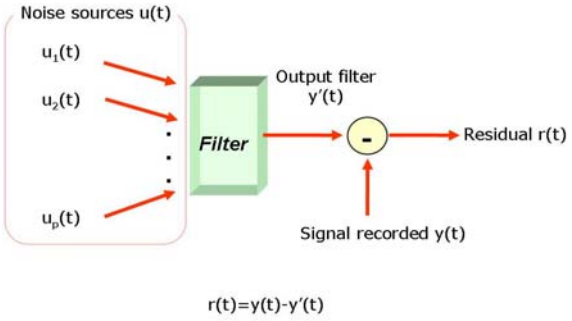

Fig. 3 – Filtering strategy used to remove the effects of meteorological variables u1(t), …u_p(t), from gravity and geomagnetic time series considered.

The model was practically applied to the gravity sequences recorded from January to December 2005 at BVD station and from June to December 2005 at PDN station. Large components with amplitude of about 600 (BVD) and about 500 µGal peak-to-peak (PDN) are strongly dominant in both gravity sequences (Fig. 4). The amplitude of the residual signals, calculated as the difference between the instrumental effect due to atmospheric temperature and pressure, estimated by the model and gravimeters output, is very low compared to the original signals. These results highlight that the instrumental effects of atmospheric temperature and pressure are the most significant components of all the original signals, and are strongly confirmed also through the low correlation factors between residual gravity sequences and temperature and pressure signals (Tab. 1).

	Temperature	***Pressure***
Gravity residual at BVD	-0.055	-0.043
Gravity residual at PDN	-0.029	-0.035

Tab. 1 - Correlation indexes between residual gravity signals and temperature and pressure after removing the corresponding model for temperature and pressure effects estimated by ANFIS from each gravity sequence.

(A)

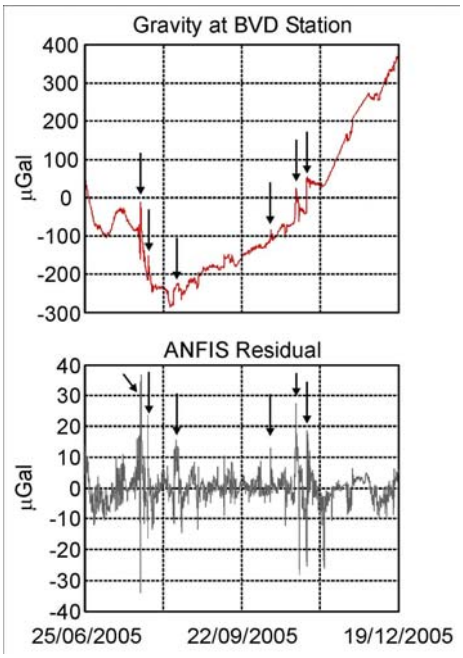

(B)

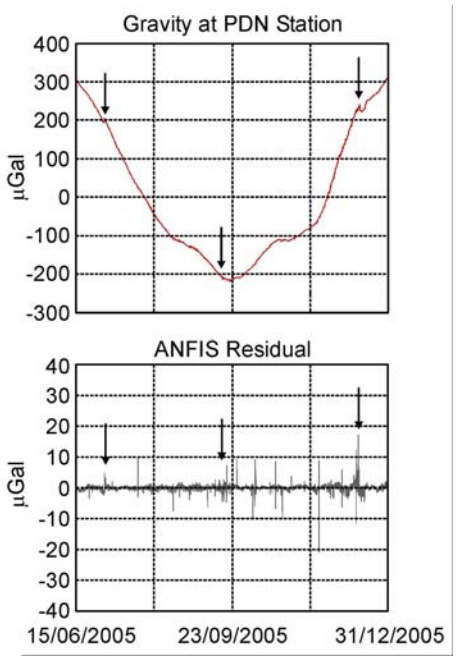

Fig. 4 – A panel: at the top, gravity signal after removal of the best linear fit and the theoretical Earth Tide observed at BVD station from June to December 2005. At the bottom, gravity residual after removing the meteorological effects estimated by ANFIS model.
B panel: at the top, gravity signal after removing the best linear fit and the theoretical Earth Tide observed at PDN station from June to December 2005. At the bottom, gravity residual after removing the meteorological effects estimated by ANFIS model.
Black arrows indicate anomalies which are not related to the meteorological variables.

We can see that the ANFIS method removes satisfactorily the long period components of the gravity sequences, considered harmonic of the annual oscillation due to the influence of the seasonal atmospheric variables changes.

The magnitude of the residuals as well as diurnal and semidiurnal components are highly comparable each other and are in the order of 2 ÷ 3 µGal. Instead, a significant component with amplitude of about ± 10 µGal peak-to-peak and a period of about 20 days strongly emerges in the residual of BVD (Fig. 4). This discrepancy is probably due to the position of the BVD station, located very close to the SE Crater (about 700 meters). The residual may reflect changes in the local gravity field due to the "normal" activity of the Crater.

For geomagnetic data, pressure was substituted by humidity (H) on the grounds of the cross correlation analysis and consequently the model is defined as follows:

$$y(t) = f(T(t), T(t-m), H(t), H(t-n))$$

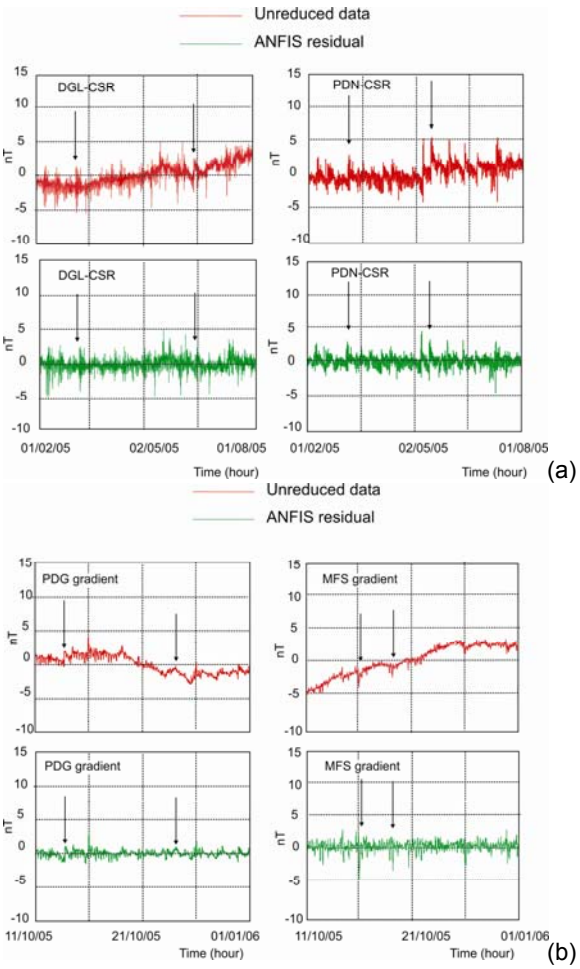

Fig. 5 – Comparison between the unreduced geomagnetic data (in red) and the residuals (in green) estimated by ANFIS model considering (a) the differences of the geomagnetic signals (DGL-CSR and PDN-CSR) and (b) raw signals recorded at the gradiometric stations of PDG and MFS. Black arrows indicate anomalies which are not related to the meteorological variables.

This model was applied to the hourly averages of total intensity variations from February to August 2005 observed at PDN and DGL stations, relative to the reference station (CSR). It is worth stressing that, though external magnetic fields were previously removed by differential technique, and at that time no significant volcanic activity occurred, a clear trend is still evident especially at DGL station (Fig. 5a). In order to evaluate the capability of the filtering process, we compared the estimated residuals with the differences of total magnetic intensity with respect to CSR station. The magnitude of the residuals is lower than the original ones and no evident trend appears (Fig. 5a).

Unreduced data	***Temperature***	***Humidity***
PDN-CSR	0.68	0.54
DGL-CSR	0.66	0.20
MFS gradient	0.87	0.42
PDG gradient	0.84	-0.18

Residuals	***Temperature***	***Humidity***
PDN-CSR	0.003	0.008
DGL-CSR	0.00001	0.002
MFS gradient	0.0016	-0.02
PDG gradient	0.021	-0.003

Tab. 2 - Correlation indexes between meteorological variables (temperature and humidity), recorded geomagnetic signals and residuals obtained by ANFIS filtering.

At the same time, we used hourly averages of total intensity variations recorded at the MFS and PDG gradiometric stations. Each station consists of two sensors, (namely MFSnorth, MFSsouth, PDGnorth and PDGsouth) spaced horizontally by about 50 m, which simultaneously sample the Earth's magnetic field. In this case, we initially applied the model to the raw signals recorded by each sensor and then the residual signals were differentiated to obtain the gradient (MFSnorth-MFSsouth and PDGnorth - PDGsouth). Figure 5b shows the comparison between the hourly averages of the unreduced magnetic gradients recorded from October 2005 to January 2006 at MFS and PDG and the difference of residuals estimated by ANFIS model. It is evident that the long period fluctuations affecting original signals, probably due to the joint effects of temperature and humidity, are successfully removed. To better estimate the validity of the model, as well as for the gravity case, a correlation analysis between each residual and temperature and humidity was calculated. Also in this case, the correlation indexes significantly decreased, ranging between 0.02 and 0.00001 for temperature and between 0.02 and -0.003 for humidity (Table 2)**.** These results confirm that the applied model removes both the effect of temperature and the humidity from magnetic data.

Discussion and conclusion

With the aim of developing a novel approach to analyze gravity and geomagnetic time series recorded in volcanic areas, we proposed the ANFIS method. Results presented throughout this paper show the denoising capability of this technique for removing noise from both gravity and geomagnetic signals. In particular, the very low correlation indexes between residuals and the set of explaining variables confirm that both approaches are able to efficiently remove the effects of meteorological variables from considered geophysical data. It is important to stress the presence of small anomalies (such as amplitude) in the gravity and magnetic time series both in the unreduced and reduced signals, which are not due to changes in the meteorological variables (Figs. 4 and 5).

Gravity data	***Unreduced signal***	***ANFIS residual***
PDN	165.36 μGal	1.01 μGal
BVD	155.98 μGal	4.86 μGal

Geomagnetic data	***Unreduced signal***	***ANFIS residual***
PDN-CSR	1.25 nT	0.66 nT
DGL-CSR	1.56 nT	0.84 nT
MFS gradient	2.25 nT	1.25 nT
PDG gradient	1.34 nT	0.47 nT

Tab. 3 - Standard deviations of recorded gravity, geomagnetic signals and residuals obtained by the ANFIS and the ICA approaches.

The standard deviations of residuals were also assessed to verify the obtained results (Table 3). It should be noted, that the standard deviation of residuals is much decreased both for gravity and geomagnetic data when compared to that of the unreduced—signals. In particular, gravity residuals show standard deviations lower than 98 ÷ 99% in comparison with original data, while the standard deviation of geomagnetic residuals decreased by about 40 % (for PDN, DGL and MFS stations) and more than 60% for the PDG station. The ANFIS technique removes efficiently noise components showing itself a valid approach to the general problem of denoising geophysical data. The results are highly promising, and in our view the proposed technique outperform traditional time series filtering in terms of efficiency. This is an important

chance since the gravity and magnetic signals could include volcanic effects with a wide range of evolution rates.

References

Andò, B.and Carbone, D., (2001). A methodology for reducing a continuously recording gravity meter for the effect of meteorological parameters. IEEE Trans. Instrum. Meas. 50 (5), 1248–1254.

Andò, B. and Carbone, D., (2004). A test on a Neuro-Fuzzy algorithm used to reduce continuous gravity records for the effect of meteorological parameters. Phys. Earth Planet. Int. 142, 37–47.

Andò, B. and Carbone, D., (2006). A new computational approach to reduce the signal from continuously recording gravimeters for the effect of atmospheric temperature. Phys. Earth Planet. Int. 159, 247–256

Carbone, D., Budetta, G., Greco, F. and Rymer, H., (2003). Combined discrete and continuous gravity observations at Mt. Etna. J. Volcanol. Geotherm. Res. 123, 123–135.

Currenti, G., Del Negro, C., Fortuna, L., Napoli, R. and Vicari, A., (2004). Non-linear analysis of geomagnetic time series from Etna volcano, Nonlin. Proc. Geophys., 11, 119-125, Sref-ID: 1607-7946/npg/2004-11-119.

Davis, P.M., Jackson, D.D., Searls, C.A. and McPhernon, R.L., (1981). Detection of tectonomagnetic events using multichannel predictive filtering. J. Geophys. Res., 86, 1731-1737.

Del Negro, C., Napoli, R. and Sicali, A., (2002). Automated system for magnetic monitoring of active volcanoes, Bull. Volcanol., 64, 94-99.

Del Negro, C., Currenti, G., Napoli, R. and Vicari, A., (2004). Volcanomagnetic changes accompanying the onset of the 2002-2003 eruption of Mt. Etna (Italy). Earth and Planetary Science Letter 229, 1-14.

El Wahabi, A., Ducarme, B., Van Ruymbeke, M., d'Orey`e, N. and Somerhausen, A., (1997). Continuous gravity observations at Mount Etna (Sicily) and correlations between temperature and gravimetric records. Cah. Centre Eur. G´eodyn. S´eismol. 14, 105–119.

Johnston, M.J.S., (1989). Review of magnetic and electric field effects near active faults and volcanoes in the U.S.A. Earth Planet. Sci. Lett., 57, 47-63,

Torge, W., (1989). Gravimetry. Walter de Gruyter., Berlin-New York.

Utada, H., Neki, M. and Kagiyama, T., (2000). A study of annual variations in geomagnetic total intensity with special attention to detecting volcanomagnetic signals, Earth Planets Space, 52, 91-103.

Warburton, R. J. and Goodkind, J.M., (1997). The influence of barometric-pressure variations on gravity. Geophys. J. R. Astron. Soc., 48: 281-292.

Wenzel, H.G., (1996). The nanogal software: Earth tide data processing package ETERNA 3.30. Bull. Inf. Marees Terrestres, 124, 9425-9439.

Zlotnicki, J., Bof M., Perdereau L., Yvetot P., Tjetjep W., Sukhyar R., Purbawinata M.A and Suharno, (2000). Magnetic monitoring at Merapi volcano, Indonesia, J. Volcanol. Geotherm. Res., 100, 321-336.

DENOISING CONTINUOUS GRAVITY DATA USING WAVELET MULTI-CHANNEL FILTER ANALYSIS

Filippo Greco

Isitituo Nazionale di Geofisica e Vulcanologia, Sezione di Catania
Email: greco@ct.ingv.it

Abstract

Continuous gravity recordings in volcanic area could play a fundamental role in the monitoring of active volcanoes and in the prediction of eruptive events too. This geophysical methodology is used, on active volcanoes, in order to detect mass changes linked to magma transfer processes and, thus, to recognize forerunners to paroxysmal volcanic events. Spring gravimeters are still the most utilized instruments for this type of microgravity studies. Unfortunately, spring gravity meters show a strong influence of meteorological variables (i.e. pressure, temperature and humidity), especially in the adverse environmental conditions usually encountered at such places. As the gravity changes due to the volcanic activity are very small compared to other geophysical or instrumental effects we need a new mathematical tool to get reliable gravity residuals susceptible to reflect the volcanic effect. This study summarizes the results obtained by using a processing method based on wavelet transform for noise-filtering of continuous gravity data. To check the goodness of the method proposed we compared the residual of continuous sequence with data collected through discrete campaigns carried out in the same period at two sites very close to the continuous station.

Keywords: Gravimeter, wavelet transform, filtering, volcanic monitoring

Introduction

The perturbations of the local gravity field in volcanic areas are often related to sub-surface mass/volume/density redistributions or to elevation changes in response to magmatic processes and vary significantly in both space (wavelengths ranging from hundreds of meters to tens of kilometers) and time (periods ranging from minutes to years) according to the size, depth and rate of evolution of the perturbing source. Continuous gravity recordings in volcanic areas, acquired at 1datum/min sample rate (each datum is the average calculated over 60 measurements), are prized for the high frequency information they provide in order to recognize forerunners to paroxysmal volcanic events. This kind of measurements are now increasingly performed at sites very close to active craters, where there is the greatest opportunity to detect significant gravity changes due to the volcanic activity. Spring gravity meters are still the most utilized instruments for volcano monitoring, because of their relatively low cost and small size which make them easy to transport and install. Unfortunately, this type of instruments have been shown to be severely influenced by meteorological variables (i.e. pressure, temperature and humidity), especially when used against the adverse environmental conditions usually encountered at areas so close to the active craters. The effect due to these perturbations can have an amplitude higher by one order of magnitude than the volcanic related one. This can seriously hinder the accurate detection of geophysical signals.
Several authors have demonstrated that meteorological variables, especially atmospheric temperature, affect continuously running spring gravimeters. In particular, El Wahabi et al (1997) proved that, over a yearly period, temperature changes can cause an instrumental effect up to 1 mGal (1 mGal = 10^{-5} ms^{-2}). Furthermore, an admittance up to 0.2 mGal/°C, over changes with period longer than 1 month, has been evidenced in Carbone et al (2003).

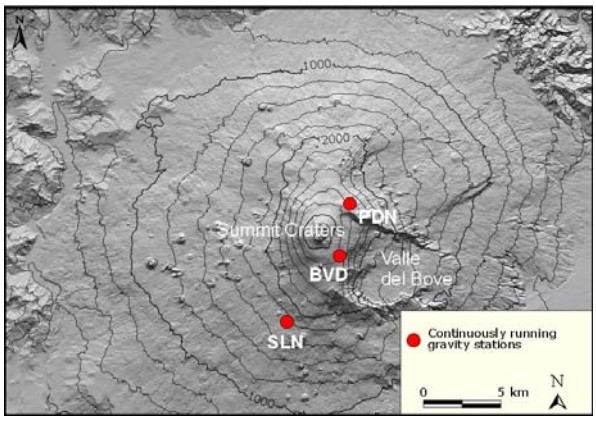

Fig. 1 - Sketch map of Mt Etna showing the continuously running gravity stations.

Thus, in order to obtain the volcano-related gravity signal, it is crucial to evaluate effectively the meteorological variables which can affect the gravity measurements at each station and to suitably remove their effect from the gravity signal. Since the transfer functions of these influences are frequency and instrument dependent is not easy to remove their effects. Moreover, frequency-domain filters cannot be efficiently applied to remove the effect of these perturbations since the spectrum of each component of various origins has wide intervals of superposition. Furthermore, frequency domain filtering does not always work well because: (i) it globally removes frequencies causing a generalized smoothing effect that substantially broadens features of interest; (ii) depending on both cut off frequency and filter order it also could introduce edge effects and distortions of the original signal; (iii) it does not allow to study local features of the signal in the time domain. A comparison between the traditional filtering methodology and the wavelet transform for continuous gravity data noise-filtering was proposed in Panepinto et al (2006).
In this paper we propose a data pre-processing method for noise-filtering based on wavelet transform. This technique allows to filter out unwanted-frequency-noise while preserving localized sharp signal features. The advantage of analysing a signal with wavelets is that it enables local features of the signal to be studied with a detail matching their characteristic scale. In the temporal domain, such a property allows transient signals to be represented effectively.

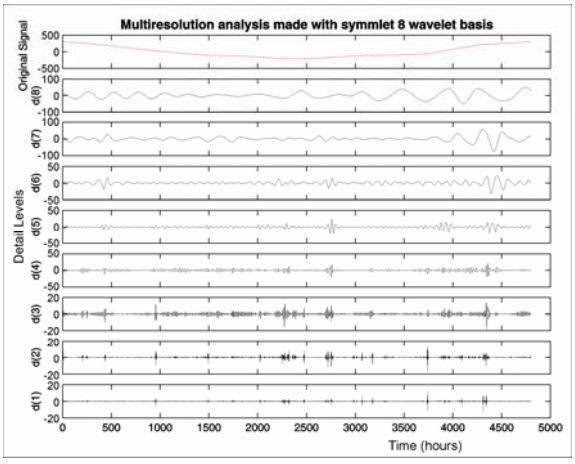

Fig. 2 - Multi-resolution analysis of the gravity signal made with Sym8 wavelet basis. The input signal is displayed in red at the top.

Data presentation and analysis

The continuously gravity stations working at Etna were set up during 1998 (Carbone et al., 2003) and at present, consist of 3 gravity remote stations (SLN 1710 m a.s.l.; PDN 2820 m a.s.l.; BVD 2910 m a.s.l.) at distances from Etna's summit craters ranging between 1 and 10 Km (Fig. 1). The gravity stations are equipped with LaCoste and Romberg (L&R) spring gravimeters, featuring analog feedback systems. The continuously recording stations were devised using innovative technologies which guarantee uninterrupted working under harsh environmental conditions.
In the present study, the denoising technique is applied to a short sequence (about 7 months registration) acquired at PDN gravity station (Fig. 1). The continuously running station is located about 2 km NE of the summit NE crater, inside the Volcanological Observatory. Data presented and analyzed in the following were acquired through L&R PET 1081 gravimeter with a measurement range of about 5 mGal. Besides gravity, other parameters were acquired: ground tilt in two perpendicular directions, atmospheric temperature, pressure, humidity and tension from the power system feeding the station. Data were recorded at 1datum/min sample rate (each datum is the average calculated over 60 measurements) through a CR10X Campbell Scientific data-logger and transmitted through a wireless connection to Catania.

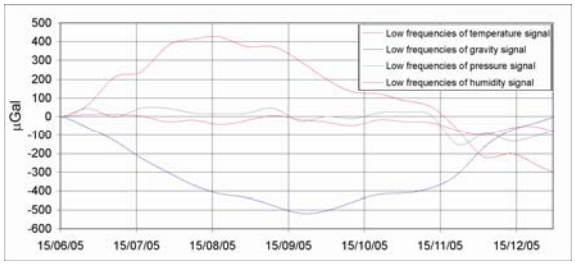

Fig. 3 - Over plot between low frequency components of gravity, temperature, pressure and humidity signals. In order to get the same scale, the temperature and pressure signals are multiplied by an amplification factor.

After removing the instrumental drift (modeled as a best linear fit) and the Earth Tide effect (modeled through the Eterna 3.30 data processing package; Wenzel, 1996), through the optimization of an automatic one-dimensional algorithm, that enables the wavelet decomposition to be made, a multi-resolution analysis of the signal was performed.
The advantage of analysing a signal with the wavelet multiresolution decomposition, considered as a band pass filter, is that it allows to filter signal into very narrow band with good frequencies response and without introduce phase lag. What's more, the wavelet based filter

furnished a good separation of the long period component from the short period one.
The “maximum compactness” or “minimum entropy” criterion, which Coifman and Wickerhauser (1993) and Fedi and Quarta (1998) applied for data compression and data analysis, respectively, was used here in an attempt to optimize the choice of the wavelet basis.
The gravity sequence was decomposed into eight detail and approximation levels (corresponding to different frequency bands; Fig. 2), on the grounds of the length of the considered time window using the wavelet basis Symmlet 8 (Daubechies, 1992).

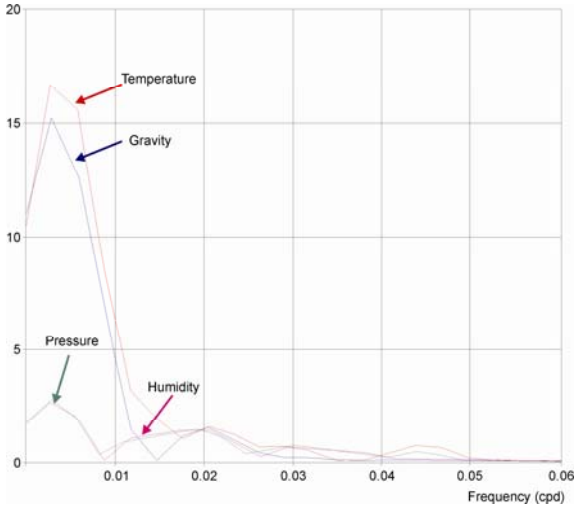

Fig. 4 - Spectra of the long period components of gravity and meteorological variables, obtained with the wavelet low pass filter.

The multi-resolution analysis allows local features of the signal to be studied in time domain and transient signals to be represented effectively. This is an important issue to point out, since the continuous gravity signal could include some volcanic effects, which in time span from minute to years. The only way to check them is the correlation, in the time domain, with other geophysical or geochemical signals.
Fig. 3 shows the long period components of the gravity, pressure, temperature and humidity signals acquired at the same station obtained with a low pass filter performed by wavelet transform. Instantaneous cross-correlation analysis in the time domain between the corresponding low frequencies component shows a strong anti-correlation between gravity and temperature (factor up to -0.77). Additionally, time cross-correlation analysis shows a time lag of about 900 hours of the gravity signal with respect to the temperature changes.
The Figure 4 shows the spectra of the long period components of all signals obtained with the wavelet low pass filter. This kind of analysis clearly shows that the spectrum of each signal contain the same main components. The main peak around 190 days is the harmonic of annual period which is not resolved properly due to the insufficient time span. Thus, it is more difficult to detect changes due to volcanic processes in the long period component of the signal, as this one is largely affected by the annual oscillations due to the meteorological variables.
Once the meteorological effects have been removed as a difference between the level obtained with the wavelet low pass filter, highly correlated with temperature (Fig. 5b) and gravity signal recorded (Fig. 5a), continuous gravity changes are within 20 μGal peak-to-peak (a reduction of about 95% respect to original signal). These result highlight that the instrumental effects of meteorological variables are the most significant components of the gravity original signal, and is strongly confirmed also through the poor correlation factors between residual gravity sequence and meteorological variables.

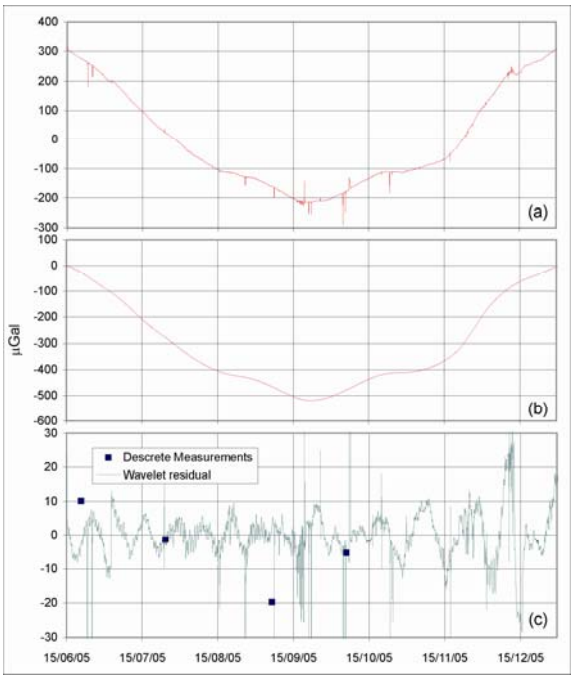

Fig. 5 - Reduced gravity sequence recorded at PDN by LCR PET-1081 gravity meter during 15 June – 31 December 2005 period. Comparison between: (a) the original signal after removal the theoretical Earth Tide and the best linear fit; (b) low frequency components of the gravity signal obtained with the wavelet low pass filter; (c) reduced gravity sequence, after removal of the best linear fit, the theoretical Earth Tide and the effect of meteorological variables modelled through a wavelet decomposition. Blue squares in figure c are gravity changes assessed by discrete relative observations at two sites very close to the continuous station.

Since we don’t have the real gravity at a given place, so we cannot be sure about the

effectiveness of the correction we have done, a good practice consists in comparing the residual of continuous sequences with data collected through discrete campaigns of measurements (Carbone et al., 2003). Here is reported an example of this kind of joint analysis (Fig. 5c). The residual gravity signal comes from PDN station was compared with discrete relative observations carried out in the same period at two sites very close to the continuous station. During the summer time, 4 campaigns of discrete measurements were made along a profile of 30 stations crossing the summit zone of the volcano (which is only reachable during the summer time because of the snow cover). Reduced continuous gravity changes from PDN station differ from gravity time changes at the benchmarks closer to the continuous station, by no more than 10 μGal (Fig. 5c). This result allows to validate the correction process we made on the continuous sequence.

Conclusions

A new promising technique, for continuous gravity data noise-filtering based on wavelet transform, was proposed. The aim of this preliminary work is only an overview about wavelet transform with an application on the continuous gravity data. Results presented throughout this paper, also by comparing wavelet residual with gravity changes assessed by discrete relative observations, show the denoising capability of the considered method for removing the effects of meteorological variables from continuous gravity signal.

Furthermore, the wavelet based filter does not require any tuning of parameters to produce results as good as the best achieved with frequency domain filters. This makes the process faster and more convenient. This paper stresses that the wavelet transform has others advantages: multi-resolution decomposition and time-space localization, two important characteristics for denoising problems.
Finally, the wavelet decomposition could be suitable for the construction of a non-linear multi-regression model that could enable a simultaneous correction of the main perturbing processes.

References

Carbone, D., Budetta, G.., Greco, F. and Rymer, H., 2003. Combined discrete and continuous gravity observations at Mount Etna. J. Volcanol. Geotherm. Res., 123, 123-135.

Coifman, R.R. and Wickerhauser, M.V., 1993. Wavelets and adapted waveform analysis. A toolkit for signal processing and numerical analysis. Proceeding of Symposia in Applied Mathematics, 47, 119-145.

Daubechiens, I., 1992. Ten lectures on Wavelets. Society for Industrial and Applied Mathematics.

El Wahabi, A., Ducarme, B., Van Ruymbeke, M., d'Oreyè, N. and Somerhausen, A., 1997. Continuous gravity observations at Mount Etna (Sicily) and correlations between temperature and gravimetric records. Cahiers du Centre Européen de Géodynamique et de Séismologie, 14, 105-119.

Fedi, M. and Quarta, T., 1998. Wavelet analysis for the regional residual and local separation of the potential fields anomalies. Geoph. Prospecting, 46, 507-525.

Panepinto, S., Greco, F., Luzio, D., Ducarme, B., 2006. An overview on wavelet multi-resolution decomposition compared with traditional frequency domain filtering for continuous gravity data denoising. Bull. Inform. Marèes Terrestres 141, 11213-11224.

Wenzel, H. G.., 1996. The nanogal software: Earth tide data processing package ETERNA 3.30, Bull. Inf. Marees Terrestres, 124, 9425-9439.

JOINT MODELING OF GROUND DEFORMATION AND GRAVITY CHANGES

Daniele Carbone and Gilda Currenti*

Isitituo Nazionale di Geofisica e Vulcanologia, Sezione di Catania
**Email: carbone@ct.ingv.it*

Abstract

The results of this study highlight the advantages of multi-objective evolutionary algorithms, as a powerful tool to jointly invert multi-method geophysical data, and pose important issues on the subject of volcano-monitoring.

Keywords: gravity changes, ground deformation, Pareto front, Etna volcano.

Introduction

Our main objective is the joint modeling of volcano-related gravity, ground deformation and magnetic data. We focused our activity on the development and optimization of the tools needed to meet the objectives of the project. In particular, this activity was split into two main phases: on one hand, a library of the most relevant forward models reported in the literature for the three above geophysical parameters was implemented; on the other, the inversion scheme, based on the identification of a Pareto optimal solution in the framework of a multi-objective Genetic Algorithm, was developed with the aim of more effectively converging towards the best source parameters of the model.

As for the first issue, the analytical formulations which were implemented are:

- *Gravity*

Tensile-crack	Sasai (1986)
Fracture zone	Okubo et al. (1989)
Fault model	Okubo (1992)

- *Magnetic*

Electrokinetic Fault model	Murakami (1989)
Piezomagnetic Mogi model	Sasai (1991)
Piezomagnetic Fault model	Utsugi et al. (2000)

- *Ground deformation*

Tensile-crack model	Sasai (1986)
Ellipsoidal source	Yang et al. (1988)
Fracture zone	Okubo et al. (1989)
Fault source	Okada (1992)

Through the above analytical formulations a wide range of processes occurring at volcanic areas, and often associated to the occurrence of paroxysmal events, can be modeled, i.e.: magma intrusion along sheet-like structures (faults, dykes), filling/withdrawal of elongated zones with uniformly distributed cracks, pressurization/de-pressurization of point sources by magma and/or gas intrusion/withdrawal, etc.

As for the second issue, the Genetic Algorithm was optimized to effectively solve multi-objective optimization tasks. To solve this kind of problems means to find the set of model parameters which satisfies some constraints and optimizes the objective function vector, whose components are the objective functions for each geophysical dataset. Usually, the contribution to the final solution of each dataset is obtained by constructing a weighted sum of all the objectives. However, the non-commensurability of the different objective functions means that the contribution of each dataset needs to be normalized and, if the weight coefficients are not properly chosen, the minimization of the functional may yield solutions that are dominated by one data set. To avoid this drawback, the NSGA-II algorithm (Non-dominated Sorting Genetic Algorithm) was utilized. It has two main advantages. Firstly, no weights need to be defined a priori since the scalarization of the objective function is avoided. Secondly, in a single run of inversion, a set of solutions is achieved (instead of a single one) representing the Pareto front. The size and shape of the Pareto front provides insights into the interactions among the objective functions: conflicting objectives (i.e. with different optimal solutions) imply a Pareto front spread over a large region of the vector space. Conversely, if all the objectives tend to converge towards similar solutions, the Pareto front is well confined in the vector space of the objectives.

Once developed, the above described tools (library of analytical models and inversion scheme for multi-objective optimization tasks) were tested within the framework of two case-studies from Etna volcano.

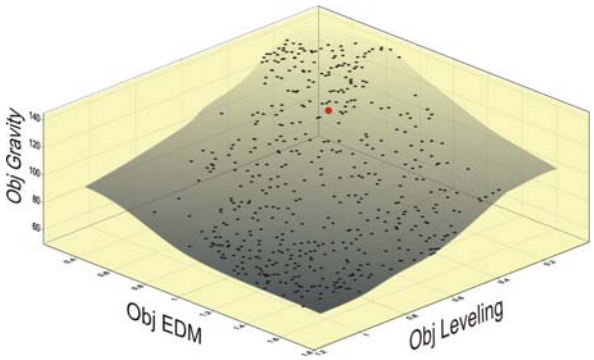

Fig. 1 - Objective function values of the Pareto front obtained after the first inversion cycle. The red circle indicates the selected vector of model parameters.

1981 Etna eruption

The first case-study refers to the March 1981 eruption which occurred on the North flank of the volcano. Gravity, leveling and EDM data encompassing the eruption are available. We inverted them jointly, using the formulations by Okada (1992) and Okubo (1992), as forward models, and an inversion scheme based on the NSGA-II algorithm. Both analytical formulations account for the effects arising from tensile faults buried in a homogeneous half-space and, while the former allows to calculate the displacement, shear and tilt due to the faulting processes, through the latter the corresponding gravity changes can be assessed. Thus, by coupling these two sets of analytical expressions we are able to forward model the ground-deformation and gravity effects of a given tensile source simultaneously and with the same set of model parameters.

Through the NSGA-II strategy, we obtained a family of about 500 solutions which form a Pareto front spread over a wide region (Fig. 1). The objectives relative to both horizontal and vertical deformation are minimized within a region of the Pareto front where the values of the objectives relative to gravity are unsuitably high. Conversely, to move along the Pareto front towards the region where the gravity objective is minimized, means to increase the value of the objective of both horizontal and vertical deformation beyond an acceptable limit (Fig. 1). This is an evidence of the conflicting behavior of the objective functions.

This discrepancy is likely to be due to the occurrence of mass changes without deformation accompanying the main intrusive process. We took into account this effect by assuming the presence of an infiltration zone surrounding each tensile fault (Fig. 2). All the geometrical parameters of the infiltration zone are in common with the corresponding tensile fault, but: (i) depth, (ii) opening, (iii) vertical extent (Fig. 2).

The new inversion cycle, which takes into account the additional mass, is also accomplished through the NSGA-II algorithm. It returns a Pareto front which is restricted within a smaller region with respect to the previous inversion step (compare Figures 1 and 3a), indicating that the objective functions interact cooperatively with each-other. The “best” model (red circle in Fig. 3a) provides a satisfactory fit to both ground deformation (Fig. 3b and 3c) and gravity data (Fig. 3d).

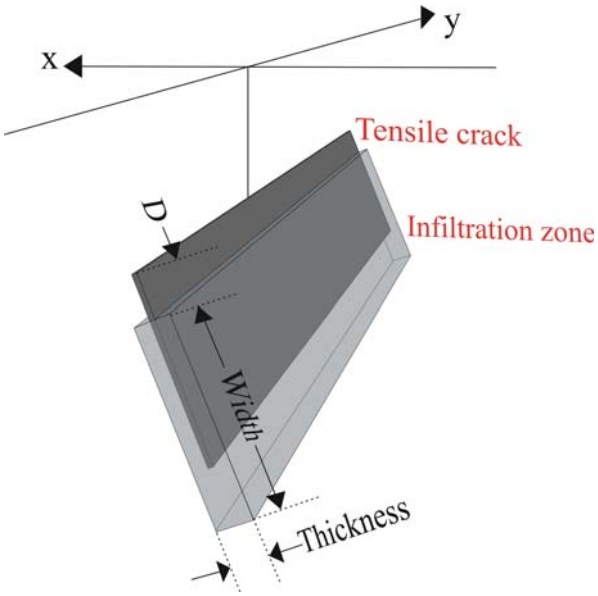

Fig. 2 - Geometrical relationship between the tensile crack and the corresponding infiltration zone.

The second case study refers to the July-August 2001 eruption which occurred on the southern flank of Etna. We tested the hypothesis that the marked gravity decrease before the eruption (80 microGal in 5 months) was due to the opening of a buried fracture zone on the southern flank of the volcano (subsequently used by the magma as a path to reach the surface). In this case, we utilized the formulation proposed by Okubo and Watanabe (1989), which assumes the opening of tensile microfractures within a rectangular parallelepiped-shaped volume. This model allows gravity and elevation changes to be calculated. Also in this case the inversion problem was formulated following a global optimization approach based on the use of Genetic Algorithms. Results showed that it is possible to explain the observed gravity changes by means of the proposed analytical formulation.

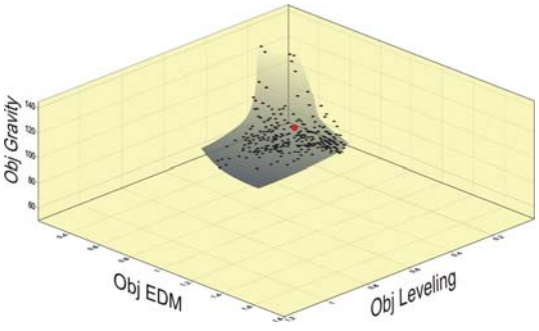

(a)

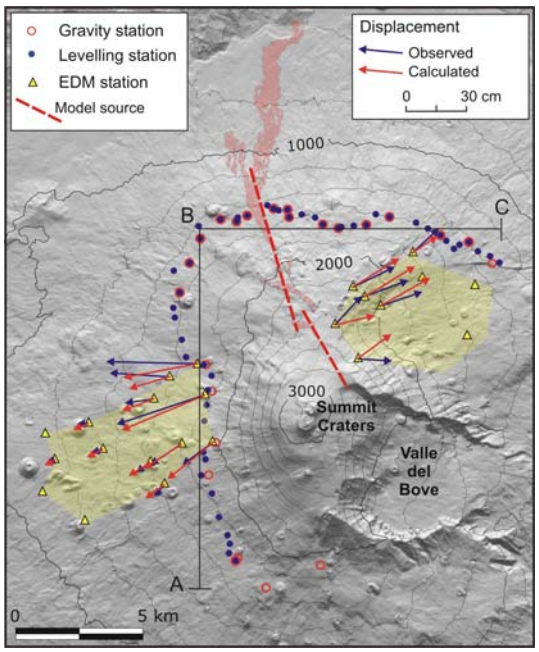

(b)

(c)

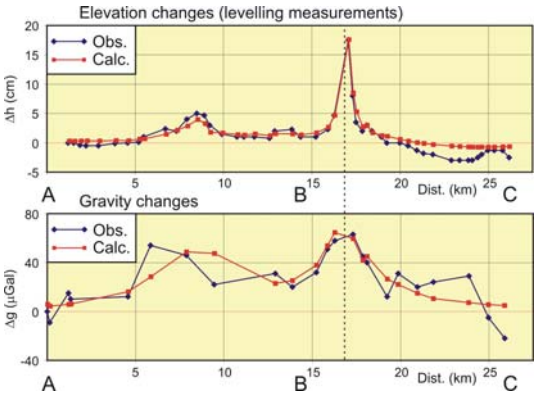

(d)

Fig. 3 - Objective function values of the Pareto front obtained from the second inversion cycle (see text for details). The red circle indicates the selected vector of model parameters (a). Observed (red) and modelled (blue) EDM (b), levelling (c) and gravity data (d).

Conclusive remarks

The above presented case studies proved the strong potential of the tools we have developed in the framework of the project to effectively perform joint inversions of multiparametric geophysical datasets. We show that the use of multi-objective evolutionary algorithms, and in particular the use of the NSGA-II, is especially suitable for the joint inversion of multi-method geophysical datasets. Besides offering the common advantages of GAs, such as their ability to globally optimize highly non-linear problems with limited amount of a priori information, the NSGA-II finds multiple Pareto optimal solutions in one single run (instead of converting the multi-objective into a single-objective optimization problem), a feature which is especially suitable when dealing with geophysical inverse problems, often characterized by ambiguous solutions. We thus encourage the development of a near-real-time system based on this algorithm to be used at volcanic areas where different geophysical parameters are routinely monitored.

References

Carbone, D., Currenti, G., Del Negro, C., 2007. Elastic model for the gravity and elevation changes prior to the 2001 eruption of Etna volcano. Bull. Volcanol., 69: 553–562.

Bonforte, A., Carbone, D., Greco, F., Palano, M., 2007. Intrusive mechanism of the 2002 NE-rift eruption at Mt Etna (Italy) modelled using GPS and gravity data. Geophys. J. Int., 169: 339–347.

Currenti, G., Del Negro, C., Ganci, G., 2007. Modelling of ground deformation and gravity fields using finite element method: an application to Etna volcano. Geophys. J. Int., 169 (2): 775-786.

Carbone, D., Currenti, G., Del Negro, C., Multi-objective Genetic algorithm inversion of ground deformation and gravity changes spanning the 1981 eruption of Etna volcano. J. Geoph. Res. (Submitted 2006).

Abstracts/conference presentations

Carbone, D., Currenti, G., Del Negro, C., Ganci, G., Giudice, S., 2006. Insights into the internal dynamics of active volcanoes through joint inversion of deformation and gravity data. EGU General Assembly 2006 - Vienna, Austria, 02-07 Aprile 2006 (oral session).

Currenti, G., Del Negro, C., Ganci, G., 2006. Finite Element Modeling of Ground Deformation and Gravity Data Observed at Mt Etna During the 1993-1997 Inflation Phase. American Geosciences Union - Fall Meeting 2006, San Francisco, CA, USA, 11–15 Dicembre 2006 (oral session).

Carbone D., Greco F., Budetta G., Andò, B., Del Negro, C., 2006. Continuous gravity measurements at Mt. Etna. American Geosciences Union - Fall Meeting 2006, San Francisco, CA, USA, 11–15 Dicembre 2006 (oral session).

Carbone, D., Jousset, P., Musumeci, C. (2007). Gravity steps at Etna and Merapi volcanoes. Instrumental effects or evidences of earthquake-triggered magma density changes?, XXIV IUGG General Assembly, Perugia, 02-13 July (oral presentation).

PIEZOMAGNETIC MOGI MODEL IN A VISCOELASTIC HALF-SPACE

Gilda Currenti

Isitituo Nazionale di Geofisica e Vulcanologia, Sezione di Catania
Email:currenti@ct.ingv.it

Abstract

Temporal changes in piezomagnetic field can arise from changes in magma pressure, evolution of the source geometry, or rheologic properties of the host rock. Especially in volcanic areas, the presence of inhomogeneous materials and high temperatures produce a lower effective viscosity of the Earth's crust that calls for considering anelastic properties of the medium. We have investigated time dependent piezomagnetic changes due to viscoelastic properties of the medium surrounding volcanic sources. Piezomagnetic properties are carried by grains of titano-magnetite, which occupies only a small fraction of ordinary rock volume and are supposed to be elastic, while the non-magnetic surrounding matrix is assumed to behave viscoelastically. Under this assumption, only the elastic/anelastic medium parameters show a viscoelastic behavior. From all the possible rheological models, we investigate two cases in which the bulk modulus is purely elastic and the shear modulus relaxes as: (i) a Maxwell solid and (ii) a standard linear solid (SLS). We applied the correspondence principle to the analytical elastic solutions for pressurized spherical sources in order to find out the time dependent piezomagnetic fields in a viscoelastic medium. In particular, the shear stress and hence the piezomagnetic field completely vanishes after the relaxation process for Maxwell rheology. For a SLS rheology, the piezomagnetic field is found to decrease over time and reach some finite offset value. These different behaviors could provide helpful hints in understanding the temporal evolution of piezomagnetic anomalies in volcanic regions.

Key words: piezomagnetic field, viscoelastic medium, Maxwell rheology, standard linear solid rheology.

Introduction

Studies on the deformation of a viscoelastic Earth were developed since 1970's in order to explain very slow crustal deformations with the duration time of several days to a few years (Peltier, 1974). The viscoelastic behavior of the earth associated with an earthquake was first investigated theoretically by Rundle (1978), in which the Earth consists of an elastic lithosphere underlain by a viscoelastic asthenosphere. Since the multi-layer earth model was rather difficult to deal with analytically, a more simple case study was anticipated in order to realize the behavior of a viscoelastic Earth. Especially in volcanic areas, the presence of inhomogeneous materials and high temperatures produce a lower effective viscosity of the Earth's crust that calls for considering anelastic properties of the medium. Bonafede et al. (1986) presented the crustal deformation due to the Mogi model in a viscoelastic half-space. They worked out analytical solutions for the displacements and associated stress fields induced by a pressure point source in a viscoelastic half-space and showed that the viscoelastic response may enhance the displacement at the ground surface requiring plausible overpressures. Lately, Dragoni and Magnanensi (1989) considered a spherical magma chamber, surrounded by a homogeneous shell of thermal metamorphic rocks, which is elastic dilatational and Maxwell deviatoric. Recently, investigations have been carried out by means of numerical methods which showed that rheological heterogeneities may be much more important than elastic heterogeneities (Folch 2000; Trasatti 2003). Therefore, it is well accepted that the rheological response of the medium can play an important role in the interpretation of long-term deformation.

Although several studies on the displacement and stress fields have been already performed, no investigations have been carried out to evaluate the viscoelastic response of piezomagnetic field. Since the piezomagnetization is proportional to the deviatoric stress, a question arises about the time dependent response of piezomagnetic field in a viscoelastic medium.

To fill this lack we investigated time dependent piezomagnetic changes due to viscoelastic properties of the medium surrounding volcanic sources. We extend volcanomagnetic and tectonomagnetic modeling to viscoelastic materials. Following Bonafede et al. (1986) scheme and applied it to Sasai's (1991a) solution for the piezomagnetic field in the elastic medium we derive an analytical solution of the

piezomagnetic field in a viscoelastic medium. We consider the piezomagnetic Mogi model (Sasai, 1991a) in terms of center of pressure and center of dilation sources. We adopted the rheology of a standard linear solid (SLS) and Maxwell solid for the shear modulus, while the bulk modulus is kept elastic. The analytical solutions in both the cases are compared to estimate the different behavior of the time piezomagnetic response due to the rheology assumption.

Method

For a linear viscoelastic material, the solution of the governing equations can be obtained from the elastic solution employing the correspondence principle (Fung 1965; Christensen 1971). The analytical solution of the elastic problem was devised by Sasai (1991a) for Mogi piezomagnetic model. The linear piezomagnetic law leading to the stress-magnetization relationship is given by:

$$\Delta J_i = \frac{3}{2}\beta\sigma'_{ij}J_j \qquad (1)$$

where σ'_{ij} is the deviatoric stress tensor, J and ΔJ are the magnetization of the material and its increment (i.e. piezomagnetization), while β is the stress sensitivity. The piezomagnetic potential W_i produced by the i-th component of the magnetization is:

$$W_i(r) = \iiint_V \Delta J_i \cdot \nabla\left(\frac{1}{\rho}\right) dV\,(r') \qquad (2)$$

where $\rho = |r - r'|$.

No piezomagnetic experiments have ever been made on the viscoelastic behavior of magnetized rocks. Piezomagnetic properties are carried by titano-magnetite, which occupies only a small portion of ordinary rocks. We suppose that titanomagnetite is elastic, while the non-magnetic surrounding matrix behaves viscoelastically. The piezomagnetization is determined simply by the stress field around titanomagnetites. Under this assumption, β and ΔJ are independent of the rheological behavior of host rocks. When the magnetic parameters β and J are homogeneous within the volume V, they are excluded from the integral sign. Therefore only σ'_{ij} determines the magnetic potential. If the analytic solution for the piezomagnetic potential of any linear elastic model is given, we can apply the correspondence principle to the elastic solution to obtain the viscoelastic behavior of the piezomagnetic field that leads to:

$$\tilde{w}_i(r,s) = \tilde{g}(s)\tilde{W}_i(r,s) \qquad (3)$$

where $\tilde{w}_i(r,s)$ is the Laplace-transformed piezomagnetic potential, *g(s)* is the source time function, and $\tilde{W}_i(r,s)$ indicates the function $W_i(r)$ in which λ and μ are replaced with the relaxation functions λ(s) and μ(s). The resulting expression is the Laplace transformed of the viscoelastic solution, which must be inverted in order to obtain the viscoelastic solution for the piezomagnetic potential in the time domain.

Our aim is to compare the physical behavior of a number of models coming from different rheologies. Among all the possible rheological models, we investigate two cases in which the bulk modulus is assumed to be elastic and the shear modulus relaxes as a: (i) standard linear solid (SLS) and (ii) Maxwell solid. This rheology accounts for keeping the elastic compressibility of the crust fixed, but at the same time allowing shear stresses to relax (Fernandez et al., 2001).

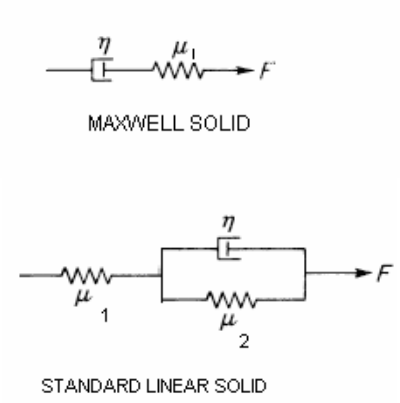

Fig. 1 – Linear viscoelastic models: Maxwell solid (a) and Standard Linear Solid (b).

The SLS behaves as an elastic solid in the limit of both high and low frequencies and can be represented by a mechanical analogue model combining a spring and a dashpot in parallel connected with a second spring in series (Fig.1). Instead, the Maxwell rheology is an elastic solid at high frequencies and a Newtonian fluid at low frequencies, and the analogue model is achieved by combining a spring and a dashpot element in series (Folch et al., 2000). The Laplace transform for the shear modulus in a SLS rheology is given by (Fung, 1965):

$$\tilde{\mu}(s) = \frac{\mu_1 s + \mu_1\mu_2/\eta}{s + (\mu_1 + \mu_2)/\eta} \qquad (4)$$

where μ_1 e μ_2 are the rigidity parameters and η is the viscosity. For the sake of simplicity, we assume $\mu_1=\mu_2$, therefore:

$$\tilde{\mu}(s) = \frac{\mu_1 s + \mu_1^2/\eta}{s + 2\mu_1/\eta} \qquad (5)$$

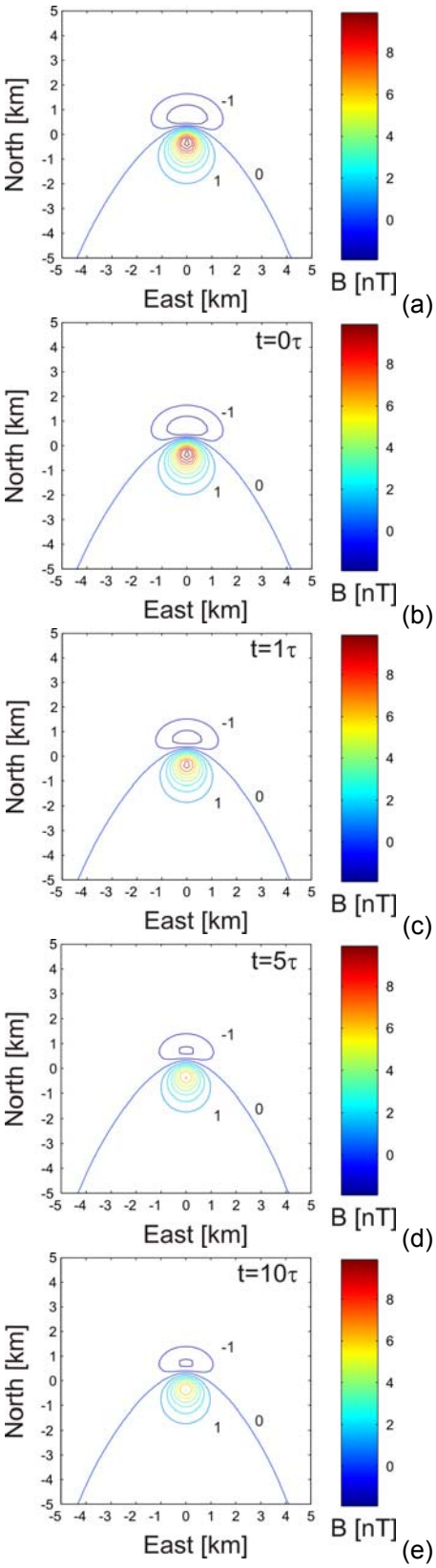

Fig. 2 - Piezomagnetic field of a Mogi source embedded in a Maxwell viscoelastic solid subjected to a pressure step changes. The elastic solution (a) coincides with the one obtained at t=0 (b).

When $\mu_1=0$, the SLS reduces to a Maxwell solid leading to:

$$\tilde{\mu}(s) = \frac{\mu_1 s}{s + \mu_1/\eta} \tag{6}$$

Under the assumption of an elastic bulk modulus:

$$K(s) = K \tag{7}$$

that yields to the following relation:

$$\lambda + \frac{2}{3}\mu_1 = \tilde{\lambda}(s) + \frac{2}{3}\tilde{\mu}(s) \tag{8}$$

from which the $\lambda(s)$ can be computed as:

$$\tilde{\lambda}(s) = \lambda + \frac{2}{3}\mu_1 - \frac{2}{3}\tilde{\mu}(s) \tag{9}$$

Besides the rheology assumption, two different spherical sources are taken into account: (i) center of dilation (COD) where the incremental source volume ΔV is kept constant, and (ii) center of pressure (COP) where the incremental pressure ΔP applied to the source surface remains constant.

Mogi Piezomagnetic solution in Viscoelastic Medium

The piezomagnetic field due to the Mogi model was obtained by Sasai (1991a), which was a corrected version of the point source solution by Sasai (1979). The piezomagnetic potential at observation point (x_0,y_0,z_0) due to a Mogi source centred at (0, 0, D) is given by:

$$W_x = \pi\beta J_x C\left[\frac{\mu}{\lambda+\mu}\left(\frac{x_0}{\rho_0} - \frac{x_0}{\rho_3{}^3}\right) + 6H\left(\frac{3x_0 D_3}{\rho_3{}^5}\right) + \right.$$
$$\left. + \begin{cases} \left(\frac{x_0}{\rho_1{}^3} - \frac{x_0}{\rho_2{}^3}\right) & (H > D) \\ 0 & (H < D) \end{cases}\right] \tag{10}$$

$$W_z = \pi\beta J_z C\left[-\frac{\mu}{\lambda+\mu}\left(\frac{D_1}{\rho_1{}^3} - \frac{D_3}{\rho_3{}^3}\right) + 6H\left(-\frac{1}{\rho_3{}^3} + \frac{3D_3{}^2}{\rho_3{}^5}\right) + \right.$$
$$\left. + \begin{cases} -\left(\frac{D_1}{\rho_1{}^3} + \frac{3D_2}{\rho_2{}^3}\right) & (H > D) \\ 0 & (H < D) \end{cases}\right] \tag{11}$$

where

$$\rho_i = \sqrt{\left(x_0{}^2 + y_0{}^2 + D_i{}^2\right)} \tag{12}$$

$$D_1 = D - Z_0,$$
$$D_2 = 2H - D - z_0,$$
$$D_3 = 2H + D - z_0 \tag{13}$$

and C is the moment of the nucleus, which is proportional to the pressure changes for the COP model and to the volume changes for the COD model. According to Sasai (1979), the normal stress σ_{RR} across the source wall is given by:

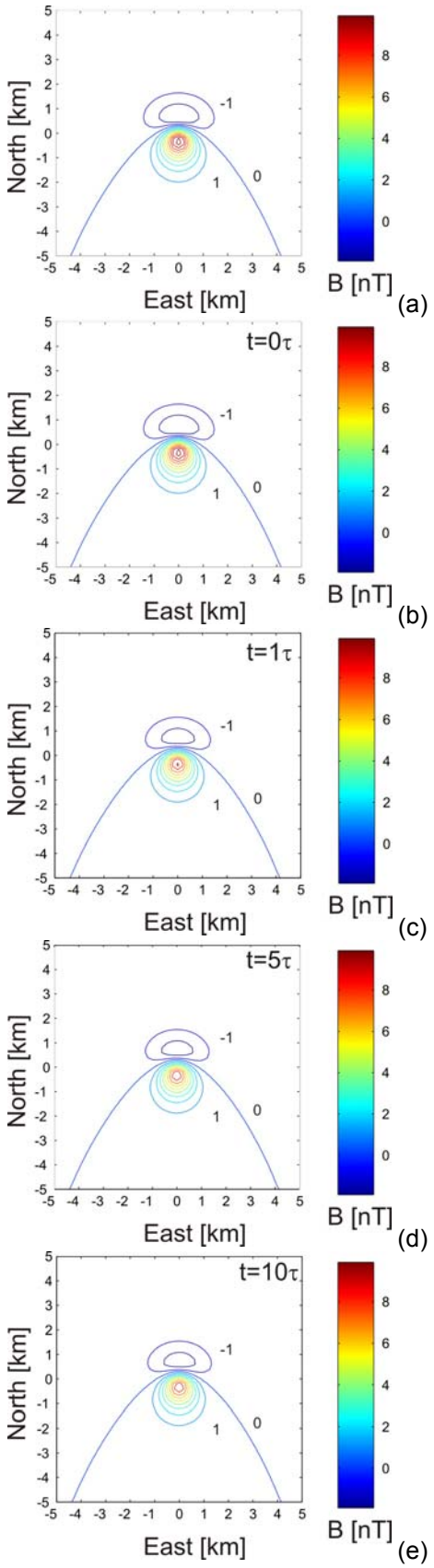

Fig. 3 - Temporal piezomagnetic changes due to a Mogi source embedded in a SLS rheology subjected to a pressure step changes. The elastic solution (a) coincides with the one obtained at t=0 (b).

$$\sigma_{RR} = \frac{2C}{a^3} \tag{14}$$

which is balanced by the internal hydrostatic pressure ΔP. Following the standard sign convention for stress (i.e. compression is negative), it leads to:

$$C = -\tfrac{1}{2} a^3 \Delta P \tag{15}$$

The increment of the source radius Δa, when an internal hydrostatic pressure ΔP is applied, is given by the displacement at an arbitrary point on the source surface:

$$\Delta a = \left| u_z(0,0,D-a) \right| = \frac{C}{2\mu}\frac{1}{a^2} \quad \left(\frac{a}{D} << 1 \right) \tag{16}$$

The incremental volume change is estimated as:

$$\Delta V = 4\pi a^2 \Delta a = \frac{2\pi}{\mu} C \tag{17}$$

Thus the moment C can be expressed in terms of ΔV or ΔP as:

$$C = \frac{\mu}{2\pi}\Delta V = -\frac{a^3}{2}\Delta P \tag{18}$$

Therefore, we used two different definition of C in the case of COP and COD model. It is worth to note that C is dependent on u in COD model.

Piezomagnetic Parameters	***Symbol***	***Value***
Average Magnetization	J	2.5 A/m
Curie Depth	H	15000 m
Magnetic Inclination	I0	53°
Magnetic Declination	D0	1°
Rigidity	μ	30 GPa
Viscosity	η	1016 Pa*s
Stress Sensitivity	β	0.0001 bar-1

Table I – Medium Parameter

Mogi Model Parameters	***Value***
Volume change	106 m3
Depth of the sphere center from the surface	1000 m
Pressure change	100 MPa
Radius	500 m

Table II – Geometry parameter for the COD and COP models.

COP viscoelastic solution

We investigated the piezomagnetic behavior for the COP model under Maxwell and SLS rheology assumptions in a medium having shear modulus μ_1= 30 GPa and viscosity η=10^{16} Pa*s (Table I). A Mogi source with 500 m radius and pressure 100 MPa located at 500 m depth was considered (Table II). The elastic and magnetic parameters of the medium surrounding the source are reported in Table I. We have also to define a specific source function to model the time history of the COP model. We consider an Heaviside step function H(t):

$$g(t) = H(t) = \begin{cases} 0 & t < 0 \\ 1 & t \geq 0 \end{cases} \qquad (19)$$

which represents an abrupt change in pressure at t=0 and whose Laplace-transform is 1/s. Applying the correspondence principle to Eqs. (10) and (11), only the first terms (i.e. μ/(λ+ μ)) contain λ(s) and μ(s), whereas the others are time-invariant since they are independent from λ(s) and μ(s). This implies that a portion of the piezomagnetic field is time-independent and that it will never vanish. We computed the viscoelastic solution of the piezomagnetic field for a Maxwell solid rheology at different time windows t=0, t=τ, t=5τ, t=10τ, where τ is the characteristic time given by τ=μ/η. The viscoelastic solution at t=0 (Fig. 2a) coincide with the elastic solution (Fig. 2). The magnetic anomaly decreases in amplitude until it reaches a finite offset. A decrease of about 4 nT in proximity of the positive anomaly is observed.

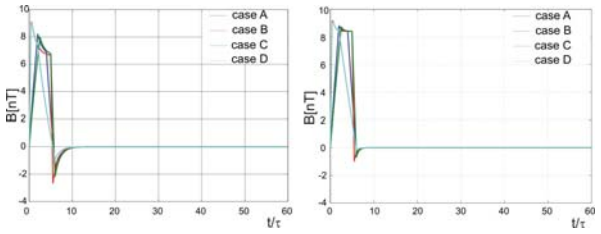

Fig. 4 - Piezomagnetic field of a COP source subjected to a trapezoidal pressure changes in a Maxwell (a) and SLS (b) rheology.

The steady-state of the total piezomagnetic field is reached in less than 10τ. A similar behavior is obtained for the SLS rheology (Fig. 3). Also in this case the piezomagnetic solution at t=0 is equal to the elastic solution and decreases over time. The decay in amplitude of the piezomagnetic field is different from the one obtained for the Maxwell rheology. A decrease of about 2 nT at the center of the positive anomaly is observed from the initial value at t=0. Indeed, the incremental pressure ΔP is continuously applied to the source surface and always generates shear stress within the viscoelastic medium. Hence the source sphere continues to expand indefinitely.

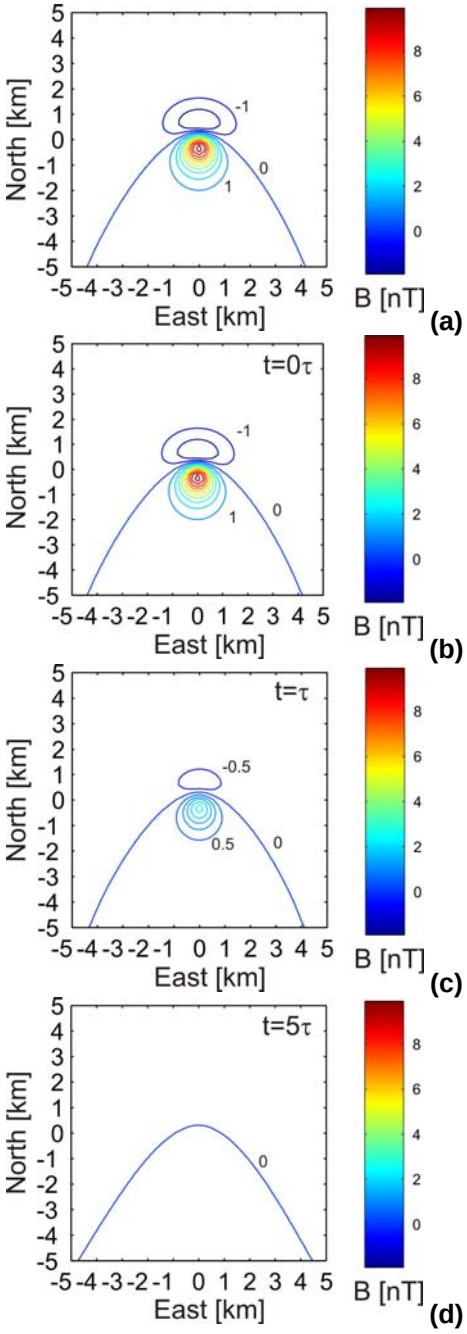

Fig. 5 – Time dependent piezomagnetic anomaly due to a COD source in a Maxwell viscoelastic solid subjected to a volume step changes. The elastic solution (a) coincides with the one obtained at t=0 (b).

To get a more realistic picture, a source time history having a trapezoidal shape is assumed (Fig. 4):

$$g(t)=\Delta P\left\{\frac{t}{t_1}\left[1-H(t-t_1)\right]+H(t-t_1)-H(t-t_2)+\frac{t_3-t}{t_3-t_2}\left[H(t-t_2)-H(t-t_3)\right]\right\} \quad (20)$$

whose Laplace transform is:

$$\tilde{g}(s)=\frac{\Delta P}{s^2}\left(\frac{1-e^{-st_1}}{t_1}+\frac{e^{-st_3}-e^{-st_2}}{t_3-t_2}\right) \quad (21)$$

The pressure increases linearly in time from t=0 to $t=t_1$, keeps constant for $t_1<t<t_2$ and decay linearly for t2<t<t3. Trapezoidal shape function allows for describing pressurization followed by depressurizzation of magmatic source, usually observed in volcanic areas. Four different values of t_1, t_2, and t_3 have been considered to investigate how they affect the evolution of the piezomagnetic field. Curve (A) is for $t_1=2\tau$, $t_2=4\tau$, $t_3=6\tau$; curve (B) for $t_1=\tau/2$, $t_2=5\tau$, $t_3=5.5\tau$; curve (C) for $t_1=2.5\tau$, $t_2=5\tau$, $t_3=6\tau$; curve (D) for $t_1=\tau/2$, $t_2=2\tau$, $t_3=6\tau$. On the ground surface at the centre of the positive anomaly, the piezomagnetic field changes sharply during the rise time and fall time of the trapezoidal function. The maximum change is obtained for the B and D cases, which present the sharper rise time. The evolution of the piezomagnetic field for the SLS and Maxwell rheologies is different, even if the field vanishes to zero for $t>10\tau$.

COD viscoelastic solution

In an elastic medium the pressure change can be related to the volume change through the Lamé constants and, therefore, the stress and the piezomagnetic field produced by COD coincide with those generated by COP. When viscoelasticity is taken into account, the solutions differ from each other (Bonafede et al., 1986). A volume change is chosen in a way to assure the same piezomagnetic field at t=0. Using eq. (18), the incremental source volume can be estimated as:

$$\Delta V = 4\pi a^2 \Delta a = \frac{2\pi}{\mu} C = a^3 \pi \frac{\Delta P}{\mu} \quad (22)$$

that gives a volume change of $1.039*10^6$ m^3. If we apply the correspondence principle to eqs. (10) and (11), then all the three terms depend on λ(s) and μ(s) as: (i.e. μ and $\mu^2/(\lambda+\mu)$).

The solution at time windows t=0, t=τ, t=5τ, t=10τ are reported in Fig. 5 for the Maxwell rheology.

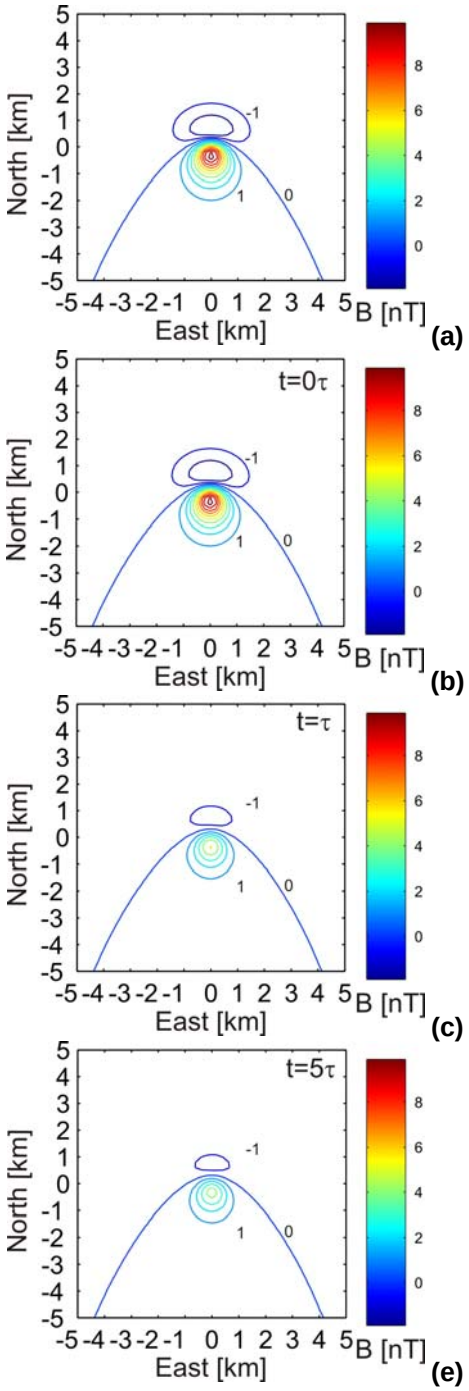

Fig. 6 - Piezomagnetic field of a Mogi source embedded in a SLS rheology subjected to a volume step changes. The elastic solution (a) coincides with the one obtained at t=0 (b).

The piezomagnetic field completely vanishes after the relaxation process, since the shear stress is completely relaxed. Instead, for a SLS rheology the piezomagnetic field is found to decrease over time and reaches a finite offset (Fig. 6). As in the COP model, we consider a trapezoidal time history for the cases (A, B, C, D) with different rise and fall times (Fig. 7). The temporal evolution of the piezomagnetic field for the Maxwell and SLS rheologies at a point where

the magnetic anomaly at t=0 shows the maximum amplitude is reported. The piezomagnetic anomaly evolves in a different way for the two rheologies even if both show a reverse in sign of the computed anomaly.

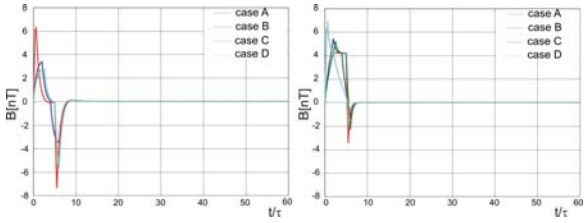

Fig. 7 - Piezomagnetic field of a COD source subjected to a trapezoidal volume changes in a Maxwell (a) and SLS (b) rheology.

Conclusions

The time dependent piezomagnetic changes due to Mogi sources embedded in a viscoelastic medium were computed. In agreement with previous studies on viscoelastic deformation, the presence of viscoelactic material also produces remarkable time-dependent magnetic effects in COD and COP models. The relaxation of the shear stress (Dragoni and Magnanensi, 1989) makes the piezomagnetic field vanish when a Maxwell rheology is considered. For a SLS rheology, the piezomagnetic solution decays exponentially and reaches a finite offset. In the case of COP source, even for a Maxwell solid, the solution remains finite because it contains some terms multiplied by the time history g(t).

The proposed method can be easily extended to other tectonomagnetic models whose analytical elastic solutions have been already devised, i.e. inclined shear and tensile faults (Utsugi et al., 2000) and a uniform circular load or the dam-magnetic effect (Sasai, 1986). However, a viscoelastic half-space is a too crude approximation to the actual Earth. More realistic would be a layered earth with the mixture of elastic and viscoelastic ones. For a point source or strain nuclei of elastic dislocation problems, we can obtain analytic formulas in a layered earth with the propagator matrix technique which was employed by Okubo and Oshiman (2004). Then the present method will be available to investigate the piezomagnetic field in a viscoelastic Earth. This may be a rather laborious work, but should make a breakthrough to further tectonomagnetic studies.

References

Bonafede, M., M. Dragoni, F. Quareni, 1986, Displacement and stress fields produced by a pressure source in a viscoelastic half-space: application to the study of ground deformation and seismic activity at Campi Flegrei, Italy, Geophys. J. R. astr. Soc., 87, 455-485.

Bonafede, M., 1990, Axi-symmetric deformation of a thermo-poro-elastic half-space: inflation of a magma chamber, Geophys. J. Int., 103, 289-299.

Dragoni, M. and Magnanensi, C.,2001 Displacement and stress produced by a pressurized, spherical magma chamber, surrounded by a viscoelastic shell. Phys. Earth Planet. Inter, 56, 316-328.

Fernandez, J., Tiampo K. F. and Rundle J. B., 2001, Viscoelastic displacement and gravity changes due to point magmatic intrusions in a gravitational layered solid earth, Geophys. J. Int. 146, 155–170.

Folch, A., Fernandez, J., Rundle, J.B., Marti, J., 2000, Ground deformation in a viscoelastic medium composed of a layer overlying a half-space: a comparison between point and extended sources, Geophys. J. Int. 140, 37–50

Fung, Y. C., 1965, Foundations of Solid Mechanics, Prentice-Hall, Englewood Cliffs. Japanese traslation by Y. Ohashi, S. Murakami and N. Kamiya, 1970, Baifukan, 524 pp.

Lee, E., 1955, Stress analysis in viscoelastic bodies, Quart. J. Appl. Math., 13, 183-190.

Maruyama, T., 1964, Statical elastic dislocations in an infinite and semi-infinite medium, Bull. Earthq. Res. Inst., Univ. Tokyo, 42, 289-368.

Mindlin, R. D. and D. H. Cheng, 1950, Nuclei of strain in the semi-infinite solid, J. Applied Phys., 21, 926-930.

Okubo, A. and N. Oshiman, 2004, Piezomagnetic field associated with a numerical solution of the Mogi model in a non-uniform elastic medium, Geophys. J. Int., 159, 509-520.

Rundle, J. B., 1978, Viscoelastic crustal deformation by finite quasi-static sources, J. Geophys. Res., 83, 5939-5945.

Sasai, Y., 1979, The piezomagnetic field associated with the Mogi model, Bull. Earthq. Res. Inst., Univ. Tokyo, 54, 1-29.

Sasai, Y., 1980, Application of the elasticity theory of dislocations to tectonomagnetic modelling, Bull. Earthq. Res. Inst., Univ. Tokyo, 55, 387-447.

Sasai, Y., 1986, A Green's function for tectonomagnetic problems in an elastic half-space, J. Geomag. Geoelectr., 38, 949-969.

Sasai, Y., 1991a, Piezomagnetic field associated with the Mogi model revisited: analytic solution for finite spherical source, J. Geomag. Geoelectr., 43, 21-64.

Sasai, Y., 1991b, Tectonomagnetic modeling on the basis of the linear piezomagnetic effect, Bull. Earthq. Res. Inst., Univ. Tokyo, 65, 585-722.

Trasatti, E., Giunchi, C., & Bonafede, M., 2003. Effects of elastic and rheological layering on ground deformation in volcanic regions, J. Volcan. Geotherm. Res.,122, 89-110.

Utsugi, M., Y. Nishida, Y. Sasai, 2000, Piezomagnetic potentials due to an inclined rectangular fault in a semi-infinite medium, Geophys. J. Int., 140, 479-492.

STATIC STRESS CHANGES INDUCED BY MAGMATIC INTRUSIONS DURING THE 2002-2003 ETNA ERUPTION

*Gaetana Ganci * and Gilda Currenti*

Isitituo Nazionale di Geofisica e Vulcanologia, Sezione di Catania
** Email: ganci@ct.ingv.it*

Abstract

The understanding of shallow intrusive processes during 2002–2003 Etna eruption, as well as the complex interaction between the magma intrusive events and the tectonic response of the volcano eastern flank, has been improved by the numerical modeling of deformation data and by the estimation of changes in the static Coulomb stress due to magmatic intrusion. Previous inversions of the ground deformation patterns clearly indicate a composite mechanism of intrusion on both the southern and north-eastern flanks of the volcano. These inversions used a homogeneous elastic half-space model, although geological data and seismic tomography indicate that Mt Etna is elastically inhomogeneous, and that rigidity layering and heterogeneities are likely to affect the magnitude and pattern of the deformation field. To overcome these limitations, we use the finite-element method (FEM) to provide a more realistic model, which considers topographic effects as well as a complicated distribution of material properties. Computations on the stress changes determined by the numerical models are also performed to investigate the complex interaction between dike emplacement and the mechanisms responsible for the kinematics of the east flank.

Key words: Coulomb stress changes, ground deformation, finite element method, Etna volcano.

Introduction

The 2002-2003 Etna eruption was a highly complex eruptive event, as it simultaneously consisted of lateral activity on the north-east flank and eccentric activity on the south flank [Neri et al., 2005]. During the night of 26-27 October, 2002, an intense seismic sequence heralded and accompanied the opening of two eruptive fracture systems on both the north-east and south flanks of Etna volcano (Fig. 1). The space-time pattern of epicenters showed an almost stationary distribution in the central part of the volcano on October 26 during the first hours of the swarm and a very clear migration towards the North-East Rift in the early morning of 27 October [Barberi et al., 2004]. After a decrease in the daily earthquake rate, a sharp resumption due to the activation of new seismic volumes in the south-east flank was observed on October 29. The seismicity was mainly related to the magma intrusion along the North-East Rift, although the highest seismic releases were associated with the activation of two fault systems: (i) the Pernicana Fault, which is a local tectonic feature, and (ii) the Timpe Fault System, which represents the inland extension of the Malta Escarpment regional fault. In concomitance with the seismic crisis, during a 48-h period encompassing the beginning of the eruption, marked ground deformation was recorded through GPS and tilt permanent stations. Aloisi et al. [2003] determined that the geodetic observations were consistent with a response of the edifice to a composite mechanism of intrusion on both the southern and northeastern flanks of the volcano.

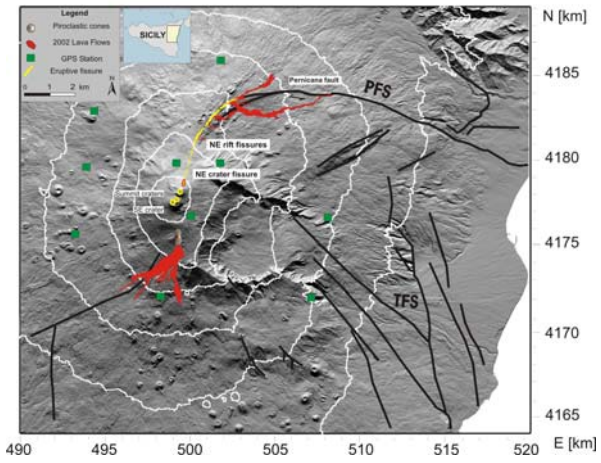

Fig. 1 - Schematic map showing the area affected by the 2002-2003 Etna eruption. Black solid lines trace the main faults on the edifice: PFS, Pernicana Fault System and TFS Timpe Fault System (after Walter et al., 2005).

Despite the clear sequence of volcano-tectonic events and the quantity of data collected, the interaction between magmatic events and tectonic processes responsible for the kinematics of the seismogenic structures occurring during

the 2002-2003 eruption is still under debate. The large recorded deformation pattern of the east flank occurred in response to the intrusive event, which was also responsible for the reactivation of the Pernicana Fault. Stress changes associated with dike intrusions are one of the basic mechanisms responsible for the kinematics of the east flank.

We use the finite-element method (FEM) to provide a more realistic model, which considers topographic effects as well as a complicated distribution of material properties. Computations on the stress changes determined by the geodetic data inversion [Aloisi et al., 2003; 2006] were performed to investigate the interaction between the dike intrusions and the fault systems that were reactivated soon after.

The Numerical Model

A fully 3D finite element simulation is performed to study in a more realistic way the ground deformations observed on Mt Etna during the onset of the 2002-2003 eruption. We investigate how topography and complex medium heterogeneity can affect the results. The modeling is conducted using the Lithomop finite element code [Williams and Wadge, 2000]. The source geometry and the dislocation parameters of the intrusive dikes are based on the results of geodetic data inversion [Aloisi et al., 2003]. The elastic parameters were estimated using VP and VS wave velocities inferred from seismic tomography [Chiarabba et al., 2000]. A Poisson's ratio equal to 0.25 is assumed that is a reasonable approximation on Mt Etna. In such a case, the Young's modulus, E, is related to medium density ρ and seismic wave velocity VP through the following relation:

$$E = \frac{5}{6}\rho\, V_P^2 \qquad (1)$$

Using a medium density of 2400 kg/m3 the Young modulus varies in the range from 11.5 GPa at shallower depth to 133 GPa at greater depth.

A good approach to estimate how medium heterogeneity and topography may affect the solutions is to evaluate each one separately and compare the results. Therefore, we conducted four numerical simulations in which we considered: (i) a homogeneous elastic medium with a flat surface (HomFlat), (ii) a homogeneous elastic medium with the real topography of Mt Etna (HomTopo), (iii) an elastic heterogeneous medium with a flat surface (HetFlat), and (iv) an elastic heterogeneous medium with the real topography (HetTopo).

Stress Changes

To better understand the interaction between tectonic and intrusive processes, we analyzed the stress changes computed by the numerical models along the North-East Rift zones, the Pernicana Fault, and the Timpe Fault System. We computed the horizontal normal stress changes to study the stress transferred onto the North-East Rift dike, while we computed the Coulomb stress changes to investigate the role magmatic processes play in the volcano's eastern flank movement. We computed the induced stress by means of Coulomb failure stress changes defined by:

$$\Delta CFF = \Delta\tau + \mu\left(\Delta\sigma_n + \Delta P\right) \qquad (2)$$

where $\Delta\tau$ is the shear stress in the direction of slip on the receiver fault, $\Delta\sigma n$ is the normal stress change, μ is the friction coefficient and ΔP is the pore pressure change. Based on the Coulomb failure criterion, failure on a fault is favored if the Coulomb stress change is positive and discouraged if the Coulomb stress change is negative [Cocco and Rice, 2002]. The value at which the Coulomb failure criterion is met is not known, but recent studies point out that Coulomb stress changes higher than 1 bar are considered to be significant [Toda et al. 1998].

North-East Rift

The changes in the state of stress generated by the southern dike could have affected the likelihood for the intrusion propagating along the North-East Rift. To investigate a possible interaction between these subsequent intrusive events, we examined the stress transfer associated with the southern dike intrusion onto the North-East Rift. Following the standard sign convention for stress (i.e. extension is positive), the horizontal normal stress changes on the North-East Rift were computed for all the models HomFlat, HomTopo, HetFlat and HetTopo (Fig. 2a-d) on a map view at 1000 m bsl. Besides the amplitude and the shape of stress patterns, all the numerical models show a positive stress change area around the North-East Rift. The HomTopo and HetTopo numerical models demonstrate how the stress pattern is affected by the Mt Etna topography. The medium heterogeneity strongly influences the amplitude of the field because of the lower value assigned to the Young's modulus at shallower depth with respect to the homogeneous models (Fig. 4).

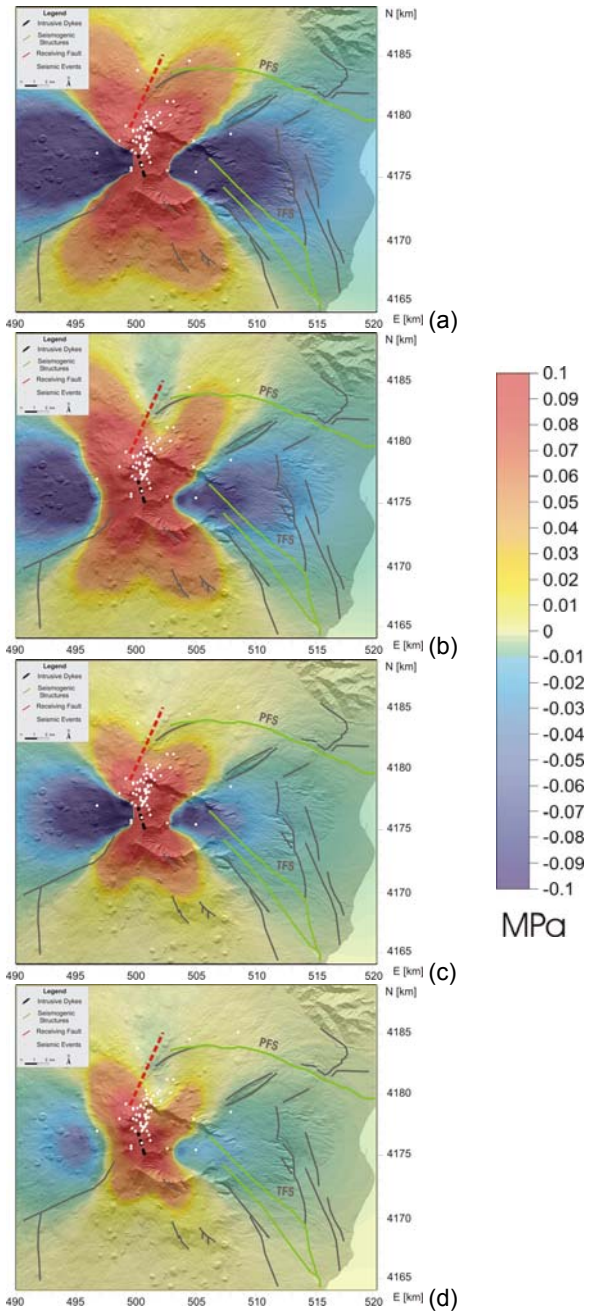

Figure 2 - Horizontal normal stress changes induced by the southern dike intrusion (black dashed line) on the North-East Rift (red dashed line) for HomFlat (a), HomTopo (b), HetFlat (c), and HetTopo (d) numerical models. The seismic events (white circles) accompanying the dike propagation are also reported.

The southern dike intrusion produced a horizontal normal stress gradient (more than 0.1 MPa) along the N24°E striking dike. The positive stress change in the northeastern area shows that the vertical uprising dike in the southern flank of the volcano generated an extensional stress field, which promoted the lateral intrusion propagating along the pre-existing crustal fracture system of the North-East Rift.

Pernicana Fault and Timpe Fault System

We resolved the stress tensor generated by both the southern and northern dike intrusions onto the mapped structural trends of the Pernicana Fault and Timpe Fault System.

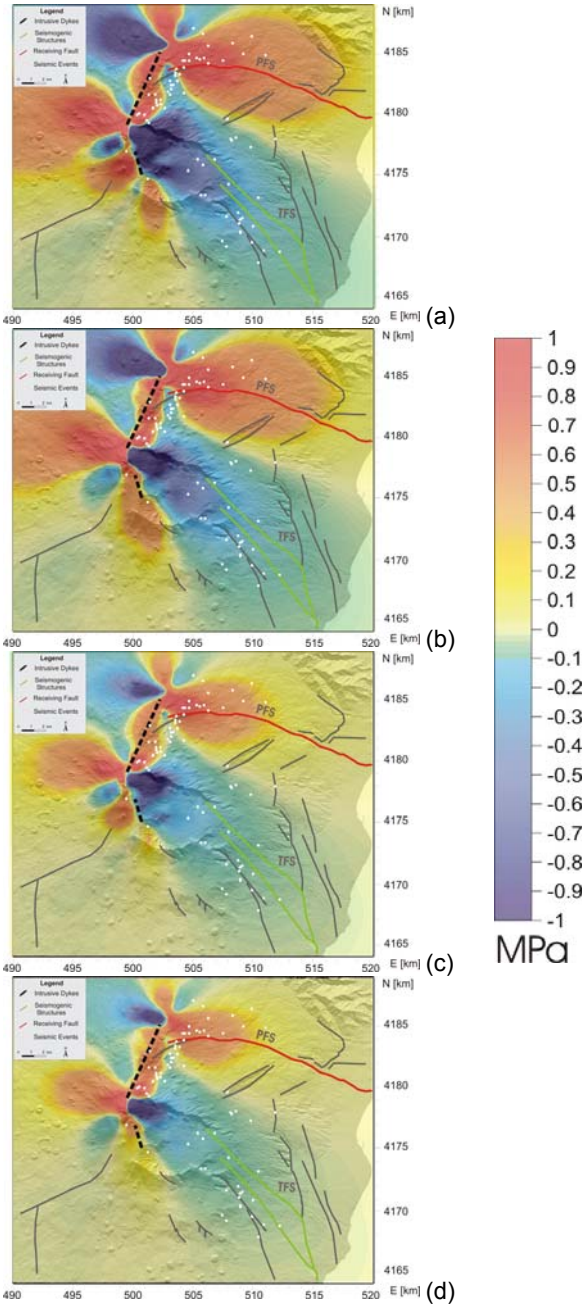

Figure 3 - Map view of Coulomb stress changes generated by the southern and northern dike intrusions (black dashed lines) and resolved onto Pernicana Fault (red line). The fault is mapped by a vertical plane oriented 100N.

Therefore, we computed the stress changes, generated by the southern and northern dike intrusions, onto a vertical plane oriented N100° with left lateral motion for the Pernicana Fault and

onto a vertical plane oriented N145° with right lateral motion for the Timpe Fault System [Walter et al., 2005]. The Coulomb stress changes were computed on a surface at 1000 m depth for the Pernicana Fault and at 3750 m for the Timpe Fault System, corresponding to the mid-depths of the seismic faulting, respectively. The heterogeneity and the topography strongly perturb the Coulomb stress changes. Effects due to topography are mostly evident in the summit area (Fig. 3a-d, 4a-d) and do not affect the foot of the volcanic edifice. Instead, the medium heterogeneity influences the magnitude of the stress change which is very sensitive to the variations in the crustal layering of rigidity [Zhao et al., 2004]. At shallower depth, where the shear modulus reaches a low value (4.6 GPa), the stress change values of the heterogeneous models can decrease by about 20 per cent compared with the homogeneous models. Positive Coulomb stress changes well match the seismic pattern and values less than 1 bar are obtained along both the Timpe Fault System and the Pernicana Fault. Therefore, the structures have reached a critical state and small stress perturbations were enough to encourage the faults to slip.

Conclusions

Our results show that heterogeneity and topography engender deviations from analytical results in the stress fields produced by the intrusive dikes on the southern and northeastern flanks under elastic conditions; however, such perturbations are more significant in the volcano summit and disappear some km away.

The intrusion on the southern flank was able to produce an extensional stress field that favoured the magma propagation along the North-East Rift. Lavas erupted from the southern fissure differ from those erupted along the North-East Rift [Andronico et al., 2004].

Such features suggest that two different magmas reached the surface through independent pathways connected to distinct fracture systems [Monaco et al., 2005]. Magma erupted from the northeastern fissure was a partially degassed magma normally residing within the central conduits and the shallow plumbing system. Therefore, this magma was already filling the North-East Crater conduit, as indicated by summit eruptive activity observed several months prior to the eruption [Andronico et al., 2004]. The vertical uprising dike under the summit craters could have produced cracks encouraging the magma from the North-East Crater conduit to intrude along the North-East Rift zone.

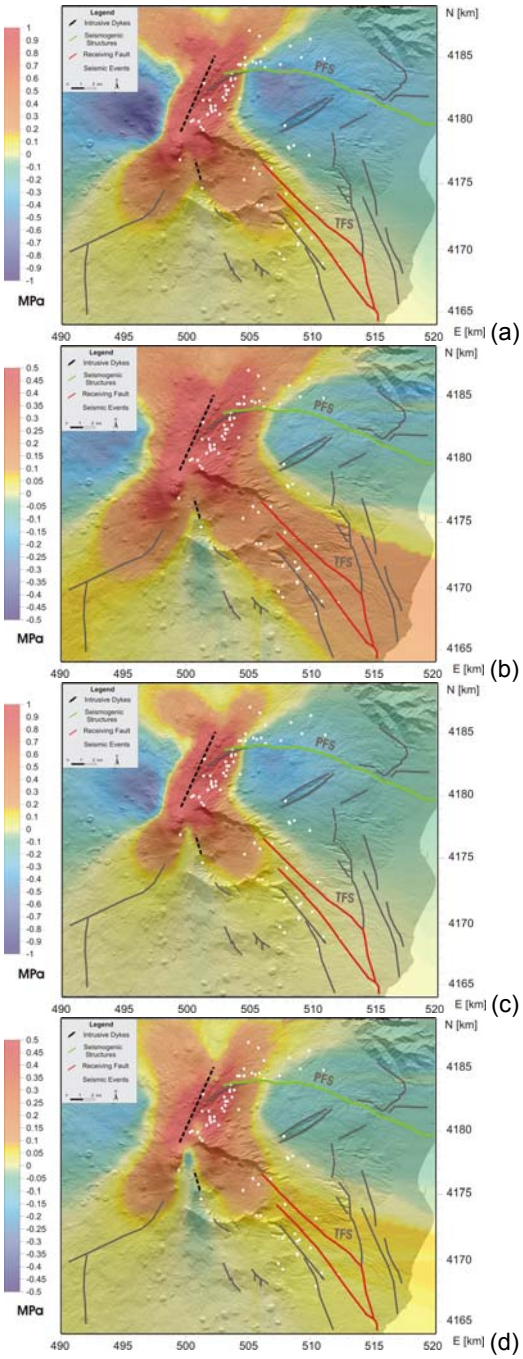

Figure 4 - Coulomb stress changes induced by the southern and northern dike intrusions (black dashed lines) for the HomFlat (a), HomTopo (b), HetFlat (c), HetTopo (d) models. The stress tensor is projected onto Timpe Systems (red lines) represented with a vertical plane oriented 145N.

Computations of Coulomb stress changes show that seismicity well matches areas of increased static stress changes caused by the intrusive event along the southern and northeastern flanks.

Extension along the North-East Rift zone was followed by the left-lateral movement of the Pernicana Fault and the right-lateral movement along the Timpe Fault System. The presence of

medium heterogeneity strongly affects the amplitudes of the static stress changes. Since recent studies on stress triggering effects point out that a few bars could increase or decrease seismicity in fault areas, the assumption on medium properties is a crucial point. All the numerical models produce stress maps that indicate that the Timpe Fault System and the Pernicana Fault are encouraged to slip. Particularly, the HetTopo numerical model, which includes the topography and medium heterogeneity, predicts static stress changes of a few bars. This is an indication that the structures were already in a critical state and the eruption has advanced the occurrence time of fault ruptures.

References

Aloisi, M., A. Bonaccorso, S. Gambino, M. Mattia, and G. Puglisi (2003), Etna 2002 eruption imaged from continuous tilt and GPS data, Geophys. Res. Lett., 30, 2214.

Aloisi M., A. Bonaccorso, S. Gambino (2006), Imaging composite dike propagation (Etna, 2002 case). J. Geophys. Res., 111, B06404, doi:10.1029/2005JB003908.

Andronico D., Branca S., Calvari S., Burton M., Caltabiano T., Corsaro R.A., Del Carlo P., Garfì G., Lodato L., Miraglia L., Murè F., Neri M., Pecora E., Pompilio M., Salerno G., Spampanato L., (2005), A multi-disciplinary study of the 2002–03 Etna eruption: insights into a complex plumbing system, Bull. Volcanol., 67, 314–330, DOI 10.1007/s00445-004-0372-8.

Barberi G., Cocina O., Maiolino V., Musumeci C., Privitera E. (2004), Insight into Mt. Etna (Italy) kinematics during the 2002–2003 eruption as inferred from seismic stress and strain tensors. Geophys. Res. Lett, 31, L21614, doi:10.1029/2004GL020918.

Chiarabba, C., Amato, A., Boschi, E., & Barberi, F., 2000. Recent seismicity and tomographic modeling of the Mount Etna plumbing system, J. Geoph. Res., 105(B5), 10,923–10,938.

Cocco, M., and J. R. Rice (2002), Pore pressure and poroelasticity effects in Coulomb stress analysis of earthquake interactions, J. Geoph. Res., 107(B2), 2030, doi:10.1029/2000JB000138.

Gresta, S., Ghisetti, F., Privitera, E., and Bonanno, A., (2005), Coupling of eruptions and earthquakes at Mt. Etna (Sicily, Italy): A case study from the 1981 and 2001 events. Geophys. Res. Lett., 32, L05306, doi:10.1029/2004GL021479.

Monaco, C., Catalano, S., Cocina, O., De Guidia, G., Ferlito, C., Gresta, S., Musumeci, C., Tortorici, L., (2005), Tectonic control on the eruptive dynamics at Mt. Etna Volcano (Sicily) during the 2001 and 2002–2003 eruptions, J. Volcanol Geotherm Res., 144, 211 – 233.

Neri, M., Acocella, V., Behncke, B., Maiolino, V., Ursino, A., Velardita, R. (2005), Contrasting triggering mechanisms of the 2001 and 2002–2003 eruptions of Mount Etna (Italy), J. Volcanol. Geotherm. Res., 144, 235– 255, doi:10.1016/j.jvolgeores.2004.11.025.

Okada, Y. (1992), Internal deformation due to shear and tensile faults in a half-space, Bull. Seism. Soc. Am., 82, 1018-1040.

Patanè, D., G. Barberi, O. Cocina, P. De Gori, C. Chiarabba, (2006), Time-resolved seismic tomography detects magma intrusions at Mount Etna, Science, 313, 821.

Toda, S., Stein, R.S., Reasenberg, P.A., Dieterich, J.H., (1998), Stress transferred by the 1995 Mw=6.9 Kobe, Japan, shock: effect on aftershocks and future earthquake probabilities, J. Geophys. Res., 103, B10, 24543-24565.

Walter, T. R., V. Acocella, M. Neri, and F. Amelung (2005), Feedback processes between magmatic events and flank movement at Mount Etna (Italy) during the 2002–2003 eruption, J. Geophys. Res., 110 (B10205), doi:10.1029/2005JB003688.

Williams, C.A., G. Wadge (2000), An accurate and efficient method for including the effects of topography in three-dimensional elastic models of ground deformation with applications to radar interferometry, J. Geophys. Res., 105 (B4), 8103-8120.

Zhao, S., Muller, R. D., Takahashi, Y., Kaneda, Y. (2004), 3-D finite-element modelling of deformation and stress associated with faulting: effect of inhomogeneous crustal structures, Geophys. J. Int., 157, 629–644 doi: 10.1111/j.1365-246X.2004.02200.x

3D NUMERICAL MODELLING OF INTRUSIVE EVENTS FORERUNNING THE 2001 ETNA ERUPTION

*Gilda Currenti *, Gaetana Ganci and Danila Scandura*

Isitituo Nazionale di Geofisica e Vulcanologia, Sezione di Catania
** Email: currenti@ct.ingv.it*

Abstract

A 3D finite elements models were carried out in order to evaluate the ground deformation caused by the 2001 dike intrusion occurred at Etna volcano. The FE method allows for considering the medium heterogeneity and the real topography of the volcano. Firstly, we validate the method in a homogeneous elastic half-space and compared the results with those obtained from analytical dislocation models. Then, several numerical models were performed to appreciate how the complex distribution of elastic medium parameters and the topography make the numerical results differ from the simple analytical solutions.

Key words: Finite Element Method, real topography, heterogeneous medium, Etna volcano.

Introduction

The action of volcanic source and the mechanism of magma uprising, related to intrusive processes characterizing the emplacement of dikes, are often responsible of the ground deformation. The dislocation theory has been usually applied to model the ground deformation due to dike intrusions under oversimplified assumptions (Okada, 1992; Bonaccorso and Davis, 2004) In fact analytical solution are available only for rectangular or circular shaped source in an homogeneous half-space medium. The introduction of real topography and medium heterogeneity of the volcanic edifice requires the use of numeric technique, such as Finite Element Method (FEM).

In the present study, we investigated the effects of the tensile crack at Mt Etna volcano. Computations are carried out with the FE software COMSOL. We focused on the analysis of a homogenous, isotropic and half-space medium, in order to validate the solution accuracy with respect to the mesh resolution. Firstly, the numerical results were compared to the analytical ones computed using the dislocation theory (e.g., Okada, 1992). Then, a 3D analysis was performed, by introducing the real topography of Mt Etna and modelling the intrusive events forerunning the 2001 eruption, in order to examine the effect of the topography on the deformation field. In addition to the topography, the effects of the elastic medium heterogeneities were included considering a 3D complex distribution of medium properties in terms of Young modulus and Poisson ratio inferred from seismic tomography investigation.

Method

The definition of a FEM problem require to set up boundary conditions, optimal size of domain, meshing, and the type of the elements that are not known a priori. Therefore, a robust preliminary set-up is needed to obtain realistic results. In order to validate the FEM model, explicitly the size of domain and the mesh resolution, we performed several computations and compared the numerical deformation fields with the analytical ones (Okada, 1992). We considered a 3D FEM model reproducing a rectangular dislocation in a homogeneous and isotropic half-space. The geometry of the intrusion source is reported in table I. We assumed zero-stress values at the upper surface and zero displacement values at bottom and lateral boundaries. The dislocation source was modeled as a rectangular discontinuity surface by means of “pair elements” (COMSOL 2004): we imposed a non null homogeneous dislocation over the source area and a condition of identity pair along the remaining fault surface. The identity pairs enforce continuity in the deformation fields over the fault discontinuity.

Material behaviour was assumed elastic with $\lambda = \mu$, namely Poisson ratio $\nu = 0.25$, and Young modulus of 30GPa. A domain of $50000 \times 50000 \times 35000 \quad m^3$, meshed with tetrahedral elements, proved sufficient to well represent the problem under examination.

In order to compare the finite element and the analytical results a mean misfit function is defined as:

$$\Delta(U) = (\sum_{i=1}^{N} U_i^{FE} - U_i^{AN}) / N \qquad (1)$$

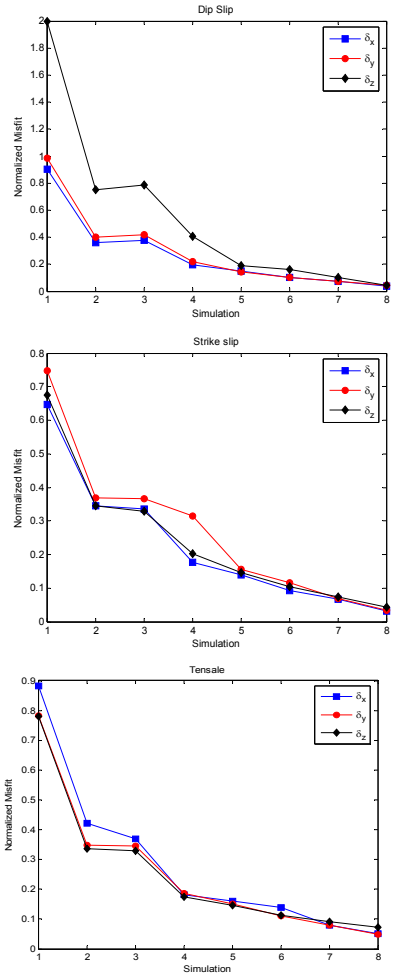

Fig. 1 - Misfit values between numerical and analytical solutions for all the displacement components. Dip-slip (a), strike-slip (b) and tensile (c) dislocation sources are considered.

where U_i^{FE} is the computed deformation at the node i for the numerical model, U_i^{AN} is the corresponding results for the analytical model, and N is the node number. To provide a reference for the quality of the fit, we have normalized each mean misfit value by the average magnitude of the deformation field:

$$M(U) = (\sum_{i=1}^{N} U_i^{AN}) \qquad (2)$$

In a finite element analysis a critical step is the meshing of the computational domain. As seen from Fig. 1 and table II, the number of element of the mesh largely influences the accuracy of the solution. There are several ways to compute the quality of individual elements and how to quantify the overall quality of a mesh. In the presented work we evaluate the element quality with respect to the equilateral simplex. For a tetrahedral element, the quality is expressed as:

$$q = f \frac{V^2}{(A+B+C+D)^3}, \qquad (3)$$

where V denotes the volume of the tetrahedron, A, B, C, and D are the areas of its faces and $f = 216\sqrt{3}$ is a normalizing coefficient ensuring that the quality of an equilateral tetrahedron is equal to 1. Alternative relations for the evaluation of the element quality are usually based on the ratio of volumes of spheres inscribed and circumscribed to a tetrahedron. In all the computations the minimum mesh quality is warranted to be higher than 0.2. Using a refined mesh, the ratio $\Delta(U)/M(U)$ is less than 0.05 for all the displacements components. Therefore the numerical results are found to be in nearly perfect agreement with the analytical solution.

Length: L [m]	Width: W [m]	Inclination angle: δ [degree]
1000	1000	90°

Strike angle: ϑ[degree]	Depth of top: d [m]	Dislocation: l [m]
0°	1000	1

Table I. Dislocation source parameters.

Computation	***# 1***	***# 2***	***# 3***	***# 4***	***# 5***	***# 6***	***# 7***	***# 8***
Mesh vertices	2228	2513	2570	3195	3977	5101	8591	36196
Vertex elements	32	32	32	32	32	32	32	32
Edge elements	206	229	230	280	307	350	408	612
Boundary elements	2166	2434	2482	3004	3586	4226	6160	15620
Elements (Tetrahedral)	9858	11236	11505	14663	18888	25141	45021	205700
Minimum element quality	0.3544	0.3083	0.3441	0.3109	0.3417	0.2960	0.3050	0.2454

Table II. Mesh statistic.

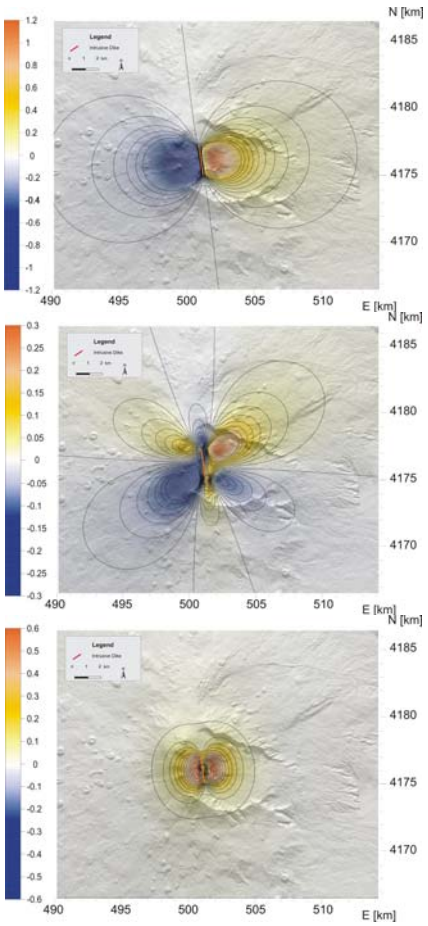

Fig. 2 - Theoretical deformation field of the Okada model for a tensile dislocation in a homogeneous, isotropic and elastic medium.

2001 Etna Eruption

The modelling procedure is applied to study the ground deformation observed during the emplacement and final uprising of the dike of the Etna 2001 eruption. The GPS data inversion indicated the response to a tensile mechanism with an opening dislocation of ca. 3.5 m that evidenced an intrusion in the volcano edifice along a ca. N-S direction (Bonaccorso et al., 2002). In the numerical computations we used the source geometry obtained by the analytical inversion model from Bonaccorso et al. (2002). In the following sections we will evaluate how the topography and medium heterogeneity can affect the computed ground deformation. We evaluate four numerical models in which we considered: (i) an homogeneous elastic medium with a flat surface, (ii) an homogeneous elastic medium with the real topography of Mt Etna, and (iii) an elastic heterogeneous medium with the real topography.

Flat Topography and Homogeneous Medium

A 3D FEM model was performed considering a rectangular tensile dislocation embedded in a homogeneous, isotropic and elastic half-space. The geometry of the intrusion is reported in table III. The medium is assumed to be elastic and poissonian ( ) with a Young modulus of 30 GPa. In Fig. 2 is shown the theoretical deformation field of the Okada model. We verified that all the deformation components well matches the analytical ones within the computational error. This allowed us to verify the validity of the domain size, mesh resolution and boundary conditions used in these computations.

Tensile dislocation: $\vec{B}$ [m]	Length: L [m]	Width: W [m]
3.5	2200	2300

Depth of top: d [m]	Inclination angle: δ [degree]	Strike angle: ϑ[degree]
1500 asl	90°	7°

Table III. Parameters of the intrusive dike forerunning the 2001 eruption (Bonaccorso et al., 2002).

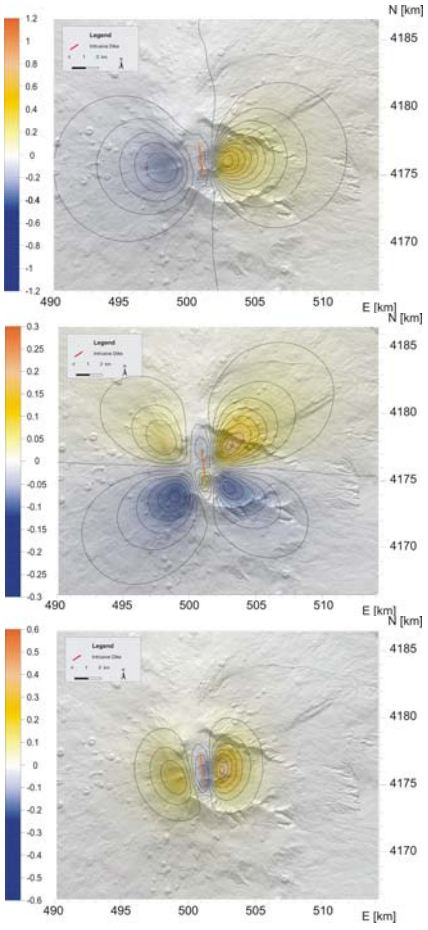

Fig. 3 - Deformation components of the 2001 dike intrusion in a homogeneous, isotropic and elastic medium with real topography.

Real Topography and Homogeneous Medium

The 3D numerical model includes now the real topography of Etna volcano as ground surface using the 90 m Shuttle Radar Topography Mission (SRTM) data. Results highlighted the influence of topography on the deformation fields. Comparing the numerical results (Fig. 3) with the analytical ones (Fig. 4) we notice a loss of symmetry of the deformation pattern due to the non-symmetry of the domain. A decrease in the deformation components near the summit craters is observed because the effective distance between the source and the ground surface is increased.

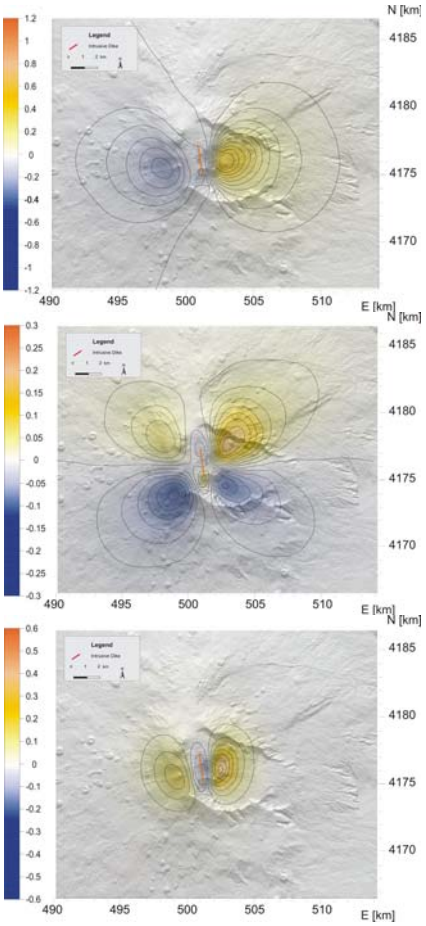

Figure 4. Deformation fields of the tensile crack in a heterogeneous medium with topography.

Real Topography and Heterogeneous Medium

We improved the previous model adding a complex distribution of the elastic medium properties. At each node of the mesh a different values of Young modulus and Poisson ratio is assigned. We used seismic tomographic information to derive the medium parameters. In particular, the Young modulus was estimated by using the following equation (Kearey and Brooks, 1991):

$$E = 5/6\rho V_p^2, \qquad (4)$$

where V_p is the seismic P-wave propagation velocity and ρ the density of the medium which was fixed to 2500 kg/m3. Instead, the values of Poisson ratio were obtained using the equation (Kearey and Brooks, 1991):

$$\nu = [(V_p/V_s)^2 - 2]/[2(V_p/V_s)^2 - 2], \qquad (5)$$

where V_s is the seismic shear wave propagation velocity. On the basis of Eqs. 4 and 5, the Young modulus varies from 11.5 GPa to 133 GPa, while the Poisson ratio is in the 0.12-0.32 range. Results compared to homogeneous medium model do not reveal significant differences in pattern and intensity of the deformation field (Fig. 4).

In Fig. 5 is reported the observed and the calculated deformation pattern. The recorded vectors are obtained from the interval comparisons 11-16 July before the eruption onset, the modelled ones are obtained from FEM analysis considering the real topography and the heterogeneity of the volcano.

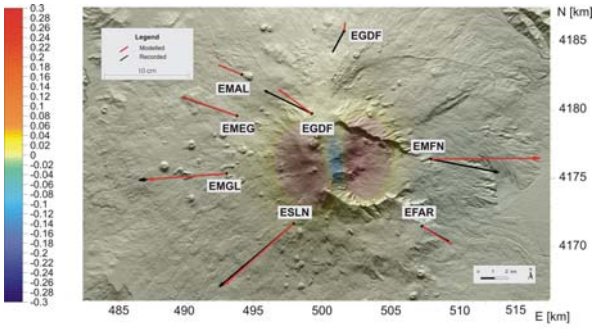

Fig. 5 - Recorded and expected deformation pattern (displacements plus tilt).

Conclusion

A 3D FEM analysis was performed with the aim to describe in a more realistic way the ground deformation due to fault movements. Dip-slip, strike-slip and tensile dislocations sources have been considered and their numerical solutions were compared to analytical solutions from dislocation theory. The meshing procedure was found to be a very tricky step. However, the refined mesh, which gives a good compromise between the computational cost and the solution accuracy, is not so computational heavy to run. The tensile dislocation source is a good approximation to also model intrusive events that frequently occur at Mt Etna. The FEM technique enabled us to consider both the topography and

the medium heterogeneity. The topography significantly alters the expected ground deformation especially near the volcano summit. On the contrary, the medium heterogeneity does not strongly affect the deformation pattern. Several computations were performed to better understand the role played by the assumption on elastic medium parameters. We considered a medium with: (a) an homogeneous Young modulus and heterogeneous Poisson ratio, (b) an heterogeneous Young modulus and homogeneous Poisson ratio, and (c) an heterogeneous Young modulus and heterogeneous Poisson ratio. In the case where only the Poisson ratio is heterogeneous, the discrepancy with respect to the homogeneous model is negligible. The models with heterogeneous Young modulus are those that engender higher perturbations in the numerical models considering the heterogeneity of medium properties. This can be related to the assignment of a fixed tensile dislocation over the dike area. In a homogeneous medium the dislocation source provide a solution that identically coincides with an equivalent pressure source. This cannot be true in a heterogeneous medium. Futures analyses will be carried out to investigate the effect of medium heterogeneity in presence of pressure source.

References

Bonaccorso, A., Aloisi, M. and Mattia, M., 2002. Dike emplacement forerunning the Etna July 2001 eruption modelled through continuous tilt and GPS data, Geophys. Res. Lett..

Bonaccorso, A., Cianetti, S., Giunchi, C., Transatti, E., Bonafede, M.and Boschi E., 2000. Analytical and 3D numerical modeling of Mt. Etna (Italy)volcano inflation, Geophys. J. Int., 142, 000-000.

Bonaccorso, A., and P. M. Davis (2004), Modeling of ground deformation associated with recent lateral eruptions: Mechanics of magma ascent and intermediate storage at Mt. Etna, in Mount Etna Volcano Laboratory, vol. 143, edited by A. Bonaccorso, S. Calvari, M. Coltelli, C. D. Negro, and S. Falsaperla, p. 384, American Geophysical Union Monography Series.

Bonforte, A., Guglielmino, F., Palano, M. and Puglisi, G., 2004. A syn-eruptive ground deformation episode measured by GPS, during the 2001 eruption on the upper southern flank of Mt Etna, Bull Volcanol, 66, 336-341.

COMSOL 2004. FEMLAB, COMSOL AB.

Kearey, P. and Brooks, M., 1991. An introduction to geophysical exploration, Blackwell Scientific Publications.

Occhipinti, R., Elia, M., Bonaccorso, A. and La Rosa, G., 2004. Finite element analysis of ground deformation due to dike intrusion with applications at Mt. Etna volcano, Ann. Geophys., 47, 5.

Williams, C. A. and Wadge, G., 2000. An accurate and efficient method for including the effects of topography in three-dimensional elastic models of ground deformation with applications to radar interferometry, J. Geophys. Res., 105, 103-8120.

THERMAL-MECHANICAL COUPLING FOR MODELING GROUND DEFORMATION IN A VISCOELASTIC MEDIUM

*Danila Scandura * and Gilda Currenti*

Isitituo Nazionale di Geofisica e Vulcanologia, Sezione di Catania
** Email: scandura@ct.ingv.it*

Abstract

Time dependent ground deformation due to pressure sources embedded in a viscoelastic medium are evaluated using Finite Element Method. The presence of viscoelastic material that is likely to characterize the upper crust near magmatic sources, greatly affects the deformation field. Assuming a Generalized Maxwell rheology, we find out that the viscoelastic response of the computed uplift grows in time because of the crust relaxation process. The temporal evolution of ground deformation is basically dependent on the rheology assumption that cannot discount the thermal regime of the crust, especially in volcanic region. In order to evaluate the temperature dependency of the viscoelastic solution we carry out a coupled thermo-mechanical numerical model.

Key words: ground deformation, Finite Element Method, thermal regime.

Introduction

Most volcano deformation models published to date assume that the earth's crust behaves as a perfectly elastic solid. While elastic half space models fit a variety of crustal deformation data, this rheology in case of volcanic regions is an oversimplification. The elastic approximation is generally appropriate for small deformations of crustal materials with temperatures cooler than the brittle-ductile transition, about 300± 500°C depending mainly on composition and strain rate. Thus, elastic behaviour characterizes the upper 10±15 km of the earth's crust in most non-volcanic regions. However, in active volcanic zones, magma at relatively shallow crustal levels can perturb the geothermal gradient significantly. Viscoelastic behaviour is more likely to characterize the upper crust near a magmatic centre, and can greatly influence the surface deformation field, rendering the elastic approximation inappropriate. Material surrounding a long-lived magmatic source be heated significantly above the brittle-ductile transition. Above this temperature, rocks no longer behave in a purely elastic manner, but permanently deform because the fluid strength, or viscosity, is significantly lower. In such a material an imposed stress will cause both an instantaneous, recoverable strain, and time-dependent, permanent strain, whose rate is controlled by its characteristic time, $\lambda_m \approx \frac{\eta}{\mu}$, where η is the viscosity and μ is the rigidity modulus.

In the present study, we investigated the effects of a pressurized spherical magma chamber in a volcanic edifice and the temporal complexities of the deformation due to the viscoelastic medium properties. Firstly, an homogeneous viscoelastic (VE) half-space model was assumed with a Maxwell generalized rheology. The homogeneity assumption is a simplification that was overcome with the introduction of a viscoelastic spherical shell surrounding the magmatic source and an elastic medium outside it. However, the thickness of the spherical shell depends on the magma temperature and the thermal properties of the surrounding rocks. In order to account for the temperature effect, we developed a thermal model which provides the temperature profile around the magma source. We also investigated empirical relationship to infer the temperature-viscosity dependence.

Deformation Model

Axial symmetric model

As first step, we derived the analytical solutions of displacement field in a viscoelastic half-space and compared them to the numerical solutions obtained by Finite Element Method (FEM). Numerical computations are carried out using the FE software FEMLAB. Our approach assumes radial symmetry about the source centre, and can be explored with a two dimensional axisymmetric model (Fig. 1). To approximate an half-space, the axisymmetric FEM is composed of ~223000 triangular elements covering a region that extends 25km horizontally from the source centre and 35km below the surface. The source is located at 4 km depth, and the radius of the spherical magma chamber is 0.7 km (Fig.1). We assumed free

displacement values at the upper surface and zero displacement values at bottom and lateral boundaries. A step-like increase in pressure (ΔP=100 MPa) is applied at time t=0 on the source wall. A generalized Maxwell rheology was assumed, whose physical interpretation is shown in Fig. 2. The instantaneous shear modulus is G_0, the rigidities are μ_0 and μ_1, the long term shear modulus is $\mu_0 G_0$, the viscosity is η, and the bulk modulus is K. For a linear viscoelastic material, the solution can be obtained from the elastic one employing the correspondence principle (Fung, 1965; Christensen 1971). One must replace the constants K and μ appearing in the elastic solution (Bonafede et al. 1986) by their expression as functions of the Laplace variable s, $\tilde{K}(s)$ and $\tilde{\mu}(s)$, which depend on the particular rheology considered. The resulting expression is the Laplace transform of the viscoelastic solution. One must then invert it in order to obtain the solution in the time domain. Since most rocks flow to relax only shear stress, we shall replace only μ with $\tilde{\mu}(s)$, while K is left constant as in the elastic case. The Laplace transform of the viscosity which hold for the generalized Maxwell model is given by (Fung, 1965):

$$\mu(s) = \frac{s(\mu_0 + \mu_1)G_0 + \mu_0\mu_1 G_0^2/\eta}{s + \mu_1 G_0/\eta} \qquad (1)$$

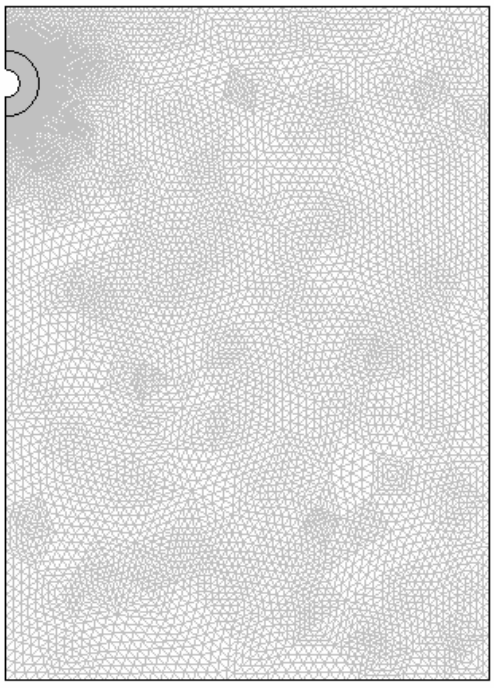

Fig. 1 - The FEM mesh for the axisymmetric model incorporating the spherical magma chamber.

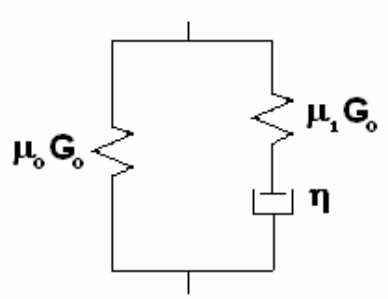

Fig. 2 - Generalized Maxwell model.

Material behaviour was assumed viscoelastic (generalized Maxwell rheology) with Poisson ratio $\nu = 0.25$, rigidity moduli μ_1=μ_2=30GPa and the time constant $\lambda_m = 6.6 \cdot 10^5$ s.

As we observe in Fig. 3, the deformation field practically coincides with the analytical ones. This allowed us to verify the validity of the numeric technique used in these computations.

Viscoelastic shell model

The model was then improved with the introduction of a viscoelastic spherical shell (radius 1.7 km) surrounding the magmatic source. It was supposed a viscoelastic behaviour inside the shell, an elastic behaviour outside it. It is logical to assume that rocks near the inflation source are considerably heated and weakened beyond the brittle-ductile transition temperature where VE rheology is more appropriate. As we can notice from Fig. 4, after the introduction of the viscoelastic shell the surface uplift is less enhanced than in the previous model when all the half-space medium is assumed viscoelastic.

Thermal model

The viscoelastic properties of the shell depend on the size of the chamber and on the temperatures of the magma and of the surrounding rocks. A variety of empirical relationship can be used to infer the temperature-viscosity dependence. If we assume a magma chamber maintained at a constant temperature, the temperature distribution around the magmatic source can be computed by solving a heat conduction equation.

Since the deformation timescales are much shorter than those over which the magma chamber evolution takes place, the temperature distribution, and therefore the viscosity profile inside the shell, can be considered as steady. Therefore, we can conduct the coupled model in two steps solving separately: (i) the heat conduction equation to compute the temperature profile and (ii) the viscoelastic problem to obtain the numerical solution of the deformation field.

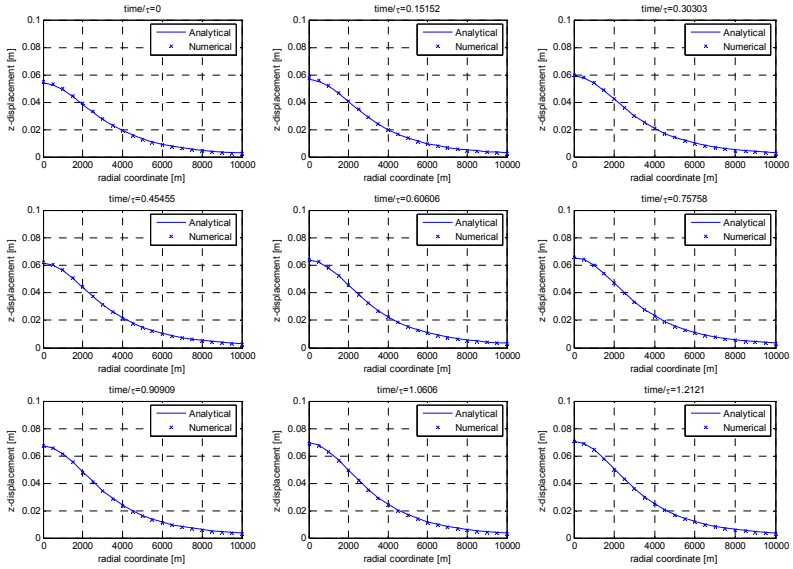

Fig. 3 - Comparison of ground uplift due to a pressure source and the corresponding results for the analytical model for a homogenous, isotropic, regular and viscoelastic domain. The radius of the source, located at a depth of $4km$, is $0.7km$.

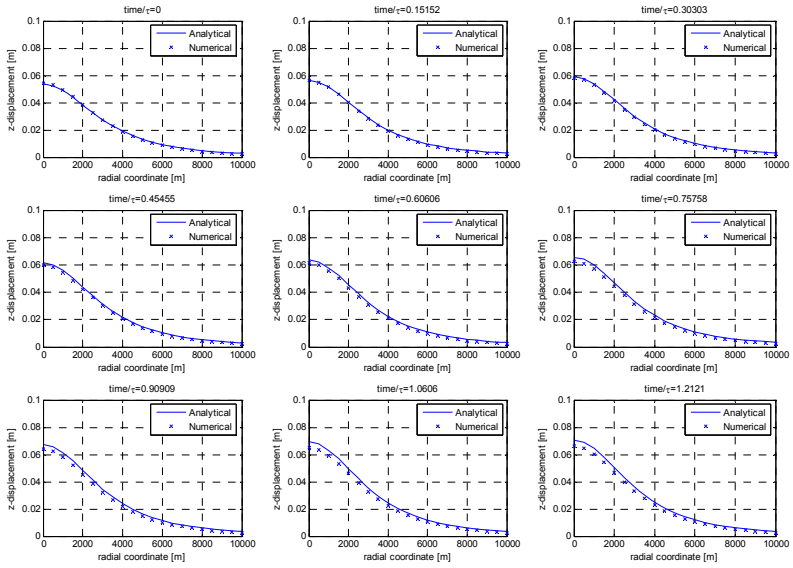

Fig. 4 - Comparison of ground uplift due to a pressure source and the corresponding results for the analytical model for a homogenous, isotropic, regular and elastic domain with a spherical viscoelastic shell surrounding the magmatic source. The radius of the source, located at a depth of 4 km, is 0.7 km, the radius of the shell is 1 km.

To derive the temperature profile, we numerically solved the equations for heat conduction in a axial symmetric formulation. The equation are solved in a cylindrical coordinate system. The time-dependent, heat conduction equation with internal heat sources used in this study is given by:

$$\rho C_p \frac{\partial T}{\partial t} - \nabla(k \nabla T) = q \qquad (2)$$

where $T = T(r,z,t)$ is the temperature field, r is the radial coordinate, z is the vertical coordinate, ρ is the crustal density, C_p is specific heat capacity, t is time, κ is thermal conductivity, q is the volumetric heat source. In the following simulations the value of the volumetric heat source was set to zero and the temperature along the shell was set to $T_0 = 1000°K$. Clearly, this boundary condition

represents the equation we used to simulate a continuous refilling of the magma chamber. As thermal initial condition, we used the steady-state geotherm given by (Hinojosa et al., 2000):

$$T(z) = T_s + \left(\frac{q_m z}{k}\right) + \left(\frac{A_s b^2}{k}\right)\left(1 - e^{-z/b}\right) \; for \; 0 \le z \le L \quad (3)$$

where T_s is the surface temperature, q_m is the heat flow coming from the mantle, A_s is the volumetric rate of heat production, and b is a characteristic depth of the order of 10±5 km. As boundary condition, we assumed a thermal insulation condition at the upper surface. At bottom and lateral boundaries we can assign the geothermal temperature values since they are far enough to not be affected by the magmatic source. The steady state temperature profile is shown in Fig. 5.

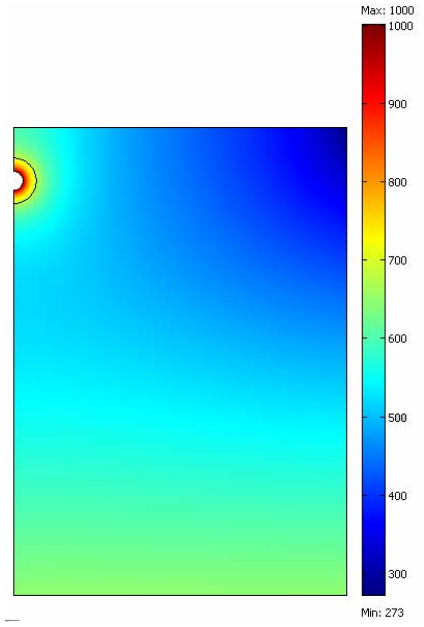

Fig. 5: Steady state temperature profile.

Starting from the temperature distribution, we estimate the medium viscosity surrounding the source region using Griggs (1939) equation (S. Maaløe, 2001):

$$\eta = \frac{\sigma}{3\dot{\varepsilon}} \quad (4)$$

where σ is the stress and $\dot{\varepsilon}$ the strain rate. The strain rate is estimated from the experimental data of Hirth and Kohlstedt (1995) for an isostatically compressed olivine matrix containing 2% melt:

$$\dot{\varepsilon} = A\sigma^n d^p \exp\left(\frac{-Q}{RT}\right) \quad (5)$$

where A is a materials constant for 1–3% melt, σ is the deviatory stress in bars, d is the grain diameter in cm, Q is the activation energy, R is the Boltzmann constant, T the temperature in °K. Additional work is needed to define plausible values for the rheological parameters, and determine the extent to which these parameters vary in the region of high thermal gradients near the magma chamber. The values of the parameters used in the computations are summarized in table I. We then run the deformation model as in the previous case and the time evolution of ground uplift at r=0 is shown in Fig. 6.

Thermal parameters		
ρ	Crustal density	2400 kg m^{-3}
C_p	Specific heat capacity	1000 J kg $°K^{-1}$
q	Volumetric heat source	0 W m^{-3}
T_s	Surface temperature	273°K
q_m	Heat flow	0.03 m Wm^{-2}
k	Thermal conductivity	4 Wm^{-1} K^{-1}
A_s	Volumetric rate of heat production	2.47 μ Wm^{-3}
b	Length scale for crustal radioactive decay	14.170 km

Mechanical parameters		
A	Material constant	1.2 x 10^{-6}
n	Diffusion creep parameter	1
d	Grain diameter	0.1 cm
p	Diffusion creep parameter	-2
Q	Activation energy	137 kJ/(g x mol x °K)
R	Boltzmann constant	8.314 J / (g x mol x °K)

Table IV. Thermal and mechanical parameters.

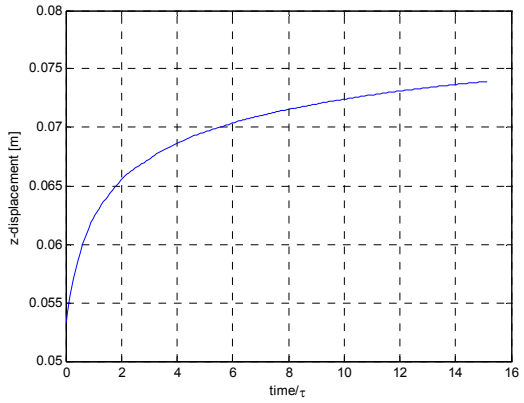

Figura 6: Ground uplift as function of time. The simulation were computed using parameters shown in table I.

Trapezoidal source function

In order to get a more realistic results, we used a pressure source which evolve like a trapezoidal source history instead of a step-like source function. The source history increases linearly in time from 0 to ΔP for t ranging between 0 and t_1, remains constant for $t_1 \le t \le t_2$, and finally decrease to 0 for $t_2 \le t \le t_3$:

$$g(t) = \Delta P\left\{\frac{t}{t_t}\left[1-H(t-t_1)\right]+H(t-t_1)-H(t-t_2)+\frac{t_3-t}{t_3-t_2}\left[H(t-t_2)-H(t-t_3)\right]\right\} \quad (6)$$

where H(t) is the Heaviside function. As first step, we focussed on the analysis of a homogenous, isotropic and regular domain, in order to compare the results using a FEM technique with the analytical ones. Figure 7 shows the ground uplift as a function of time obtained from the analytical and numerical solutions, the deformation field is close with the analytical ones.

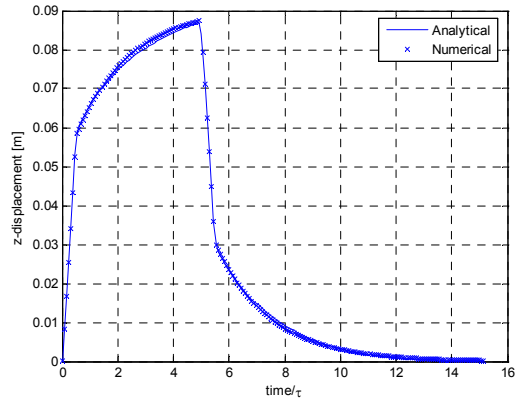

Figura 7: Comparison of ground uplift as a function of time and the corresponding results for the analytical model. Trapezoidal source history is employed with t_1=τ/2, t_2=5τ and t_3=5.5τ, the applied pressures is 100 MPa.

Computations were then carried out considering the model which includes the spherical shell whose viscosity is temperature dependent. A more careful analysis is necessary in order to choose properly the values of the parameters t_1, t_2 and t_3.

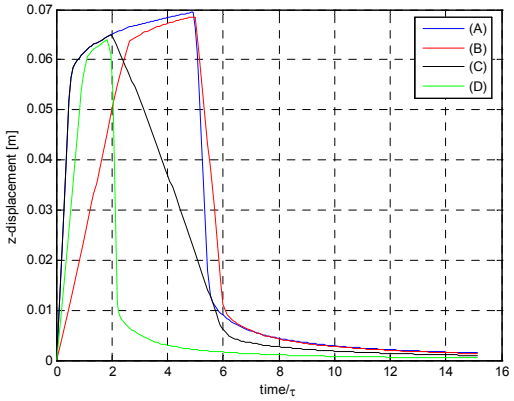

Figura 8: Ground uplift as a function of time obtained from viscoelastic pressure source model. Trapezoidal source histories are employed with t_1=τ/2, t_2=5τ and t_3=5.5τ (curve A); t_1=2.5τ, t_2=5τ and t_3=6τ (curve B); t_1=τ/2, t_2=2τ and t_3=6τ (curve C); t_1=τ, t_2=2τ and t_3=2.2τ (curve D). The applied pressures is 100 MPa.

Fig. 8 shows for curve representing the ground uplift as a function of time obtained with different choices of the time values which characterize the source history. Curve (A) is obtained with t_1=τ/2, t_2=5τ and t_3=5.5τ; curve (B) has t_1=2.5τ, t_2=5τ and t_3=6τ, curve (C) has t_1=τ/2, t_2=2τ and t_3=6τ, curve (D) has t_1=τ, t_2=2τ and t_3=2.2τ. We can observe that the peak representing the maximum uplift is sharper if t_3 is close t_2 and the deflation is more pronounced, as in curve (A) and (D). Curve (B) also exhibit a very slow initial gradient, due to the fact that the pressure applied at the source increase with t_1=2.5τ. Among the four cases, the smallest uplift is given by curve (D) which has the lowest value of t_2: the vertical displacement does not have the time to grow as in the other cases, since the pressure begins to decrease after only 2τ. Curve (A) exhibits the highest maximum uplift, since the time t_2, during which the applied pressure increases or remains constant, is the longest, 5τ. Curve (B) and (A) have the same t_2, but the pressure increase is slower for curve (B), since t_1=2.5τ, thus allowing a smaller uplift.

Conclusions

Finite element models have been carried out to investigate the temporal evolution of

viscoelastic deformation caused by pressure changes within a magmatic source. The presence of viscoelastic material that is likely to characterize the upper crust around magmatic sources, greatly alters the deformation field. We find out that the ground uplift grows in time and its temporal evolution is mainly dependent on the average rigidity and viscoelasticity of the medium surrounding the source. In fact, a change in the vertical uplift of about 2 cm is observed over time, when a viscoelastic shell around the spherical source was introduced in the model. The definition of elastic\anelastic rock properties strongly affect the solution and, especially in volcanic region, cannot discount the thermal regime of the crust. The coupled thermo-mechanical model evidences that the thermal state of the crust can play an important role in the temporal evolution of deformation field, since it influences the relaxation time of the medium.

Our findings highlighted that the interpretation of long-term deformation has to take into account the anelastic behaviour of the crust in order to obtain a reliable estimate of the pressure changes exerted by the magmatic source. The proposed axial symmetric models can be easily extended to a fully 3D representation in which topography, medium heterogeneity and complex source geometry can be included. To this regard, the medium parameter involved in the coupled thermo-mechanical model can be better constrained using temperature data and seismic attenuation tomography study which can provide a more realistic image of the mechanical rock properties and the thermal state of the volcano.

References

Bonafede, M., Dragoni, M. and Quareni, F., 1986. Displacement and stress fields produced by a centre of dilatation and by a pressare source in a viscoelastic half-space:application to the study of round deformation and seismic activity at Campi Flegrei, Italy, Geophys. J. R. astr. Soc., 87, 455-485.

Büttner, R., Zimanowski B., Blumm J. And Hagemann, L., 1998. Thermal conductivity of a volcanic rock material (olivine- melilitite) in the temperature range between 288 and 1470 K, J. Volcanol. Geotherm. Res., 80, 293-302.

Christensen, R. M., 1971. Theory of Viscoelasticity: an Introduction, Academic Press, New York.

Dragoni, M. and Magnanensi, C., 1989. Displacement and stress produced by a pressurized, spherical magma chamber, surrounded by a viscoelastic shell, Physics of the Earth and Planetary Interiors, 56, 316-328.

Fernández, J., Tiampo, K. F. and Rundle, J. B., 2001. Viscoelastic displacement and gravity changes due to point magmatic intrusions in a gravitational layerd solid earth, Geophys. J. Int., 146, 155-170.

Folch, A., Fernandez, J., Rundle, J. B. And Martì, J., 1999. Ground deformation in a viscoelastic medium composed of a layer overlying a half-space: a comparison between point and extended sources, Geophys. J. Int., 140, 37-50.

Fung, Y.C., 1965. Foundations of solid Mechanics, Prentice-Hall, Englewood Cliffs.

Griggs, J., 1939. The creep of rocks, J Geol, 47, 225-251.

Hinojosa, J. H. and Mickus, K. L., 2002. Thermoelastic modeling of lithospheric uplift: a finite –difference numerical solution, Computer & Geosciences, 28, 155-167.

Hirth, G. and Kohlstedt, D., 1995. Experimental constraints on the dynamics of the partially molten upper mantle: Deformation in the diffusion creep regime, J. Geophys. Res., 100, 1981-2001.

Ivins, E. R., 1996. Transient creep of a composite lower crust. A polymineralic basis for rapidly evolving postseismic deformation modes, J. Geophys. Res., 101, 28,005-28,028.

Jackson, I., Fitz Gerald, J. D., Faul, U. H. and Tan, B. H., 2002. Grain-size-sensitive seismic wave attenuation in polycrystalline olivine, J. Geophys. Res., 107, 1029/2001JB001225.

Jackson, I., Fitz Gerald, J. D., Faul, U. H. and Tan, B. H., 2004. Shear wave attenuation and dispersion in melt-bearing olivine polycrystals: Specimen fabrication and mechanical testing, J. Geophys. Res., 109, 1029/2003JB002406.

Maaløe, S., 2002. Physical behaviour of the plume source during intermittent eruptions of Hawaiian basalts, Contrib Mineral Petrol, 142, 653-665.

Newman, A. V., Dixon T. H., Ofoegbu, G. I. And Dixon, J. E., 2000. Geodetic and seismic constraints on recent activity at Long Valley Caldera, California: evidence for viscoelastic rheology, , J. Volcanol. Geotherm. Res., 105, 183-206.

Newman, A. V., Dixon T. H. and Gourmelen, N., 2004. A four-dimensional viscoelastic deformation model for Long Valley Caldera, California, between 1995 and 2000, J. Volcanol. Geotherm. Res., 150, 244-269.

Parson, T, 2002. Post-1906 stress recovery of the San Andreas fault system calculated from three-dimensional finite element analysis, J. Geophys. Res., 107, 1029/2001JB001051.

Warren, J. M. and Hirth, G., 2006. Grain size deformation mechanisms in naturally deformed peridotites, Earth and Planetary Science Letters, xx, xxx-xxx.

ADVANCES IN MODELLING METHODS FOR LAVA FLOW SIMULATIONS

Ciro Del Negro and Annamaria Vicari*

Isitituo Nazionale di Geofisica e Vulcanologia, Sezione di Catania
**Email: delnegro@ct.ingv.it*

Abstract

The latest eruptions of Mt Etna, occurring in 2004 and 2006, represented a further step towards defining the real potential of the MAGFLOW model as an effective tool for real-time forecasting of lava flow hazards. We will briefly summarize results obtained by comparing the simulated and the real events. The reliability of parameters derived from the analysis and interpretation of field data, such as those of use for the estimation of the flow rate, has allowed verifying the effective capability and high performance of the modeling implemented in MAGFLOW. It was also demonstrated that in order to simulate realistic scenarios, data collected on site during the evolution of the eruption are necessary.

Keywords: MAGFLOW model, effusion rate, satellite data, hazard map

Introduction

The study of the lava flow requires the development, validation and application of accurate and robust physico-mathematical models able to forecast their spatial and temporal evolution. Simulations of lava flow emplacement attempt to understand how the complex interaction between flow dynamics and lava physical properties lead to the final flow dimensions and morphology observed in the field. The advance of lava flows produced by volcanic eruptions has been studied through field observations as well as through analytical and numerical modeling.

Firstly, we aimed at optimizing the new model based on Cellular Automata (CA), called MAGFLOW, for simulating lava flow paths and the temporal evolution of lava emplacement (Fig. 1). We introduced an algorithm based on Monte Carlo approach to solve the anisotropic problem. A steady state solution of Navier Stokes equation, in the case of non-isothermal laminar pressure-driven Binghamian fluid, has been taken into account as evolution function of CA. In the same way, it is possible to do some considerations about the cooling mechanism. Heat of lava flow is carried out in accordance with the flow motion. Temperature of the lava in a cell is considered as uniform. For the cooling mechanism, we consider the radiative heat loss only from the surface of the flow (the effect of conduction to the ground and convection to the atmosphere is neglected), and the change of the temperature due to mixture of lavas between cells with different temperatures. Lava flows occurred at Etna during 2001 and 2004-2005 eruptions were simulated to validate the MAGFLOW model.

Secondly, we implemented some algorithms based on satellite thermal data to estimate effusion rate of lava flows useful for driving MAGFLOW numerical simulation. The same algorithms were used to estimate the total flow volume of 2004 Etna eruption. Moreover, MAGFLOW was employed for the compilation of hazard maps related to lava invasion at Mt Etna.

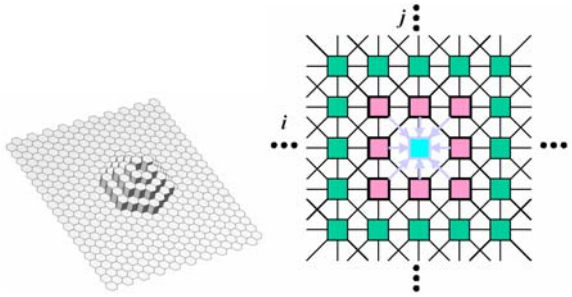

Fig. 1 – Cellular structure of the MAGFLOW model.

Lava flow simulations of 2001 Etna eruption

The 2001 eruption at Mt. Etna provided the opportunity to verify the ability of our model to simulate the path of lava flows. In initial simulations, we considered only the Monte Calcarazzi vent (2100 m a.s.l.), opened on 18 July 2001 (Fig. 2). A Digital Elevation Models (DEM) with mesh size of 10x10 m was used for the simulation. For the whole period of the simulations we considered a variable flow rate. Simulations were carried out using a relationship between magma viscosity and temperature by Giordano and Dingwell (2003). This viscosity

model allowed to better follow the evolution in space and time of lava flow paths. The observed and the simulate lava flow fields, corresponding to the same time of simulations, shown a good agreement. The difference between the simulated and real lava flows distribution in the final configuration depends on the presence, in the last days of the eruption, of lava tubes in the middle portion of flow fields, causing the opening of some ephemeral vents and the creation of a small secondary flow.

Fig. 2 - 2001 Etna eruption.

Application to 2004 Etna eruption

The MAGFLOW model proposed here was applied to reproduce the lava flow occurring during the early phase of the 2004-2005 Etna eruption (Fig. 3). We simulated the effusive activity taking place during the first forty-six days of the eruption, for which some field data for input and comparison are available. The simulations were produced taking into account the active phases of each vent. Based on field observations at vents we assumed daily effusion rates for the lava flow ranging from 2.8 to 4.9 m^3/s for the whole period of the simulation. As a topographic basis, we used the digital elevation model of the Etna maps with a 1:10000 scale (the spatial grid resolution was $\Delta x = \Delta y = 10$ m). In order to check the role of viscosity in lava flow morphology, the simulations were computed with the three different relationships. The comparison between the three simulations shows the strong dependence of the model on the variation of viscosity law (the other parameters are unchanged in the three different simulations). As expected, viscosity plays a significant role in flow morphology: it appreciably affects length, width, area, and thickness.

Fig. 3 - 2004 Etna eruption.

Volume estimation of 2004 Etna eruption by topographic approach and satellite data

The 2004 Etna eruption was characterized by outpouring of degassed lava from two main vents and a number of ephemeral vents within Valle del Bove. Field surveys of lava flow thickness allowed to constrain lava volumes between 18.5 and 32 $*10^6$ m^3, with an associated eruption rate between 2.3 and 4.1 m^3/s (updated after three month of eruption). Estimating eruption volume is a critical component of volcanology.

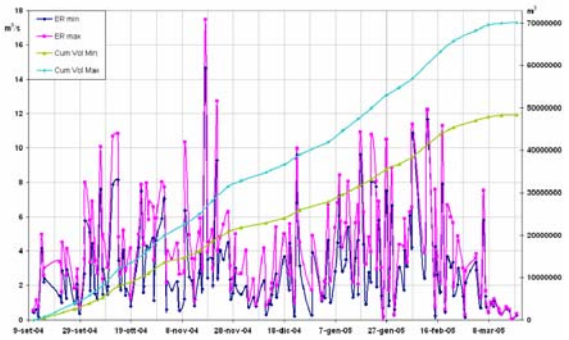

Fig. 4 - Effusion rates estimated during the period September 2004 - March 2005 by satellite data and cumulative volume obtained by integrating the effusion rate over the entire period of the eruption.

We used the method known as “topographic approach” to estimate the volume of a lava flow by subtracting pre and post-eruption DEM. In this way, the uncertainty of the volume computed by this method can be calculated considering the elevation residual out of the boundary of the flow. Two different pre-eruption DEM were available. The first one realized by Maria Marsella (University of Rome) using data collected during an aerophotogrammetric flight in August 2004 with a resolution of 5 meters, in which in a first approximation the conversion from geodetic datum to ellipsoid datum has been realized with a translation of +46 meters. The second one

realized by Maria Teresa Pareschi (INGV-Sezione di Pisa) using the LiDAR system with a resolution of 2 meters and updated on 16 September 2004. As post-eruption DEM we have considered two different DEM, both updated in August 2005, one with a resolution of 10 meters realized also by Maria Marsella using aerophotogrammetric flight and the other with a resolution of 1 meter realized by Maria Teresa Pareschi using the system LiDAR, that presents a vertical and horizontal precision of respectively 1200 m: ±15 cm and at 3000 m: ±35 cm. DEMs were interpolated to the same spatial resolution to permit their comparison. By comparing these DEM, a total volume of 62.728.948 ± 3.149.153 m^3 was estimated. This volume is about 2-3 times as large as the volume estimated from field based thickness measurement [INGV staff, 2005]. The topographic approach is advantageous because it is possible to obtain highly accurate lava volume estimate, but the method is limited by the availability of topographic data of the surface.

Fig. 5 - The lava flow field in the Valle del Bove on 9 November 2006.

An alternative method to topographic approach is represented from using of satellite data. It is possible to obtain total flow volumes by integrating the effusion rates estimated using satellite thermal data over the entire duration of an eruption. An algorithm to estimate the effusion rate of lava flow starting from thermal satellite data has been implemented in collaboration with Department of Engineering of the Catania University. Our satellite-based data consisted of thermal data from MODIS satellite-borne radiometers (TERRA - AQUA) acquired from 10 September 2004 to 18 March 2005, for a total of 178 cloud-free images. Total flow volume is derived by plotting effusion rate against time and integrating over the duration of the eruption (September 2004 - March 2005) (Fig. 4). Moreover, the effusion rate time series, allow us to define the variation in volume emplacement during the course of the eruption (cumulative volume, Fig. 1). The total volume estimated is confined between 49.000.000 and 70.000.000 m^3, which is in according of volume found by previous approach.

Application to 2006 Etna eruption

The 2006 Etna eruption provided the opportunity to verify our model's ability to predict the path of lava flows while the event was ongoing and to produce different scenarios as eruptive conditions changed. At 23:30 local time on 14 July 2006, a fissure opened on the east flank of the South-East Crater (SEC) summit cone of Mt Etna. Two vents (B1 and B2) along the fissure produced a lava flow spreading east to the Valle del Bove. We simulated step-by-step the whole effusive activity, during the period of 14 July – 29 July 2006, produced from two vents B1 and B2, opened between 3000 m and 3100 m a.s.l. MAGFLOW model can take into account the way in which effusion rate changes during an eruption and how this influences the spread of lava as a function of time.

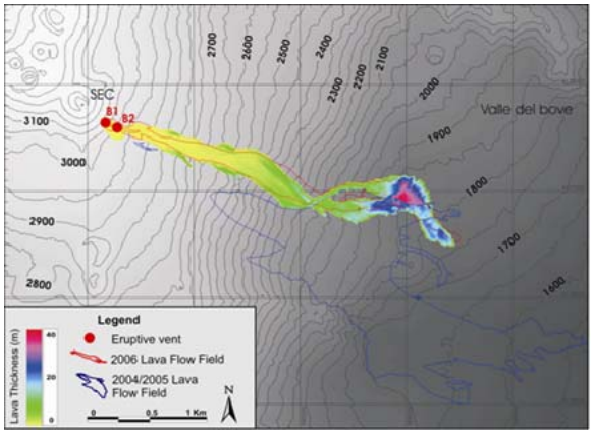

Fig. 6 - Simulated lava thickness of the 2006 Etna eruption. The different colors of the simulation are associated to different thickness. The red contour represents the observed lava flow field at the same time. The blue contour is the 2004/2005 observe lava flow field.

These features are of special interest, particularly as effusion rates can be highly variable. Indeed, lava effusion rates can vary by orders of magnitude over a matter of hours, and are difficult to determine in-situ. However, lava effusion rates can be estimated using thermal infrared satellite imagery obtained from low spatial/high temporal resolution remote sensing data (e.g. MODIS, AVHRR). To this end, we developed, in collaboration with UR15-Fortuna, an automatic system that uses near-real-time infrared satellite data acquired by MODIS and AVHRR sensors to drive numerical simulations of lava flow paths. The result of the simulation is reported in Fig. 6.

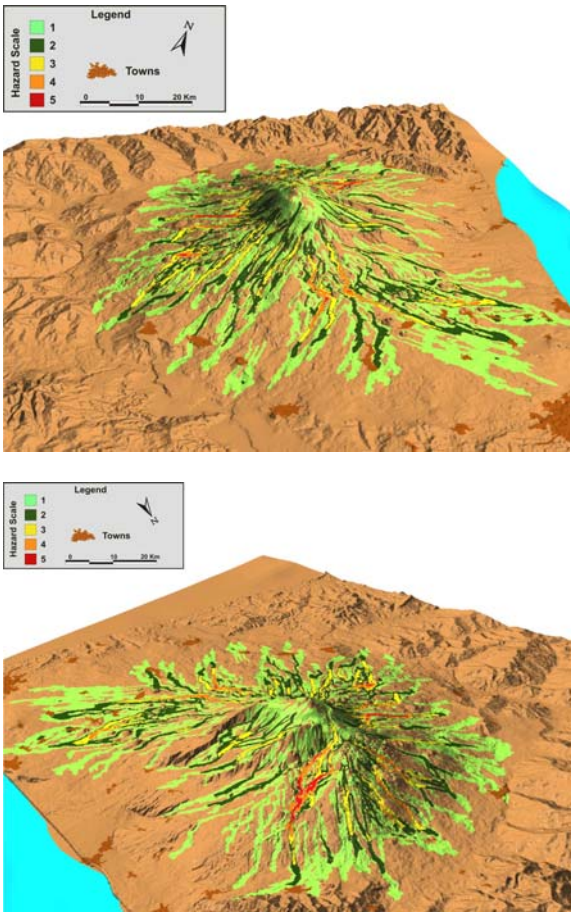

Fig. 7 – Two diverse prospective views of the hazard map realized by MAGFLOW model. The different colors are associated to the diverse probability of lava flow invasion.

Hazard Map

MAGFLOW represents the central part of an extensive methodology for the compilation of hazard maps related to lava invasion at Mt Etna. Hazard map was realized by simulating a number of lava flows from a set of initial data (a record of past eruptions) and with different parameters of the volcanic system in a meaningful range of variation. We assumed a preliminary zonation for identifying possible emission regions with the highest probability of opening. After that, a set of reference values for the parameters of the simulation model based on the knowledge of past eruptions was estimated.

MAGFLOW was used to determine for each emission region the area that can be invaded by lava flows originated from sample points located in that region. Last step was to assign the probability of lava invasions to interested region, calculated on the basis of the simulated lava flows (Fig. 7). Resulting hazard map shows areas that likely would be affected by future volcanic activity and is extremely useful to people living nearby to judge for themselves the relation between potentially dangerous areas and their daily lives. The assessments are also critical for planning (1) long-term land-use; and (2) effective emergency-response measures, especially when a volcano begins to show signs of unrest.

References

Del Negro C., Fortuna, L. and Vicari, A., (2005). Modelling lava flows by Cellular Nonlinear Networks (CNN): preliminary results. Nonlin. Proc. Geophys. 12, 505-513.

Vicari, A., Herault, A., Del Negro, C.; Coltelli, M., Marsella, M., Proietti, C. (2007). Modelling of the 2001 Lava Flow at Etna Volcano by a Cellular Automata Approach, Environmental Modelling & Software, 22, 1465-1471.

Del Negro, C., Fortuna, L., Herault, A., Vicari, A. (2007). Simulations of the 2004 lava flow at Etna volcano by the MAGFLOW Cellular Automata model, Bull. Volcanol., in press.

Herault, A., Vicari, A., Ciraudo, A., and Del Negro, C. (2007). Forecasting Lava Flow Hazard During the 2006 Etna Eruption: Using the Magflow Cellular Automata Model, Computer & Geosciences, in press.

Coltelli, M., Proietti, C., Branca, S., Marsella, M., Andronico, D., Lodato, L., 2005. Lava flow multitemporal mapping: the case of 2001 flank eruption of Etna, submitted to JGR.

NEAR REAL TIME FORECASTING OF 2006 ETNA ERUPTION USING THERMAL SATELLITE DATA

Annamaria Vicari

Isitituo Nazionale di Geofisica e Vulcanologia, Sezione di Catania
** Email: vicari@ct.ingv.it*

Abstract

The lava flow hazard on Etna volcano was evaluated during the ongoing eruptions by means of the MAGFLOW cellular automata model. This model was developed for simulating lava flow paths and the temporal evolution of lava emplacement. MAGFLOW is intended for use in emergency response situations during an eruption to quickly forecast the lava flow path over some time interval from the immediate future to a long-time forecast. Many data are necessary to run MAGFLOW and to determine how far lava will flow. However, for a given composition, the volumetric flux of lava from the vent (i.e. the lava effusion rate) is the principal factor controlling final flow dimensions. As such, simulations that take into account the way in which effusion rate changes during an eruption, and how this influences the spread of lava as a function of time, are of special interest, particularly as effusion rates can be highly variable. To this end, during the latest eruptions of Etna, occurring in July and October 2006, the lava effusion rates were estimated at regular intervals (i.e. up to two times per day) using thermal infrared satellite data (e.g. MODIS, AVHRR). The 2006 Etna eruptions represented a further step towards defining the true potential of the MAGFLOW model as an effective tool for real-time forecasting of lava flow hazards. We will briefly summarize results obtained by comparing the simulated and the real events.

Key words: MAGFLOW model, MODIS, AVHRR.

Introduction

Timely predictions of the areas likely to be inundated by lava flows are of major interest to hazard managers during a volcanic eruption. In order to estimate the amount of damage that can be caused by a lava flow, it is useful to be able to predict the size and extent of such flows. Numerical simulation is a good tool to examine such events. With such simulations, one can explore various eruption scenarios and these can specifically be used to estimate the extent of the inundation area, the time required for the flow to reach a particular point and resulting morphological changes. However, to reproduce the advancement of a lava flow is not easy, because the temperature, rheological properties and effusion rate are not linearly dependent and they are variables on space-time domain. For this reason, most of the models that we can find in literature, are based on various simplifications of the governing physical equations and on analytical and empirical modelling (Young and Wadge, 1990; Costa and Macedonio, 2005) but they are not easy to be applied under general conditions. An alternative to differential equation methods is represented by Cellular Automata (Crisci et al., 1986; Ishihara et al. 1990; Miyamoto and Sasaki, 1997).

We developed the MAGFLOW Cellular Automata model which involves a steady state solution of the Navier-Stokes equations coupled to heat transfer due to radiative losses and solidification effects modeled via a temperature dependent viscosity. MAGFLOW model requires as input data a digital representation of the topography over which the lava is to be emplaced, the location of the eruptive vent, knowledge of the relationships of viscosity and yield strength with temperature, and an estimate of the lava effusion rate. We already applied the MAGFLOW model to reproduce flow fields formed during the 2001 and 2004 eruptions at Mt Etna (Del Negro et al., 2007; Vicari et al., 2007; Herault et al. 2007). Despite the satisfactory results, the principal factor controlling final flow dimensions is the effusion rate. MAGFLOW model can take into account the way in which effusion rate changes during an eruption and how this influences the spread of lava as a function of time.

These features are of special interest, particularly as effusion rates can be highly variable. Indeed, lava effusion rates can vary by orders of magnitude over a matter of hours, and are difficult to determine in-situ. However, lava effusion rates can be estimated using thermal infrared satellite imagery obtained from low spatial/high temporal resolution remote sensing data (e.g. MODIS, AVHRR). To this end, we developed an automatic system that uses near-real-time infrared satellite data acquired by MODIS and AVHRR sensors to perform an automatic detection of thermal anomalies and effusion rate estimation to drive numerical

simulations of lava flow paths. We describe and show the operation of this system by using an analysis of the recent lava flow-forming during 2006 Etna eruption.

Method Description

We developed an automatic system that uses near-real-time infrared satellite data acquired by MODIS and AVHRR sensors to drive numerical simulations of lava flow paths. A flowchart of the system is reported in Fig. 1.

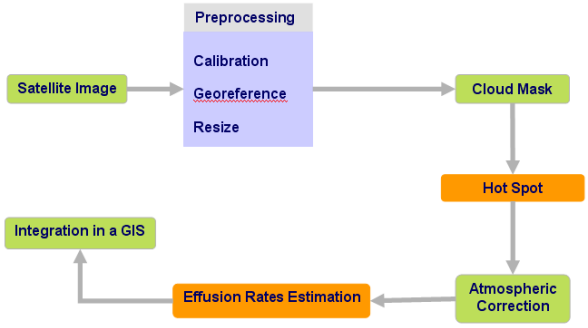

Fig. 1 - Automatic system to detect thermal anomalies and to compute effusion rate.

The first block regards the preprocessing of the images. It consists in the calibration, the geoferencing and the resizing of the data. The calibration is the process of determining the radiance or the brightness temperature starting from digital number. After the preprocessing of the data, it is necessary to build a cloud mask. It is a mask in which every pixel is classified as cloud or not, with a level of uncertainty. After that, the algorithm for hot spot detection is launched. The output of this block is a binary matrix, where the pixel classified as hot are marked. After an eventual atmospheric correction, the binary matrix is passed as input to the effusion rate algorithm, which comes back an instantaneous value minimum and maximum computed from the satellite data.

The algorithm of cloud mask detection works using some spectral tests rely on radiance (temperature) thresholds in the infrared and reflectance thresholds in the visible. The threshold are dependent from many factors as for example the considered surface (ground or sea), or the sun zenith angle (day or night). Different test were developed for AVHRR and MODIS data. For the AVHRR sensor we used the channel 1 (only for day) centred to a wavelength of 0.6 micrometers, and channel 4 and 5, corresponding to a wavelength of 11 and 12 micrometers. In particular the brightness temperature of channel 4 permit to discover high or medium clouds, the difference between channel 4 and 5 permit to detect the “hot cloud”, cirrus. The information derived from channel 1 in the visible is the more efficient, but useful only during the day hours. Moreover, sometimes was not possible to classify with absolute certainty the nature of a pixel For this reason, we introduce some uncertainty range. For MODIS data found similar tests.

To locate thermal anomalies automatically in MODIS and AVHRR data, a contextual approach is applied. This compares a pixel with its neighbours and a threshold calculated from within the image, to define whether or not a pixel is “hot”. The hot pixel detection technique uses the difference between brightness temperature in channel 21 (or 22), and in channel 31 ,defined as delta T. The channels 21 and 22 are centered in the same wavelength, 3.9 micrometers, but they have a different level of saturation temperature. So we use one channel or the other in function of the saturation of the pixel. Although channels 21 and 31 are equally sensitive to solar heated surfaces, channel 21 is more sensitive to high temperature surfaces. This means, that for pixel containing a high temperature volcanic features, delta T will be greater that for those containing solar-heated surfaces. To identify hot pixels within the volcano sub image, we compare the delta T for each pixel in the image with that of its immediate neighbourhood delta neigh. This is achieved by first setting a value for delta neigh using the mean delta T for the other eight pixels (excluding saturated pixels) in a 3X3 pixel box centred on the current target pixel. The resulting delta neigh is then subtracted from delta T of every pixel to give delta diff. The delta T diff for a target is compared with the maximum delta diff obtained from a nearby “non-volcanic” portion of the image to determine wheter the target pixel is hot or not. Here, the term natural variation, delta T nat, is used for the maximum delta T diff for the non volcanic portion of the image. The algorithm scans across the image on a pixel-by-pixel basis, being applied to each pixel in the volcano image. Pixels that have an elevated delta, but which also have hot pixels in their neighbourhood, may not be flagged during the first scan of the algorithm. This is due to the influence of the hot neighbourhood pixels in the calculation of delta T neigh for such target pixels. So that such hot pixels are included, we scan the image iteratively, excluding pixels that have already been flagged as hot in a previous iteration from the calculation of delta T neigh, until no further hot pixel are flagged.

An application to 2006 July Etna eruption hot spot detection is reported in Fig. 2. The data set analyzed is consisted of 11 cloud-free satellite imagery of MODIS sensor of TERRA and AQUA satellites. The sequence started on 15 July at 01:40 UTC time. From this data, until 24 July, hot

pixels are detected. At this date, the observed flow field is superimposed to satellite image. As it is possible to note there is an exact correspondence between the pixels flagged as hot and the real path of lava.

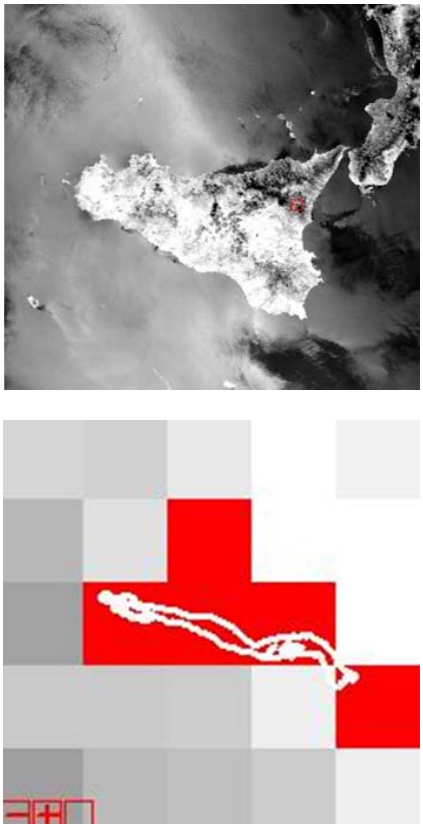

Fig. 2 – Observed flow field on 24 of July (white contour) superimposed to satellite image at the same data.

Thermal analysis is carried out for each hot pixel located to give an estimate of the size and thermal flux of the thermal feature contained within the pixel.

Harris et al. (1997, 1998, 2000) and Wright et al. (2001) showed that the total heat loss measured from satellite data can be converted to the instantaneous effusion rate (E) at the time the image data were collected using:

$$E = \frac{Q_{TOT}}{\rho\left(C_p \Delta T + C_L \Delta\phi\right)} \qquad (1)$$

where Q_{tot} is instantaneous heat loss from the flow, ρ and C_p are lava density and specific heat capacity, ΔT is eruption temperature minus solidus temperature, C_L is latent heat of crystallization, and ΔΦ is the volume percent of crystals that form while cooling through ΔT. In Tab. 1 values of parameters used in the eq. 1 are reported.

Parameter	*Symbol*	*Value*	*Unit*
Density of lava	ρ	2600	kg m^{-3}
Specific heat capacity	C_p	1150	J kg^{-1} K^{-1}
Latent heat of crystallization	C_L	$3.5*10^{-5}$	J kg^{-1}
Temperature Difference	ΔT	150-200	°K
Temperature of extrusion	T_e	1360	°K
Volume percent of crystals	ΔΦ	45%	-

Tab. 1– Parameters used in the eq. 1 to find effusion rate values.

To estimate Q_{tot}, we used the approach proposed by Dozier (1981). He presented a method to estimate temperature of subpixel hot spots in thermal satellite data. This has been applied to AVHRR data to estimate the size and temperature industrial and volcanic targets (Matson and Dozier, 1981; Harris et al., 19950). The method assumes that a pixel is occupied by three thermal components: a high-temperature component at temperature Th occupying a portion ph of the pixel, a cool component at temperature Tb (typical ambient temperature) occupying a portion pb and a medium-temperature component at temperature Tc occupying a portion pc of the pixel. The method uses channel 4 μm and 11μm radiances (R4, R11) to estimate the unknown terms by solution of simultaneous equations:

$$\begin{aligned} R_4 &= p_b L_4(T_b) + p_c L_4(T_c) + p_h L_4(T_h) \\ R_{11} &= p_b L_{11}(T_b) + p_c L_{11}(T_c) + p_h L_{11}(T_h) \end{aligned} \qquad (2)$$

in which $L_4(T)$ and $L_{11}(T)$ are the Planck function spectral radiances for a blackbody of temperature T at the channel 4 μm e 11 μm central wavelengths.

Five unknowns, p_h, p_c, T_h, T_c and T_b exist in these two equations. In order to constrain a reasonable model, valid and unique estimates are required for at least three of these parameters. We therefore assume T_h as eruption temperature and estimate T_b as typical ambient temperature adjacent to lava free pixels. Field and satellite data show that temperature for T_c can range over several hundreds of degrees, making T_c impossible to define using a single value (Oppenheimer, 1991; Flynn and Mouginis-Mark, 1992; Flynn et al., 1993). To avoid error that would be introduced by selecting a single T_c, we choose to solve the equations over a reasonable range of T_c to give a range of solutions within which the true solution must lie. Following the results of Oppenheimer (1991) and Flynn (1993), we select 100°C as a reasonable lower limit for the T_c range. T_c will have an upper

limit, above which p_h would have to become negative in order to solve equations.

In this way it is possible to define two end-member cases, a hot model and a cool model, corresponding to the upper and lower limit of T_c range. The hot model maximizes heat loss with high eruption, crack, crust, and base temperatures combined with a thin base. Conversely, the cool model minimizes heat loss and uses a thick base. The thermal total flux can be estimated by:

$$Q_{TOT} = \varepsilon\sigma\left[\left(T_h^4 A_h\right) + \left(T_c^4 A_c\right)\right] \quad (3)$$

where ε is the emissivity of lava, σ is Stephan-Boltzmann constant, and A_h and A_c are the ground areas occupied by the molten and crust components, respectively.

The thermal total flux value estimated by using eq. 3 is introduced in the eq. 1 to produce an estimate of effusion rates. Finally, these estimations are used to drive numerical simulations of lava flow paths performed by MAGFLOW model.

This model is based on Cellular Automata (CA) in which the states of the cells are the thickness of lava and the quantity of heat. The states of the cells are synchronously updated according to local rules that depend on cell's own values and the neighbor's value within a certain proximity. The evolution function of MAGFLOW is a steady state solution of Navier-Stokes equations for the motion of a Bingham fluid on a inclined plane subject to pressure force, in witch the conservation of mass is guaranteed both locally and globally. However, this kind of evolution function induces a strong dependence on the cell geometry and position of the flux, with respect to the symmetry axis of the cell: flows on a horizontal plane spread preferentially in the direction of the mesh (the calculated length of lava flows depends on the relative directions of flow and the mesh). In order to solve this problem we used a Monte Carlo approach, which allows obtaining cell geometry free results as well as calculating large-scale lava flows with no artificial anisotropy. We consider a cellular automaton that has randomized neighborhood, and define the neighborhood as all cells that are distant from the central cell less than a specified value. Therefore, we count neighbors as only the cells with the center inside a circle of a certain radius.

Once the MAGFLOW structure was defined, we had to establish the evolution function of the model. Starting from the general form of Navier-Stokes equation, we used the basic equation governing fluid motion in a pressure-driven flow in order to examine flows on a slightly inclined or flat plane (steady state solution of Navier-Stokes equation). In our simulation code, we assume that the lava flow is a Bingham fluid characterized by a yield strength (Sy) and plastic viscosity (□), and that it advances as an incompressible laminar flow. The basic formula to calculate the flux on an inclined plane was proposed by Dragoni et al. (1986). They deduced a steady solution of Navier-Stokes equations for a Bingham fluid with constant thickness (*h*), which flows downward due to gravity. The volumetric flow rate (*q*) is:

$$q = \frac{S_y h_{cr}^2 \Delta x}{3\eta}\left(a^3 - \frac{3}{2}a^2 + \frac{1}{2}\right) \quad (4)$$

where $a=h/h_{cr}$, h_{cr} is the critical thickness and Δx the distance between two adjacent cells. Other models based on this formulation were proposed in the past (e.g. Ishihara et al., 1990), but they did not consider the flow driven by the effect of self-gravity. This case was introduced by Miyamoto and Sasaki (1997), and Mei and Yuhi (2001).
The critical thickness (h_{cr}) depends on the yield strength and the angle of the slope (α), as described by:

$$h_{cr} = \frac{S_y}{\rho g\left(\sin\alpha - \frac{\partial h}{\partial x}\cos\alpha\right)} \approx \frac{S_y\sqrt{\Delta z^2 + \Delta x^2}}{\rho g\left(\Delta z - \Delta h\right)} \quad (5)$$

where ρ is the density of lava, g the acceleration due to gravity, Δz the difference in height between two cells and Δh the increase in cell thickness.
At any time t, the heat content of lava (Q_t) in each cell is carried in accordance with the flow motion. The temperature of the lava in a cell is considered uniform: vertical temperature variation is neglected. For the cooling mechanism, we consider the radiative heat loss ($\Delta Q_{t,r}$) only from the surface of the flow (the effects of conduction to the ground and convection to the atmosphere are neglected), and the change of heat ($\Delta Q_{t,m}$) due to the mixture of lava between cells with different temperatures, hence:

$$Q_{t+\Delta t} = Q_t + \Delta Q_{t,m} - \Delta Q_{t,r} \quad (6)$$

where:

$$\Delta Q_{t,m} = \left(\sum_{q_i>0} q_i T_i + \sum_{q_i<0} q_i T\right)\rho c_v \Delta t \quad (7)$$

and

$$\Delta Q_{t,r} = \varepsilon A \sigma T^4 \Delta t \quad (8)$$

where T is the temperature of the central cell, Ti is the temperature of neighbor cells, qi is the flux between the central cell (i.e. the cell for which the state variables are updated) and its i-th neighbor, c_v is the specific heat per unit mass, □ is the emissivity of lava, A is area of the cell and □ is the Stefan-Boltzmann constant. Then, the new temperature from the calculated heat change is:

$$T_{t+\Delta t} = \frac{Q_{t+\Delta t}}{\rho c_v h_{t+\Delta t} A} \quad (9)$$

where $h_{t+\Delta t}$ is the new thickness.

The necessary data to run MAGFLOW are knowledge of the rheological properties of the lava, a digital representation of the topography over witch the lava is to be emplaced, the location of the eruptive vent and an estimate of the lava effusion rate.

At the initial state, the lava thickness at each cell is set to zero. The lava flow starts discharging at a certain rate from a cell (or more cells) corresponding to the vent. The thickness of lava at the vent cell increases by a rate calculated from the volume of lava extruded during each time interval (of course, the flow rate for each vent can change in time). When the thickness at the vent cell reaches a critical level, the lava spreads over the neighbour cells. Next, whenever the thickness at any cell exceeds the critical thickness, the lava flows to the adjacent cells.

Application to 2006 Etna eruption

The MAGFLOW model proposed here was applied to reproduce the lava flow outpoured during the 2006 July Etna eruption. The 2006 Etna eruption provided the opportunity to verify our model's ability to predict the path of lava flows while the event was ongoing and to produce different scenarios as eruptive conditions changed. At 23:30 local time on 14 July 2006, a fissure opened on the east flank of the South-East Crater (SEC) summit cone of Mt Etna. Two vents (B1 and B2) along the fissure produced a lava flow spreading east to the Valle del Bove. We simulated step-by-step the whole effusive activity, during the period of 14 July – 29 July 2006, produced from two vents: B1 and B2, opened between 3000 m and 3100 m a.s.l. The parameters used for the simulation are reported in the Tab. 2.

As a topographic basis, we used the digital elevation model of the Etna maps updated until August 2005 with a horizontal resolution of 5 m, obtained from Universitò of Roma La Sapienza.

Rheological properties were modeled using a variable viscosity relationship by Giordano and Dingwell (2003), parameterized in terms of temperature and water content, and linearized between solidification (1143 K) and extrusion temperature (1360 K), as:

$$\log \eta(T) = a + bT \quad (10)$$

where *a* e *b*, for a fixed water content of 0.7 wt% H2O, are 24.4226 and -0.0166 respectively. Typical material properties of many basaltic rocks occurring in volcanic regions were chosen for Etnean basaltic lava (Kilburn and Guest, 1993, Harris et al., 1997). The average density and specific heat of the lava are 2600 kg/m3 and 840 J kg-1 K-1,respectively. The eruption temperature of the lava at the point of discharge from the crater was chosen to be 1360 K with the ground temperature being 300 K.

Parameter	*Symbol*	*Value*	*Unit*
Density of lava	ρ	2600	kg m^{-3}
Specific heat	c_v	1150	J kg^{-1} K^{-1}
Emissivity of lava	ε	0.9	-
Temperature of solidification	T_s	1143	°K
Temperature of extrusion	T_e	1360	°K

Tab.2 – Parameters used in the MAGFLOW model

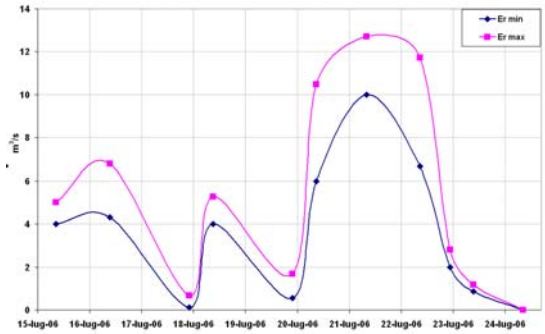

Fig. 3 – Effusion rate estimated during the 2006 July Etna eruption

The lava effusion rate was estimated using thermal infrared satellite data coming from MODIS sensor. Since they can be obtained from low spatial/high temporal resolution remote sensing data, such effusion rates can be determined at regular intervals during an eruption.

Our satellite-based data consisted of thermal data from MODIS satellite-borne radiometers (TERRA - AQUA) acquired from 15 July 2006 to 25 July 2006, for a total of 11 cloud-free images.

Figure 3 shows both the estimated values of effusion rate for the whole period of the eruption that were used t guide lava flow simulations using the MAGFLOW cellular automata algorithm (Fig. 4).

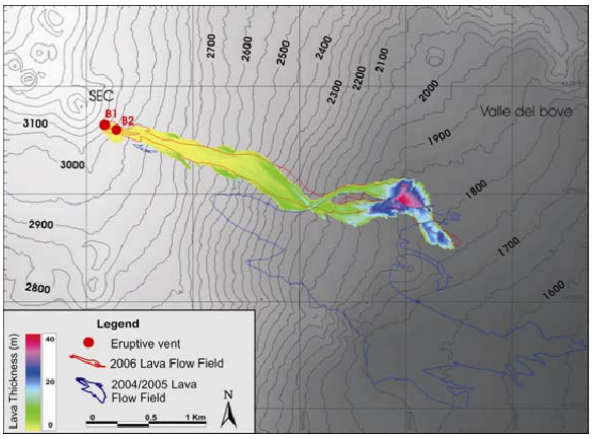

Fig. 4 – Simulated scenario updated to 24 July 2006 (colored layer) superimposed to observed flow field at the same date (red contour). Diverse colors of simulated path are associated to different thickness.

Conclusions

The lava flow hazard on Etna volcano was evaluated during the ongoing 2006 Etna eruption by means of the MAGFLOW cellular automata model. This model was developed for simulating lava flow paths and the temporal evolution of lava emplacement. Many data are necessary to run MAGFLOW and to determine how far lava will flow. However, for a given composition, the volumetric flux of lava from the vent is the principal factor controlling final flow dimensions. As such, simulations that take into account the way in which effusion rate changes during an eruption, and how this influences the spread of lava as a function of time, are of special interest, particularly as effusion rates can be highly variable. To this end, during the latest eruptions of Etna, occurring in July and October 2006, the lava effusion rates were estimated at regular intervals using thermal infrared satellite data. The 2006 Etna eruptions represented a further step towards defining the true potential of the MAGFLOW model as an effective tool for real-time forecasting of lava flow hazards. We will briefly summarize results obtained by comparing the simulated and the real events.

Reference

Crisci, G. M., Di Gregorio, S., Pindaro, O., Ranieri, G., (1986) Lava flow simulation by a discrete cellular model: first implementation, Int. J. Modelling and Simulation, 6, pp. 137-140

Costa, A., Macedonio, G., (2005) Numerical simulation of lava flows based on depth-averaged equations. Geophys. Res. Lett., 32 L05304 doi:10.1029/2004GL021817.

Del Negro, C., Fortuna, L., Herault, A., Vicari, A., (2006) Simulations of the 2004 lava flow at Etna volcano by the magflow Cellular Automata model, Bulletin of Volcanology, submitted.

Dragoni, M., Bonafede, M., Boschi, E., (1986) Downslope flow models of a Bingham liquid: implications for lava flows. J. Volc. Geotherm. Res., 30, pp. 305-325

Giordano, D., Dingwell, D., (2003) Viscosity of hydrous Etna basalt: implications for Plinian-style basaltic eruptions. Bull. Volcanol., 65, pp. 8-14, doi: 10.1007/s00445-002-0233-2

Harris, A., Blake, S., Rothery, D., Stevens, N., (1997) A chronology of the 1991 to 1993 Mount Etna eruption using advanced very high resolution radiometer data: implications for real-time thermal volcano monitoring. J. Geophys. Research, 102, pp. 7985-8003

Ishihara, K., Iguchi, M., Kamo, K., (1990) Numerical simulation of lava flows on some volcanoes in Japan. In: Lava Flows and Domes: Emplacement Mechanisms and Hazard Implications, edited by J. K. Fink, pp. 174-207, Springer Berlin

Kilburn, C. R. J., Guest, J. E., (1993) Aa lavas of Mount Etna, Sicily. In: Active Lavas: Monitoring and Modeling, edited by C. R. J. Kilburn and Luongo, pp. 73-106, UCL Press London

Lautze, N., Harris, A., Bailey, J., Ripepe, M., Calvari, S., Dehne, J., Rowland, S., Evans-Jones, K., (2004) Pulsed lava effusion at Mount Etna during 2001. J. Volcanol. Geotherm. Res., 137, pp. 231-246

Mei, C. C., Yuhi, M., (2001) Slow flow of a Bingham fluid in a Shallow Channel of Finite Width, J. Fluid Mechanics, 431, pp. 135-160

Miyamoto, H., Sasaki, S., (1997) Simulating lava flows by an improved cellular automata method, Computers & Geosciences, 23 (3), pp. 283-292

Vicari, A., Herault, A., Del Negro, C., Coltelli, M., Marsella,M., Proietti, C., (2006) Simulations of the 2001 lava flow at Etna volcano by the magflow Cellular Automata model, EM&S, in press.

Wright, R., Blake, S., Harris, A., Rothery, D., (2001) A simple explanation for the space-based calculation of lava eruption rates, Earth and Planetary Science Letters, 192, pp. 223-233

Young, P., Wadge, G., (1990) FLOWFRONT: simulation of a lava flow, Computers & Geosciences, 16 (8), pp. 1171-1191.

SENSITIVITY ANALYSIS OF MAGFLOW MODEL AS POST-OPTIMIZATION TOOL

*Alessia Ciraudo * and Annamaria Vicari*

Isitituo Nazionale di Geofisica e Vulcanologia, Sezione di Catania
** Email: ciraudo@ct.ingv.it*

Abstract

The sensitivity analysis for the MAGFLOW model has been performed to evaluate how the parameters and the structure of the model affect the lava flow simulations. We focused on parameter sensitivity. The preliminary results show as the emissivity, the two coefficients of the viscosity and the yield strength condition strongly the calculated simulations, in comparison to the density, the temperature of solidification and extrusion and the heat capacity.

Key words: MAGFLOW model, sensitivity analysis, post-optimization tool.

Introduction

Sensitivity analysis is used to determine how "sensitive" a model is to changes in the value of its parameters and to changes in its structure. In this paper, we focus on parameter sensitivity. Parameter sensitivity is usually performed as a series of tests in which the modeler sets different parameter values to see how a change in the parameter causes a change in the dynamic behavior of the stocks. By showing how the model behavior responds to changes in parameter values, sensitivity analysis is a useful tool in model building as well as in model evaluation. Sensitivity analysis helps to build confidence in the model by studying the uncertainties that are often associated with parameters in models. Many parameters in system dynamics models represent quantities that are very difficult, or even impossible to measure to a great deal of accuracy in the real world. Also, some parameter values change in the real world. Therefore, when building a system dynamics model, the modeler is usually at least somewhat uncertain about the parameter values he chooses and must use estimates. Sensitivity analysis allows him to determine what level of accuracy is necessary for a parameter to make the model sufficiently useful and valid. If the tests reveal that the model is insensitive, then it may be possible to use an estimate rather than a value with greater precision. Discovering that the system behavior greatly changes for a change in a parameter value can identify a leverage point in the model a parameter whose specific value can significantly influence the behavior mode of the system.

Using the MAGFLOW model for lava flow simulations, we have observed as different input parameters, among witch lava's rheological and physic properties, condition strongly the goodness of the output. So, to estimate the error committed we have implemented sensitivity test for these factors. Among the various techniques existing we have chosen to use the method of Morris (1991). This scheme allows to establish as input factors influence the output, with negligible, linear o nonlinear effects, and as they have involved in interactions with other factors.

In general, from the ranges of variation chosen for each factor, we will generate a set of input values for the simulator. Then the output of the simulations will be analyzed to valuate as a perturbation of input parameters conditions the final output and therefore to obtain a combination of the input factors that produce a simulation that reflects the real lava flow.

Morris Method

To the base of the method of Morris there is the concept of elementary effect, defined for a generic factor i as

$$d_i(\mathbf{x}) = \frac{y(x_1,\ldots,x_{i-1},x_i+\Delta_i,x_{i+1},\ldots,x_k) - y(\mathbf{x})}{\Delta_i} \quad (1)$$

with x k-dimensional vector representing the k input factors, y the function to evaluate the model, Δi relative distance between two vectors.

So the objective of the method is to estimate r elementary effects for each input factor, where r is the sample size of the experiment, and to compute the mean and the standard deviation of the distributions of these elementary effects. The first value gives a estimate of the effect that the

factor has on the output. The second, instead, represents a sum of all interactions of a factor with the others.

The first step of the method of Morris consists in the choice of a function (interest function) to evaluate the output of the model. We can compare a simulated lava flow with an observed on different point of view, such as an analysis of the front of the flow or a valuation based on the area invaded. If we consider the front of the flow as comparison, that is the max distance reached, then we can consider our function defined as the difference between the front of the real and the simulated flow. Instead, the area of invasion may be analyzed under different aspect, such as the difference between the total areas, or an estimate of overlapped, underestimated and overestimated areas.

The second step consists in to select the k factors variables (input parameters) for the model and to impose their range of variation physically valid. In particular, we have chosen nine factors: the two coefficients for the viscosity and those for the yield strength, the density, the solidification and extrusion temperature, the heat capacity and the emissivity. Since the first simulations, we have observed as the viscosity and the yield strength influence strongly the evolution of the simulation. In fact, the choice of these range of variation has been effected carefully, because it needs that the combination between the two coefficients will produce outputs physically reliable. So rather than to give a range of variation for these, we have thought to give one of it for the logarithm of each parameters. On the base of past estimate, we have considered as viscosity's coefficient:

- a = 25,3496
- b = 0,0167719

and for yield strength:

- c = 13,9997
- d = 0,0089.

So, in accordance with the physical laws

$$\log \eta(T) = a + bT$$
$$\log S_y(T) = c + dT \qquad (2)$$

that represent, respectively, the dependence of the viscosity (η) and the yield strength (S_y) from the temperature (T), we have calculated the minimum and the maximum value for each parameter in function of the solidification and extrusion temperature, obtaining the correspondent range of variation.

Properties	***Min value***	***Max value***
Density (Kg/m3):	2400	2700
Temperature of solidification (K):	800	1000
Emissivity:	0.8	1
Heat capacity:	840	1150
Temperature of extrusion (K):	1335	1385
Max viscosity (to the temp. of solidification):	8.5	12
Min viscosity (to the temp. of extrusion):	2	4
Max yield strength (to the temp. of solidification):	5	7
Min yield strength (to the temp. of the extrusion):	1.5	2.5

Tab. 1 - Range of variation of the input factors

For the method of Morris, each factor may assume a prefixed discrete number of values, called levels, which are chosen in own range of variation. So the next step in the method consists in to establish the sample size r, that is the number of trajectories in the input space, and the number of levels p to which the factors must be sampled. From this number, the value □i, representing the relative distance between two consecutive points in a generic trajectory, can be calculated for a factor i, such as

$$\Delta_i = \frac{p}{2(p-1)}(b_i - a_i) \qquad (3)$$

with a_i and b_i are the extremities of the range of variation of the ith factor.

Now, we can create the r trajectories in the input space. For each trajectory we select a k-dimensional vector, **x***, in which every component x_i is sampled from the set of possible values of ith factor. This vector isn't used as input for the model, but only to generate the *k+1* sample points. So each trajectory's point will be created beginning from the vector **x*** by increasing one or more components by relative value □, such that every point differs from the foregoing in only one component that has been either increased or decreased by the correspondent value □. The succession of *k+1* sampling points defines a trajectory in the input space and also a matrix **B***, with dimension *(k+1) x k*, called Orientation matrix. In our case, we have chosen six levels for each factor and ten trajectories, so we have obtained 100 input vectors.

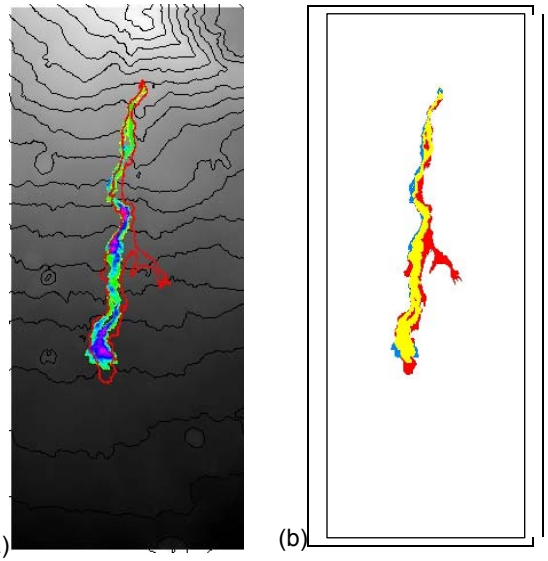

(a) (b)

Fig. 1 – Simulated scenario of 2001 Etna eruption. (a) The different colours of the simulated lava flow represent diverse lava thicknesses. (b) Evaluation map of the simulation. In yellow the overlapped areas, in red the underestimated areas and in blue the overestimated areas.

Evaluation of the model

For every point of the r trajectories created, the model must be evaluated. So we have effected the 100 simulations and for each of these we have calculated the selected interest function. In the Fig. 1 the simulated scenario of 2001 Etna eruption is shown. In particular in the Fig. 1 (a) the simulated lava flow (coloured layer) is overlapped to the observed lava flow field (red contour). Instead in Fig. 1 (b) we still observe the overlapping of the two flow, but identifying the different type of area, overlapped, overestimated and underestimated, respect than the observed flow.

After that the r trajectories have been built and the model has been evaluated in every point, for each factor *i* the relatives elementary effects d_i can be calculated, such as:

$$d_i(\mathbf{x}^{(l)}) = \frac{y(\mathbf{x}^{(l+1)}) - y(\mathbf{x}^{(l)})}{\Delta_i} \quad (4)$$

if Δi has been incremented,

$$d_i(\mathbf{x}^{(l)}) = \frac{y(\mathbf{x}^{(l)}) - y(\mathbf{x}^{(l+1)})}{\Delta_i} \quad (5)$$

if Δi has been decremented, such as $x^{(l)}$ and $x^{(l+1)}$, for $l = 1, \ldots, k$, are two consecutive points in the same trajectory differing in the ith component.

Therefore we can say that every orientation matrix gives only an elementary effect for each input factor and so the *r* matrices furnish a *kr-dimensional* sample. In other words, each factor will have to the end *r* elementary effects.

The last step of the method Morris consists to calculate for each factor *i* the mean μ and the standard deviation σ of the correspondent distribution of elementary effects:

$$\mu_i = \sum_{j=1}^{r} \frac{d_{ij}}{r} \quad (6)$$

$$\sigma_i = \sqrt{\sum_{j=1}^{r} (d_{ij} - \mu_i)^2 / r} \quad (7)$$

2525	***916.6666667***	***0.85***	***1020.833333***	***1355.833333***	***9.958333333***	***3.5***	***6.833333333***	***2.25***
2675	***916.6666667***	***0.85***	***1020.833333***	***1355.833333***	***9.958333333***	***3.5***	***6.833333333***	***2.25***
2675	***816.6666667***	***0.85***	***1020.833333***	***1355.833333***	***9.958333333***	***3.5***	***6.833333333***	***2.25***
2675	***816.6666667***	***0.95***	***1020.833333***	***1355.833333***	***9.958333333***	***3.5***	***6.833333333***	***2.25***
2675	***816.6666667***	***0.95***	***865.8333333***	***1355.833333***	***9.958333333***	***3.5***	***6.833333333***	***2.25***
2675	***816.6666667***	***0.95***	***865.8333333***	***1355.833333***	***9.958333333***	***2.5***	***6.833333333***	***2.25***
2675	***816.6666667***	***0.95***	***865.8333333***	***1355.833333***	***11.70833333***	***2.5***	***6.833333333***	***2.25***
2675	***816.6666667***	***0.95***	***865.8333333***	***1380.833333***	***11.70833333***	***2.5***	***6.833333333***	***2.25***
2675	***816.6666667***	***0.95***	***865.8333333***	***1380.833333***	***11.70833333***	***2.5***	***6.833333333***	***1.75***
2675	***816.6666667***	***0.95***	***865.8333333***	***1380.833333***	***11.70833333***	***2.5***	***5.833333333***	***1.75***

Tab. 1 - An example of Orientation Matrix generated.

If the distribution of elementary effects of some factor includes negative values, then calculating the mean some effects can be erased by others. To solve this problem, Campolongo et al. (2003) propose a little variant of method, that is to consider the distribution of the absolute values of elementary effects during the estimate of the mean, μ^*.

The mean is an estimate to identify the input factors which have more influence on the output. In fact, we can say that if it has a high value, then the relative factor have a substantial effect on the output. Instead the standard deviation can be used to detect the factors involved in interaction with other factors or whose effect is nonlinear.

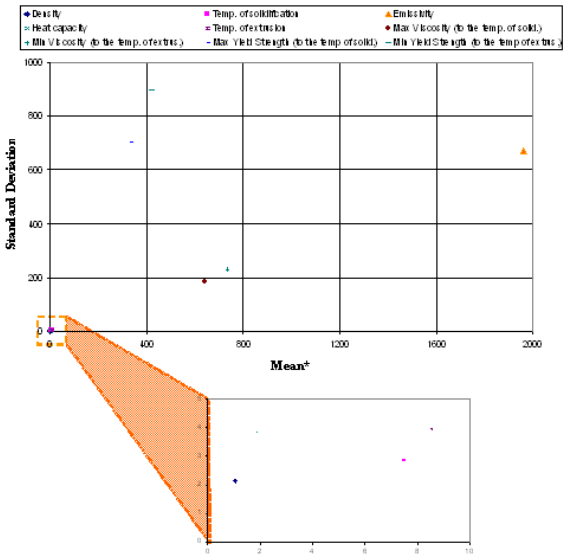

Fig. 2 - The first results obtained by the method of Morris.

Conclusions

This is a work still in progress. At present we have effected all the simulations and we have collected the interest data that is the difference of front between the simulated and the real and the value of the different areas. All these data are in elaboration. In particular the first data which we are analyzing refer to the evaluation of the model on the base of the function relative to the difference of the front. From this graphic we can see as the emissivity, the two coefficients of the viscosity and the yield strength condition strongly the output, in comparison to the density, the temperature of solidification and extrusion and the heat capacity.

Currently we are working to find an interest function which expresses better the goodness of a result. Moreover we are thinking to enlarge the range of variation of some parameters and we are searching to improve the meaning given to the value of the mean and the standard deviation.

References

Campolongo, F., Saltelli, A., Jensen, N. R., Wilson, J., Hjorth, J., 1999, The role of multiphase chemistry in the oxidation of dimethylsulphide (DMS). A latitude dependent analysis, Journal of Atmospheric Chemistry, 32, 327-356

Morris M. D., 1991, Factorial sampling plans for preliminary computational experiments, Technometrics, 33(2): 161-174

Saltelli A. Tarantola S., Campolongo, F., Ratto, M., (2004), Sensitivity Analysis in Practice. A Guide to Assessing Scientific Models , John Wiley & Sons publishers

Saltelli, A., Tarantola, S., Campolongo, F., and Ratto, M., 2005, Sensitivity Analysis for Chemical Models, Chemical Reviews, 105(7), pp 2811 - 2828

Saltelli A., Chan K., Scott E.M., 2000, Sensitivity Analysis, John Wiley & Sons publishers, Probability and Statistics series, 355-365

Vicari, A. , Herault, A., Del Negro, C.; Coltelli, M., Marsella, M., Proietti, C. (2007). Modelling of the 2001 Lava Flow at Etna Volcano by a Cellular Automata Approach, Environmental Modelling & Software , 22, 1465-1471

NUMERICAL THERMAL MODEL FOR SIMULATING LAVA FLOWS

Alexis Herault

Isitituo Nazionale di Geofisica e Vulcanologia, Sezione di Catania
Email: herault@ct.ingv.it

Abstract

We developed the numerical resolution of cooling and solidification process of lava flows. Firstly, we analyzed the heat equation with the different boundary conditions ignoring the state transition of the fluid. Secondly, we considered the generic case, introducing the phase change.

Key words: lava flows, thermal model.

Introduction

The thermal processes play a fundamental role on the dynamic of lava flows. In fact, during the eruption the gradual lava cooling cause an alteration of its rheological properties due to the heat conduction to the ground and the radiative heat loss from the surface of the flow.

We have developed the numerical resolution of cooling and solidification process in two parts. First, we have analyzed the heat equation with the different boundary conditions ignoring the state transition of the fluid. Then we have considered the generic case, introducing the phase change.

Heat equation

The one-dimensional heat equation is expressed by:

$$\frac{\partial T}{\partial t} = k \frac{\partial^2 T}{\partial x^2} \tag{1}$$

with k the thermal diffusivity of the fluid, $x \in [x_0, x_M]$, $t \in [t_0, t_N]$ and initial condition $T(x, t_0) = f(x)$, with *f(x)* a generic function in *x*.

We have solved numerically this equation using the method of finite differences. We have assumed equal spacing of the points x_j in one dimension with spatial step

$$\Delta x = \frac{x_M - x_0}{M}$$

with *M* number prefixed of discretization point, such as:

$x_j = x_0 + j\Delta x$ for $j = 0, \ldots, M$

and equal spacing of the time-steps t_n at intervals of:

$$\Delta t = \frac{t_N - t_0}{N}$$

with *N* number of temporal steps considered, such as:

$t_n = t_0 + n\Delta t$ for $n = 0, \ldots, N$

So we can estimate the second derivative with the central-difference approximation:

$$\frac{\partial^2 T}{\partial x^2} = \frac{T(x_{j-1}, t) - 2T(x_j, t) + T(x_{j+1}, t)}{\Delta x^2}$$
$$j = 1, \ldots, M-1$$

obtaining from (1) a system of ODE:

$$\frac{\partial}{\partial t} T(x_j, t) = k \frac{T(x_{j-1}, t) - 2T(x_j, t) + T(x_{j+1}, t)}{\Delta x^2}$$
$$j = 1, \ldots, M-1$$

To solve instability problem deriving from explicit time-stepping, we have chosen to use the backward Euler algorithm. This method evaluates the spatial derivatives in the new time-step

$$\frac{T(x_j, t_{n+1}) - T(x_j, t_n)}{\Delta t} =$$
$$= k \frac{T(x_{j-1}, t_{n+1}) - 2T(x_j, t_{n+1}) + T(x_{j+1}, t_{n+1})}{\Delta x^2}$$
$$j = 1, \ldots, M-1$$
$$n = 0, \ldots N-1 \tag{2}$$

then the new temperature field values may not be calculated independently, but the obtained

equations must be solved simultaneously. Defining the number:

$$c = \frac{k\Delta t}{\Delta x^2}$$

the system (2) can be rewritten as:

$$\begin{aligned} &(1+2c)T(x_j,t_{n+1}) - cT(x_{j-1},t_{n+1}) + \\ &- cT(x_{j+1},t_{n+1}) - T(x_j,t_n) = 0 \\ &j = 1,\ldots,M-1 \\ &n = 0,\ldots N-1 \end{aligned} \qquad (3)$$

For the resolution of this linear equations system, we must consider the boundary conditions.

Dirichlet Boundary Conditions

The Dirichlet boundary conditions impose a constant temperature, or related to the time, at the extremities of the mean:

$$\begin{cases} T(x_0,t) = T_i(t) \\ T(x_M,t) = T_f(t) \end{cases}$$

Introducing this equation in the system (3), we obtain:

$$\begin{cases} T(x_0,t_{n+1}) = T_i(t_{n+1}) \\ (1+2c)T(x_j,t_{n+1}) - cT(x_{j-1},t_{n+1}) - cT(x_{j+1},t_{n+1}) = T(x_j,t_n) \qquad j = 1,\ldots,M-1 \\ T(x_M,t_{n+1}) = T_f(t_{n+1}) \end{cases} \qquad (4)$$

that represent a three-diagonal linear system of *M+1* equations in *M+1* variables, resolvable with a factorization *LU* of the three-diagonal matrix of coefficients

$$\mathbf{A}\mathbf{T}^{n+1} = \mathbf{T}^n \quad \Rightarrow \quad \mathbf{L}\mathbf{U}\mathbf{T}^{n+1} = \mathbf{T}^n$$

So, the solution to the initial problem (4) is now easy given by the solution of the systems:

- $\mathbf{LY} = \mathbf{T}^n$ with forward substitutions;
- $\mathbf{UT}^{n+1} = \mathbf{Y}$ with backward substitutions.

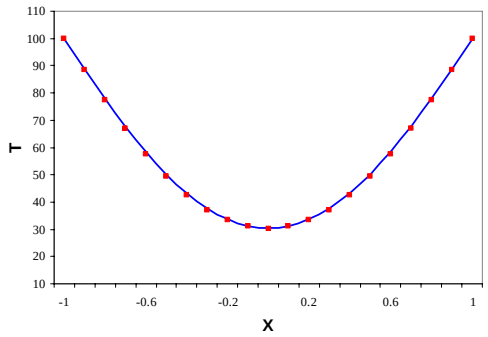

Fig. 1 - Numerical (red points) and analitical solution (blu line) of heat equation with Dirichlet boundary condictions.

To estimate the error on the numerical solution, we have considered the analytical solution in a particular case. Imposing a constant temperature, T_0, to the extremities of the mean, [*L, -L*], and a constant initial temperature, T_i, the exact solution to the heat equation is given by:

$$T(x,t) = T_0 + 4\frac{T_i - T_0}{\pi}\sum_{n=0}^{\infty}\frac{(-1)^n}{(2n+1)}\cdot$$
$$\cdot\exp\left(-(2n+1)^2\frac{\pi^2}{4}\frac{kt}{L^2}\right)\cos\left[\frac{(2n+1)\pi x}{2L}\right]$$

The figure 1 shows an example of temperature profile obtained.

Neuman Boundary Conditions

The Neuman boundary conditions impose a heat flux to the extremities of the mean:

$$\left.\frac{\partial T}{\partial x}\right|_{x_0} = \frac{\phi}{\lambda} \qquad \left.\frac{\partial T}{\partial x}\right|_{x_M} = -\frac{\phi}{\lambda}$$

with ϕ heat flux and λ thermal conductivity, such as the thermal diffusivity is given by:

$$k = \frac{\lambda}{\rho \cdot cc}$$

with *cc* heat capacity and ρ density. Before introducing these conditions in our system, they must be approximate. In particular, we can say that in a general case:

$$\frac{\partial T}{\partial x} \approx \frac{T(x+\Delta x) - T(x)}{\Delta x} \qquad (5)$$

so, the conditions become:

$$\frac{T(x_1) - T(x_0)}{\Delta x} = \frac{\phi}{\lambda}$$

$$\frac{T(x_M) - T(x_{M-1})}{\Delta x} = -\frac{\phi}{\lambda}$$

Inserting them to the initial system (3), we obtain:

$$\begin{cases} T(x_0, t_{n+1}) = T(x_1, t_{n+1}) - \dfrac{\phi \cdot \Delta x}{\lambda} \\ (1+2c)T(x_j, t_{n+1}) - cT(x_{j-1}, t_{n+1}) - cT(x_{j+1}, t_{n+1}) = T(x_j, t_n) \qquad j = 1,\ldots,M-1 \\ T(x_M, t_{n+1}) = T(x_{M-1}, t_{n+1}) - \dfrac{\phi \cdot \Delta x}{\lambda} \end{cases}$$

that still represents a three-diagonal linear system resolvable with a direct method, as make with the Dirichlet boundary conditions.

Imposing a constant heat flux, ϕ, to the extremities of the mean, $[L, -L]$ and an initial temperature T_i, the exact solution to the heat equation is given by:

$$T(x,t) = T_i + \frac{\phi t}{\rho c L} + \frac{\phi L}{\lambda}\left[\frac{3x^2 - L^2}{6L^2} + \right.$$
$$\left. - \frac{2}{\pi^2}\sum_{n=1}^{\infty}\frac{(-1)^n}{n^2}\exp\left(-\frac{kn^2\pi^2 t}{L^2}\right)\cos\left(\frac{n\pi x}{L}\right)\right]$$

The figure 2 shows the temperature profiles in a simple example.

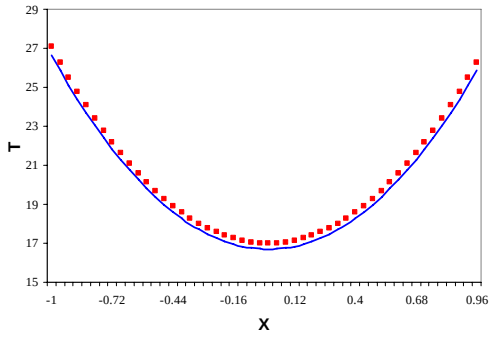

Fig. 2 - Numerical (red points) and analytical (blue line) solution of heat equation with Neuman boundary conditions.

Boundary conditions for radiation loss

The boundary conditions for radiation loss appear as

$$\begin{cases} \left.\dfrac{\partial T}{\partial x}\right|_{x_0} = \dfrac{\sigma\varepsilon}{\lambda}\left[T(x_0)^4 - T_{ext}^4\right] \\ \left.\dfrac{\partial T}{\partial x}\right|_{x_M} = -\dfrac{\sigma\varepsilon}{\lambda}\left[T(x_M)^4 - T_{ext}^4\right] \end{cases}$$

with σ Stephan constant, ε emissivity factor , λ thermal conductivity and T_{ext} extern temperature. We can approximate the equations on the base of (5) as:

$$\begin{cases} \dfrac{T(x_1) - T(x_0)}{\Delta x} = \dfrac{\sigma\varepsilon}{\lambda}(T(x_0)^4 - T_{ext}^4) \\ \dfrac{T(x_M) - T(x_{M-1})}{\Delta x} = -\dfrac{\sigma\varepsilon}{\lambda}(T(x_M)^4 - T_{ext}^4) \end{cases}$$

Inserting them to the initial system (3), we obtain:

$$\begin{cases} \frac{\sigma\varepsilon}{\lambda}\Delta x T(x_0,t_{n+1})^4 + T(x_0,t_{n+1}) - T(x_1,t_{n+1}) - \frac{\sigma\varepsilon}{\lambda}\Delta x T_{ext}^4 = 0 \\ (1+2c)T(x_j,t_{n+1}) - cT(x_{j-1},t_{n+1}) - cT(x_{j+1},t_{n+1}) - T(x_j,t_n) = 0 \qquad j = 1,\ldots,M-1 \\ \frac{\sigma\varepsilon}{\lambda}\Delta x T(x_M,t_{n+1})^4 + T(x_M,t_{n+1}) - T(x_{M-1},t_{n+1}) - \frac{\sigma\varepsilon}{\lambda}\Delta x T_{ext}^4 = 0 \end{cases} \quad (6)$$

This represents a nonlinear system, resolvable with the Newton's method for more variable. Defining the Jacobian as:

$$J_{kj}(T^{n+1}) = \frac{\partial f_k(T^{n+1})}{\partial T_k}$$

where Tn+1 represents the temperature valuated to the time n+1 in any point, Tk the temperature calculated in xk at any time and fk the kth equation of the system, such as:

$$J(T^{n+1}) = \begin{vmatrix} 4\frac{\sigma\varepsilon}{\lambda}\Delta x T(x_0,t_{n+1})^3 + 1 & -1 & 0 & \cdots & \cdots & \cdots & 0 \\ -c & 1+2c & -c & 0 & & & \vdots \\ 0 & -c & 1+2c & -c & 0 & & \vdots \\ \vdots & & \ddots & \ddots & \ddots & & \vdots \\ \vdots & 0 & & \ddots & \ddots & \ddots & 0 \\ \vdots & & & & -c & 1+2c & -c \\ 0 & \cdots & \cdots & \cdots & 0 & -1 & 4\frac{\sigma\varepsilon}{\lambda}\Delta x T(x_M,t_{n+1})^3 + 1 \end{vmatrix}$$

we can rewrite the system (6) as:

$$J(T^{n+1})Z = -B(T^{n+1})^T$$

where:

$$B(T^{n+1}) = \begin{vmatrix} \frac{\sigma\varepsilon}{\lambda}\Delta x T_{ext}^4 & -T(x_1,t_n) & \cdots & \cdots & -T(x_{M-1},t_n) & \frac{\sigma\varepsilon}{\lambda}\Delta x T_{ext}^4 \end{vmatrix}$$

and to resolve this linear system in variables Z_i, obtaining the solution to the initial nonlinear system setting

$$T(x_j,t_{n+1}) = Z_j + T(x_j,t_n)$$

Heat transfer with phase change

In this case we have three equations, one for each different fluid state:

- in the solid state

$$\frac{\partial T_s}{\partial t} = k_s \frac{\partial^2 T_s}{\partial x^2}$$

with k_s thermal diffusivity of the solid;

- in the liquid state

$$\frac{\partial T_l}{\partial t} = k_l \frac{\partial^2 T_l}{\partial x^2}$$

with k_l thermal diffusivity of the liquid;

- in the solid-liquid interface

$$\lambda_s \left(\frac{\partial T_s}{\partial x} \right)_X - \lambda_l \left(\frac{\partial T_l}{\partial x} \right)_X = L\rho_l \frac{dX}{dt}$$

with ρ_l density of the liquid, L thermal energy, λ_s and λ_l respectively thermal conductivity of the solid and liquid and X position of the solid-liquid interface.

To resolve the problem, we have considered the work of E. Duff and C. Davidson. They have developed a 2D thermal model, called 2DSOL, to simulate the solidification process, based on Eulerian coordinate system and a non-uniform, fixed mesh. It needs, in fact, that the mesh is sufficiently fine where the variation of the temperature is steep, which is in the solid-liquid interface.

For the spatial discrete approximation, the mesh-fitted control volume method has been used. The spatial domain has been divided into a number of non-overlapping control volumes, so that there is only one control volume surrounding each node. These volumes are fitted to the mesh and then the nodes are placed at the centre of each control volume. This technique guarantees that the nodal temperature is a good representative of the temperature throughout the control volume.

The next step in the research of the numerical solution consists in the temporal discretization. This is fundamental for the accuracy of the solution. In general, an accurate solution can be obtained when the time-step is sufficiently small. But if the temperature changes rather slowly with respect to time, then a small time-step isn't necessary. Besides, the time-step imposes a stability condition using an implicit method for the resolution of the ODE. On the other hand, the implicit methods are unconditionally stable, but if the time-step is too large then there is a possibility that they may give an incorrect solution. Finally, all the equations obtained can be resolved by the iterative Gauss-Seidel method.

To estimate the error in the approximation, we have considered also the analytical solution. Assuming that the fluid is to contact with a block at constant temperature lower to the solidification temperature of the fluid, the analytical solution at the time t is given by:

$$T_s(x) = T_0 + (T_1 - T_0) \frac{erf \dfrac{x}{\sqrt{4k_s t}}}{erf \dfrac{\rho_l}{\rho_s} \dfrac{K}{\sqrt{4k_s}}}$$

for the solid state, and

$$T_l(x) = T_2 + (T_1 - T_2) \frac{erfc \dfrac{x}{\sqrt{4k_l t}}}{erfc \dfrac{K}{\sqrt{4k_l}}}$$

for the liquid state, with T_0 the temperature of the block, T_1 the solidification temperature of the fluid, k_s and k_l the thermal diffusivity of the solid and liquid, ρ_s and ρ_l the density of the solid and liquid, T_2 the initial temperature of the fluid and K a variable to be determined from the balance equation at the interface.

For the water-ice system there is an approximation for the variable

$$K = \sqrt{\frac{2(T_1 - T_0)\lambda_s \rho_s}{L\rho_l^2}}$$

with λ_s the thermal conductivity of the solid. So, fixed the opportune physic parameters, the temperature profile obtained in an example are showed in Figure 3.

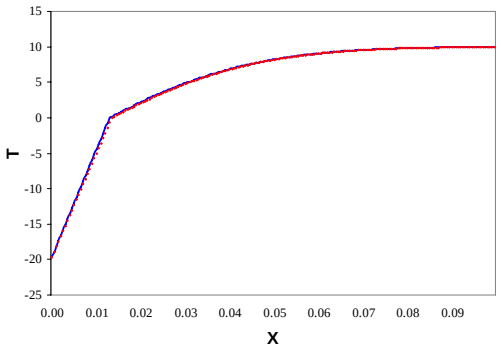

Fig. 3 - Numerical (red points) and analytical (bleu line) solution of the solidification process

References

Duff E., (1999), Fluid flow aspects of solidification modelling: simulation of low pressure die casting, Ph.D. Thesis

Jannot, Y, (2003), Transferts thermiques, http://www.librecours.org

GEODAP: A GEOPHYSICAL DATA PROCESSING TOOL FOR VOLCANOES MONITORING

*Antonino Sicali *, Filippo Greco and Rosalba Napoli*

Isitituo Nazionale di Geofisica e Vulcanologia, Sezione di Catania
** Email: sicali@ct.ingv.it*

Abstract

We designed a graphical computer program to satisfy the demand for faster processing and analysis of large volumes of diverse A modular software architecture devoted to the automated elaboration of geophysical data recorded at active volcanoes is presented. To pursue this goal, we have been developing a modular software architecture for geophysical data storage and reduction, called GEODAP (by GEOphysical DAta Processing).Our aim is To to improve the effectiveness of volcano monitoring providing a powerful environment for high-efficiency throughput of data, it is essential that data time series gathered by continuously running stations over a volcanic area are processed quickly and effectively. To pursue this goal, we have been developing an automated system for geophysical data acquisition and reduction, called GEODAP (by GEOphysical DAta Processing). It is a library of open-source software for geophysical signal processing and analysis, the detection of significant events using both classic techniques and novel methods based on statistical physics and nonlinear dynamics, the interactive display and characterization of signals, the creation of new databases, the quantitative evaluation and comparison of analysis methods, and the analysis of non-stationary processes. It currently includes databases of gravity, magnetic and self potential measurements gathered in the last ten years on Mt. Etna volcano and since 2003 on at Stromboli volcanoIsland. The combination of signal database and different analytic tools can provide the basis for reliable interdisciplinary researchresearches in active volcanic environments.

Keywords: volcano monitoring, database, gravity, magnetism, self potential, Mt. Etna.

Introduction

During the last two decades, our Laboratories of Geomagnetism (MagLab) and Gravimetry (GravLab) have been intensively monitoring the magnetic and gravity fields on Mt Etna. Significant correlations, have been observed between volcanic activity and changes both in the gravity field and in the local magnetic field, up to a few hundred of μGal and a few tens of nanoteslas, respectively (e.g.: Branca et al., 2003; Budetta and Carbone, 1998; Budetta et al., 1999; Carbone et al., 2003b, Del Negro and Currenti, 2003; Del Negro et al., 2004).

The complexity of volcanic systems and the large variety of underground processes that induce modifications of the thermodynamic state and/or stress field within the volcanic edifice, produce changes in several geophysical parameters measurable at the surface before and during the magma rise and eruption. In particular, changes in potential fields methods, (i.e. gravity and magnetic fields), have proven to be effective for volcano monitoring; indeed in some edge cases, they are the only measurable effect of the ascent of the multiphase magmatic mixture through the plumbing system of a volcano. Experiments carried out on Mt Etna over the last ten years have demonstrated the ability of discrete gravity observations to constrain the magma movements involved in the main phases of the volcano activity (Budetta and Carbone, 1998; Budetta et al., 1999; Carbone et al., 2003a). In turn, the repetition of magnetic and self potential profiles has allowed the description of the history of magmatic intrusions and lava tunnels (Del Negro and Ferrucci, 1998; Del Negro et al., 1998). Continuous measurements open the prospect of extending the observation spectral window towards phenomenology with a more rapid evolution and, therefore, of greater interest with regard to monitoring the state of activity of a volcano. (Branca et al., 2003; Carbone et al., 2003b; Carbone et al., 2006). Also the continuous magnetic observations have proved their ability to detect small changes of the local magnetic field linked to volcanic activity (e.g.: Zlotnicki and Bof, 1998; Del Negro and Ferrucci, 1998; Del Negro and Currenti, 2003; Del Negro et al., 2004). These techniques are now useful to give more complete information on the state of a volcano.

Detection of clear geophysical signals associated with the renewal of the volcanic

activity has led to an increase in the potential fields monitoring of Mt Etna. Since 1998 continuously running gravity stations and a permanent magnetic array have been installed at Etna (Del Negro et al., 2002), and from the beginning of 2003, the potential fields monitoring of Stromboli Island also began. It is now possible to gather large volumes of gravity, magnetic and self potential data of the highest achievable quality distributed over both volcanoes. With the aim of managing and analyzing in near-real-time the huge amount of multi-disciplinary data-sets, a graphic user interface based application, called GEODAP (GEOphysical DAta Processing), was implemented and adopted. The software, designed under Visual C++, is characterized by high automation level and development flexibility. It is able to exploit the entire available information coming from remote stations of monitoring networks by means of query, visualization and analysis tools. In particular, as a first step time-series data collected at different intervals or periods, were unified in a common, four-dimensional representation of space and time. As a second step, the main module containing a set of analysis routines for reduction and evaluation of the incoming data produce interpretable parameters and store the data in permanent files. Finally, the results of the analysis may be integrated to provide an estimate on the state of volcano. In this view GEODAP, represents a useful tool to facilitate scientific research on volcanic processes and phenomena, and improve the efficiency of volcanic monitoring.

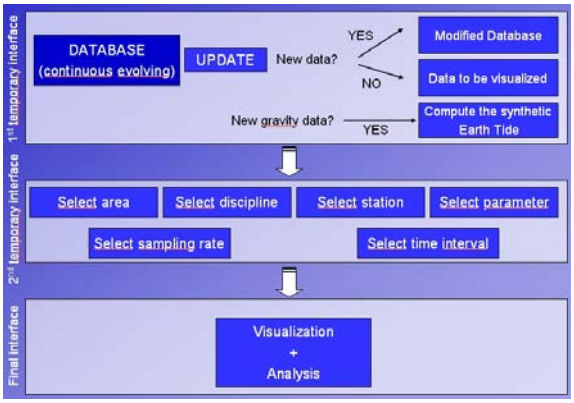

Figure 1 - Simplified flow chart of GEODAP representing the main architecture of the program.

Gravity and Magnetic networks

The architecture of GEODAP program has been developed taking into account the specific requirements of our permanent networks for the gravity and magnetic monitoring of Etna volcano and Stromboli Island (Fig. 1). At present, the monitoring system working at Etna consists of 3 gravity remote stations, an array of 7 scalar magnetometers and 3 magnetic gradiometers, and 4 stations for measuring self-potential (SP) signals. Sites are located at elevations ranging between 1700 and 3000 m a.s.l. along a North-South profile crossing the summit craters. At Stromboli Island we have been operating a network of 3 magnetic gradiometers, 1 gravity remote station and 1 station for measuring SP signals.

All the continuously recording stations were devised using innovative technologies which guarantee uninterrupted working under harsh environmental conditions. The gravity stations are equipped with LaCoste and Romberg (L&R) spring gravimeters, featuring analog feedback systems. Data are recorded at 1 datum/min sampling rate through a CR10X Campbell Scientific datalogger. The magnetic stations are equipped with a GSM-90 Overhauser effect magnetometer (0.01 nT sensitivity). Each station synchronously samples the Earth's magnetic field every 5 seconds. A Global Positioning System (GPS) receiver controls the synchronization of readings. The continuously recording electrical stations were installed at the same sites of magnetic stations. At each station five Pb- PbCl2 pipe non-polarizing electrodes are buried at 0.5 m depth. The measuring dipoles, 50 and 100 m long, are orthogonally oriented along NS and EW directions. By this dipole arrangement, noise from electrode instability, rainfall and nearby sources can be estimated. Simultaneously with gravity and magnetic signals, at each station atmospheric and ground temperature, pressure and humidity are also acquired. The data transmission is based on mobile phones and wireless systems, and automatically sends data from the acquisition systems at regular intervals to a remote computer for safe storage and analysis.

All sites sample synchronously every 10 sec and transmit data via mobile phone to the Catania Section where these data are processed and analyzed

In the following we investigate the magnetic time series collected from January 2000 to December 2002 at three selected stations: PDN, near summit craters; DGL, on the north flank, and CSR, the remote reference (Figure 1).

GEOphysical DAta Processing (GEODAP)

Such dataset is extremely heterogeneous, and handling a series of different binary data formats, sampling frequencies, resolutions, etc., becomes a key issue. Visualizing these data on a common time base is critical to interpreting them correctly and reacting suitably to possible geophysical changes. Furthermore, the need for storing additional information describing the time

series could arise; therefore, a database has been designed and implemented. It greatly simplifies the organization of the different files containing the gravity, magnetic and SP time series gathered by the real-time monitoring networks set in the field, as well as some other important parameters (such as: temperature, pressure, humidity, Kp index, etc.) that may severely influence geophysical signals making the detection of volcanic source effects more difficult (Carbone et al., 2003b; Del Negro et al., 2004). Simple command line interfaces allow for the input of geophysical data of heterogeneous formats and descriptions through one input text file, following a prescribed syntax. For each instrument, and for each measurement, a string that contains information concerning that particular data channel can be maintained. For each installation of a new instrument, a string can be added in the file, containing information about the volcano where the data are recorded, the station and the specific data channel used, measurements accuracy and the location of the sensors. All the available information, which is continuously updated, is geographically referenced and visualized on a local DEM with a distance between the grid points in N-S and E-W direction of 25 m (Fig. 2). Once entered into the database, the geophysical data and the other parameters can easily be queried, visualized and exported. A graphic interface allows the user to consult the database content and retrieve available data using geographical and thematic requests. After submitting the query, a list of matching data is loaded into the browser window, offering to export data in a text file. The export dataset is created at run time (Fig. 3).

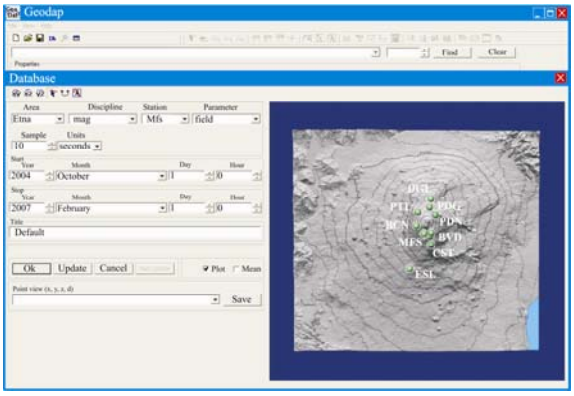

Figure 2 – Interface of the GEODAP database that includes a local DEM for geographical reference of the continuously running stations.

An original graphic routine allows speeding up the visualization of long data series, thus to obtain a general view of the signals in a short time. It offers an immediate visual representation of different channels, even channels relative to different stations or volcanoes, for a given period. These can then be analyzed in more detail by selecting shorter and more appropriate time windows. It is possible to simultaneously apply the same analysis to them and display the raw data with the results obtained to facilitate the detection of possible anomalous behavior.

GEODAP has also been devised to upload data to a distant user immediately after acquisition and re-formatting. A client–server application with dedicated protocols was built to guarantee the access to the data from anywhere in the world (of course according to a given set of permissions). Data processed at the “distant desk” can, therefore, be downloaded a few hours later and used by the personnel in charge of the volcano forecast. The on-line availability of crude or pre-processed data to authorized users connected to a wide-area network, fosters the possibility of monitoring active volcanoes without concentrating all human resources in a single observatory. Provided that the field maintenance and support are available at the volcano observatory, such a scheme would allow special instruments to be run even without any expertise in processing and interpretation of specific data.

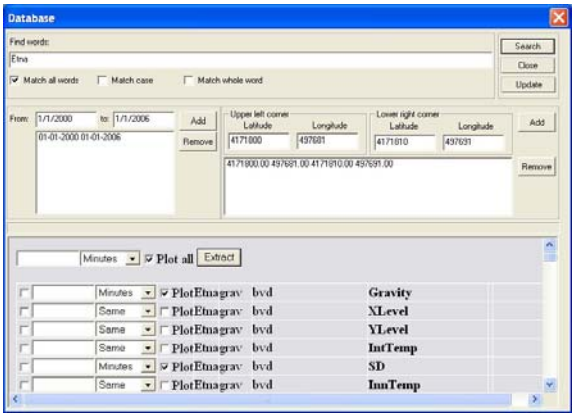

Figure 3 - Example of results for one record matching query posted to database.

At the website http://www.ct.ingv.it it is possible to examine gravity and geomagnetic observations carried out at Mt. Etna and Stromboli. Normally, in the website, the last three days reduced gravity signals observed at every station, after removal of the best linear fit and the theoretical Earth Tide, are available. Moreover, the 10-minute average of the magnetic field total intensity and the related standard deviation for each station are plotted (Fig. 4). In particular, any external users having a password are able to download directly data acquired at the stations of the gravity and magnetic networks of Mt. Etna and Stromboli.

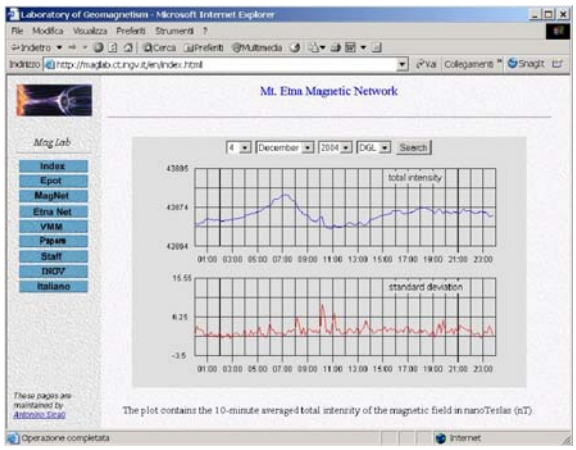

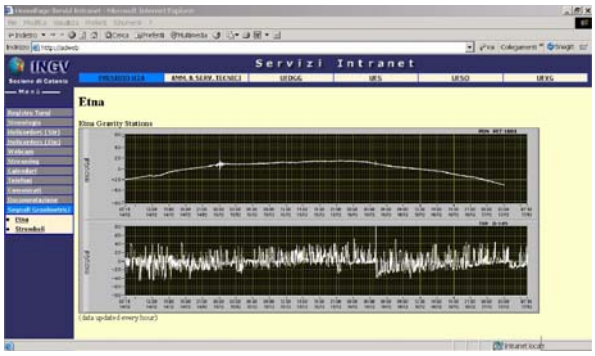

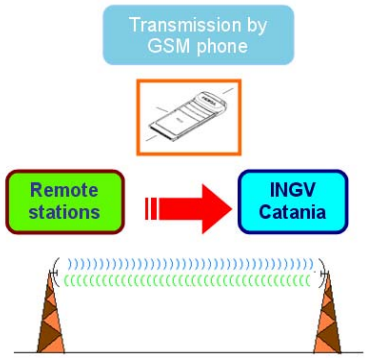

Figure 4 – A specific modulus of GEODAP, completely automated, allows the last part of the time sequences coming from the remote stations to be visualized in the INGV-CT website at the address: http://www.ct.ingv.it.

The Analysis package

GEODAP gives the possibility of browsing, plotting and downloading (e.g. to be analysed using other software) the huge amount of data coming from continuously recording remote stations, as well as, that of analyzing them. To rapidly process any time series and to detect possible volcanic changes, a powerful, comprehensive package of analysis routines for processing acquired data was developed. This package provides appropriate and reliable analysis techniques for potential fields data processing. Our application is built to be user friendly and specifically to minimize time taken in data reduction processes and improve the ability to recognize gravity, geomagnetic and SP anomalies due to geophysical sources. GEODAP is rich in statistics, regressions, linear algebra, time and frequency domain algorithms, windowing routines, and digital filters (Fig. 5). Described below are some dedicated routines available in the package.

Gravity module

Continuous gravity sequences acquired on volcanoes can be split into two main components: i) anomalies linked to the activity of the volcano itself (useful signal) and ii) signal due to tides, instrumental and meteorological effects (assumed as noise). Since the gravity raw data sets coming from a station are often affected by undesired artifacts which can corrupt the analyses, great care has been taken in designing a tool for data pre-processing. In particular, GEODAP package contains algorithms which allow, with a high automation level, to detect and correct spikes, gaps and steps on the signal under the control of the operator. It is important to stress that we can correct any kind of measurement, and not only gravity signals (e.g. meteorological variables).

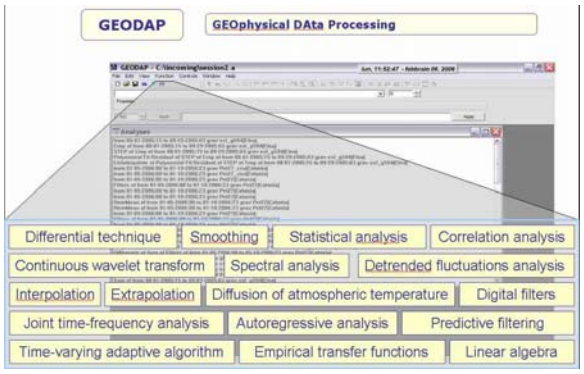

Figure 5 - Main window of the analysis module.

In order to obtain the volcano-related signal, after the pre-processing step is completed, our code allows the following operations to be accomplished: (a) correct for the Earth Tide effect, (b) correct for the instrumental drift, (c) correct the gravity effect of the tilt changes which are measured at each station along two perpendicular axes X and Y and (d) reduce the gravity effect of meteorological perturbations.

The instrumental drift is assumed to be the dominant signal over the lowest part of the spectrum and thus is modeled as the first or second degree best fit to the sequence.

The effect of Earth Tides (amplitude up to 200 μGal peak-to-peak depending on latitude, elevation and stage in the tidal cycle) is modeled

following the tidal potential catalogue from Tamura (1987). We computed the synthetic tide through the Eterna 3.30 data processing package (Wenzel, 1996), using the local tidal parameters deduced from local recordings and the Wahr-Dehant-Zschau inelastic Earth model (Dehant, 1987). The accuracies of the prediction model is within ±1%, implying tidal residuals affecting the gravity signal up to 1-2 μGal peak-to-peak over the most relevant tidal families (diurnal and semidiurnal).

The inclinometric effect is calculated using the formula (Scintrex Limited, 1992):

$$\Delta g = g(1-\cos X \cos Y)$$

where g is the average gravity value (980.6 Gal).

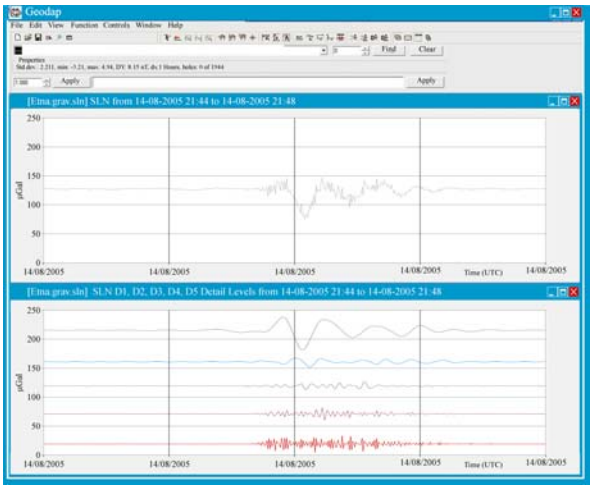

Figure 6 – Example of short-lasting (4 minutes) gravity sequence (a) and the related Wavelet multi-channel filter analysis (b).

After removing the instrumental drift, the Earth Tide effect and the tilt effect, the correlation of the residual gravity sequences with simultaneous recordings of meteorological parameters acquired at each station are analyzed. To assess reliable gravity sequences, it is crucial to measure meteorological perturbations which can affect the gravity signal at each station and to suitably remove their effect from the gravity signal. Several authors have demonstrated that meteorological parameters, especially atmospheric temperature, affect continuously running spring gravimeters. In particular, in El Wahabi et al (1997) it has been proven that, over a yearly period, temperature changes can cause up to 1 mGal instrumental effect. An admittance up to 0.2 mGal/°C, over changes with period longer than 1 month, has been evidenced in Carbone et al (2003b). To remove the effect of these perturbations is not easy given that the transfer functions are frequency-dependent and are different for each gravimeter employed. Moreover, frequency-domain filters cannot be applied to remove the effect of these perturbations since the spectrum of each component of various origins has wide intervals of superposition.

Finally, to correct the gravity signal for the influence of the atmospheric pressure produced by the combined effect of the gravitational attraction of the air column and the distortion of the Earth's surface resulting from barometric changes (Warburton and Goodkind, 1997), an algorithm that uses the standard admittance value of -0.365 μGal/mbar (Merriam, 1992) was implemented.

The package uses a tool concerning the application of the wavelet decomposition to the continuous gravity data. The advantage of analyzing a signal with wavelets is that it enables local features of the signal to be studied with a detail matching their characteristic scale. In the temporal domain, such a property allows transient signals to be represented effectively (Carrozzo et al., 2002). The "maximum compactness" or "minimum entropy" criterion, by Coifman and Wickerhauser (1993) and Fedi and Quarta (1998) applied for data compression and data analysis, respectively, are used in this tool to optimize the choice of the wavelet basis (Fig. 6).

Once the gravity signal from continuously recording stations is suitably reduced for the effect of external perturbations (which proved to be stronger by one order of magnitude than the volcanic effect), events with anomalous and/or characteristic amplitude with respect to the "normal" signal will be evidenced within different frequency bands. Possible time correlations between such anomalous items and the volcanic activity will also be tentatively evidenced to define gravity forerunners of paroxysmal eruptive episodes.

Magnetic module

Detection of volcanomagnetic events (a few nT or less) attributable to the dynamics of a volcano requires eliminating the geomagnetic field variations with no geophysical significance from measurements. To date, the most used and reliable method is the classical differential technique, based on simultaneous simple differences among the magnetic field amplitudes recorded at several points on a volcano. This technique was implemented with the option to verify the synchronization between signals recorded at different stations by cross-correlation function. We also included Steppe's (1979) method to find differences between a given station and a weighted linear combination of the remaining stations in a total field array, where the weights are determined by linear regression.

These relatively simple techniques do not allow to properly reduce the geomagnetic signal to the level of a few nanoteslas which is the apparent upper limit of detectability of magnetic anomalies associated with volcanic activity. To date, filtering geomagnetic noise is a very complex problem that involves the development of different algorithms to reduce transient fields, which could be of the same order as the volcanomagnetic signal to be detected. We were concerned with reduction of changes in the difference fields due to contrasting responses at magnetometer sites, using methods of predictive filtering, with the filters giving the relative responses between sites. Davis et al., (1981) developed the first type of approach based on Wiener's classic filters theory. The predictive analysis allows some time-intervals to be identified where important statistical variations of the signal are present. These zones are also called non-stationary zones. Considering that the phenomenology of the process is time-variant, a non-stationary approach is more appropriate to describe the physical processes tied to volcanic dynamics. For this reason, we have also been implementing an adaptive type approach (Currenti, 2004). In the non-stationary analysis all the variables are time varying. Therefore, also the weight vector of prediction will depend on time, as well as the cost function (mean squares error). The technique of analysis is based on a set of adaptive mutual predictors trained on a sliding time-window, which describes the changing statistical characteristics of the observed time series. In practice, a sliding time-window of data, input of predictor, is introduced. A time-variant vector weights each sample in order to obtain a minimization of time-variant cost function. In this way, it is easy to identify the time intervals where the predicted time series is different from the original sequence. These intervals, characterized by important statistical variations of the signal, could be associated to the periods when volcanomagnetic effects occurred.

We have observed that improvement in noise reduction can be achieved if we include magnetic vector data as input to the filter. Recently, a vector magnetometer for continuous monitoring of the inclination and declination of the Earth's magnetic field has been tested in the magnetic reference station. Thus, we added a more detailed data analysis by employing the method developed by Poehls and Jackson (1978), which relates the vector field at the reference site to the total field at the observation sites by empirical transfer functions to filter out residual variations caused by transitory fields. This method is effective in reducing the residuals associated with diurnal variations, thus allowing volcanomagnetic events, even shorter than a few days duration, to be detected. In order to distinguish between transients of volcanomagnetic origin and transients generated by strong variations in the external transitory magnetic field, we implemented the method devised by Del Negro and Ferrucci (2000), which takes into account the correlation between the measurements at two stations.

In addition to transient variations, annual components have clearly been observed in the magnetic reduced signals even when there was no significant volcanic activity. Recent and more accurate studies claim that annual variations in the geomagnetic total intensity could be caused by seasonal changes in the heterogeneous magnetization of near-surface rocks due to a diffusion of atmospheric temperature change into the ground. The intensity of the local magnetic anomaly depends on the heterogeneity of the near-surface rocks and their temperature dependence. Using the method proposed by Utada et al., (2000), the features of annual variations (ΔFT) can be quantitatively estimated by a simple one-coefficient filter as:

$$\Delta F_T(t) = h_0 \Delta T(t-t_0)$$

where ΔT is time variation in the ground temperature, h_0 is the amplitude ratio of annual changes estimated by a least squares method, and t_0 is the time lag calculated from the phase differences between total intensity and temperature.

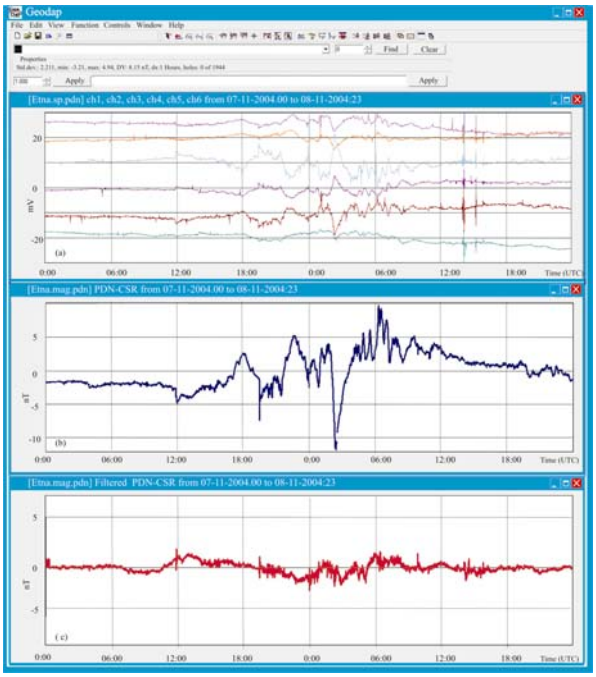

Figure 7 - (a) Self-potential data recorded at PDN station from 7 to 8 November 2004; (b) Total magnetic intensity at PDN with respect to CSR and (c) cleaned differences field after multichannel filtering procedure using self-potential data.

Self Potential module

Monitoring SP anomalies can be an efficient method for describing evolution of hydrothermal activity, changes in ground water circulation and magma displacement (Zlotnicki and Nishida, 2003). Self Potential (SP) anomalies, up to some hundreds of mV, are associated with volcanic activities.

If we assume the process to be time-variant, a non-stationary approach is required to describe the natural SP fluctuations. For this reason we implemented a predictive type approach that allows estimating important time-varying parameters. The technique was already successfully tested for magnetic data and allows identifying the possible electromagnetic changes which can occur during seismic and volcanic events.

Moreover, joint magnetic and self-potential measurements can be useful to distinguish the different magnetic effects with the same time scale, in particular electrokinetic phenomena from those due to piezomagnetic sources, associated to volcanic activity. A good time correlation between electrical and magnetic signals could indicate the presence of electrokinetic sources.

A marked correlation between the SP and magnetic signals can also appear during magnetic storms (Fig. 7). The origin of self potential temporal variations could be explained by atmospheric electrical variations (namely, the normal electric field and the induced telluric field). During a magnetic storm, electric signals are clearly dominated by magneto-telluric induction phenomena.

The amplitude of electrical signals is controlled by the shallow resistivity structure, which tends to deflect the induced current lines in a direction perpendicular to the main conductivity contrasts. The magnitude of these effects is in the range of 20 mV for electrical signals and in the range of tens of nanotesla for magnetic data. To remove this kind of temporal variation, magnetic measurements and electrical measurements need to be combined. Reduction for these induced variations can be accomplished by filtering the magnetic data with specific filters based on the self-potential data recorded nearby the magnetic stations. In Figure 7 is shown an example of the residual components obtained after the filtering procedure. It is worth noting that the variations in the magnetic data induced from the external geomagnetic field are successfully reduced.

Denoising techniques

In general, one of the main problems of signal analysis is to discriminate between the components of the signal related to the volcano activity from variations due to noise sources (i.e. meteorological variables). The presence of non-volcanic changes, indeed, not only makes signal detection more difficult but may also lead to misinterpret data. For volcano monitoring purposes it is necessary, therefore, to reduce the effects of these perturbations. Therefore, we have been developing two different approaches for denoising geophysical time series (Del Negro et al., submitted). The first one is a nonlinear autoregressive model based on the application of an Adaptive Neuro-Fuzzy Inference System (ANFIS), whose intrinsic learning features seem to be particularly suitable for such a task. The latter is a method obtained by combining wavelet transform and Independent Component Analysis (ICA), which is able to separate multiple data series into independent data series.

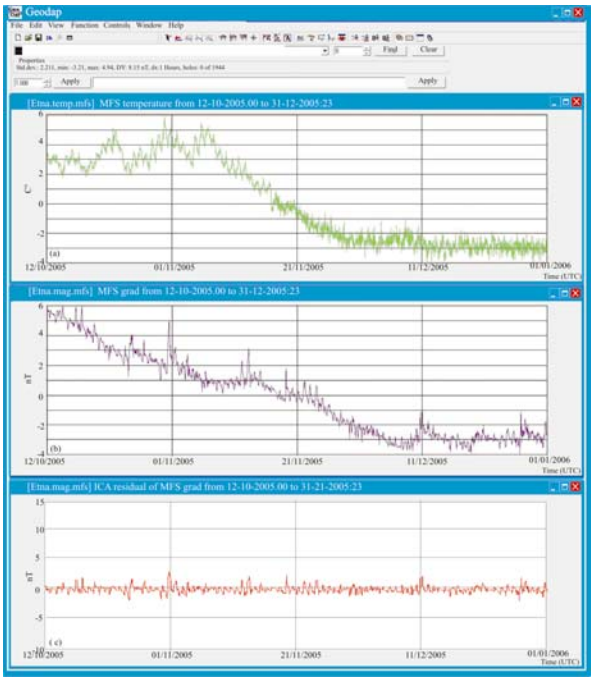

Figure 8 - Reducing of the temperature effect by ICA from magnetic data recorded at MFS gradiometric station from October to December 2005. (a) Temperature recorded at MFS station; (b) Magnetic field gradient at MFS and (c) residual estimated by ICA approach.

Both approaches may be applied to gravity, geomagnetic and self potential data (Fig. 8) when traditional filtering techniques provide unsatisfactory results. These approaches are capable of finding and effectively representing the underlying factors or sources, and allow local features of the signal to be detected. This is an important chance since the gravity and geomagnetic signals could include volcanic effects with a wide range of evolution rates.

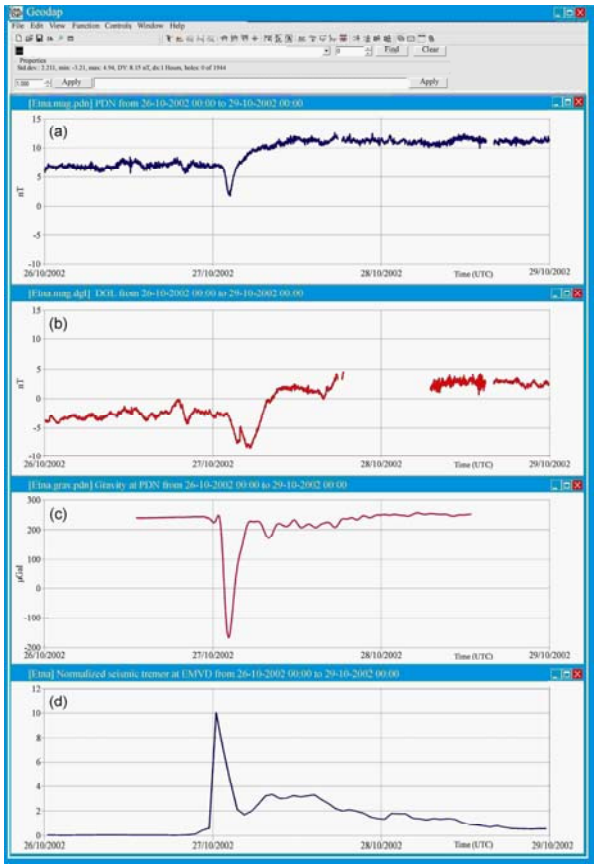

Figure 9 - Example of multi-disciplinary data-sets recorded during 26/10/2002-29/10/2002 period encompassing the start of the 2002 NE-Rift eruption. The local magnetic field at PDN and DGL stations are shown in (a) and (b) respectively. Magnetic variation of about 4–5 nT was associated with October 26 seismic swarm, while a step-like variation of 9–10 nT was observed on October 27 at the same time of the eruptive fissures opening up. A marked gravity decrease (about 400 μGal in less than one hour) observed at PDN station (c) about 4 hours before lava was first emitted from the eruptive fissures along the NE-Rift (the anomaly reversed soon afterward at a high rate). Normalized seismic tremor observed at EMVD seismic station (d).

Discussion and Conclusion

The computer-based system GEODAP was designed and implemented for geophysical monitoring of active volcanoes. The system is intended to solve the problem of monitoring the volcano at large distances from the local observatory, with the requirement of providing an estimate of the level of geophysical activity. GEODAP is an example of the rapidly growing technologies involved in managing geophysical data. The integration of different geophysical data requires the building of spatio-temporal databases. The unified representation of geophysical information is based on a structural organization of different available datasets. It affords the problems to correlate huge amounts and variety of data acquired in volcanic areas. When studying a system as complex as a volcano, to be able to simplify it without losing relevant information is crucial. GEODAP is a modular structure using physical building blocks that allow the global problem to be split into smaller and easier sub-problems, each solved within a single module. The multi-resolution approach allows data with diverse characteristics to be elaborated effectively. A variety of blocks with different procedures, depending on the nature of available data, were implemented. In particular, both traditional elaboration procedures and innovative ones were used. The flexibility of the proposed structure allows both changes to the current modules and implementation of new modules to be easily performed. This architecture will avoid dispersion in human resources and will drastically decrease the time response to visualize and analyze time series gathered by the real-time monitoring networks set on the field.

The construction of a database containing datasets of gravity, magnetic and SP measurements, and other data will make it possible to carry out multi-faceted studies of the volcanic activity. The intensified coupling of these geophysical fields, indeed, is not restricted to the handing over of data during the evaluation process, but it can lead to the integration of both data and methods and thus achieve a substantial scientific advantage. Indeed, the joint use of this information provides, through the detection of phenomena with a wide range of evolution rates, both substantial improvements in the knowledge of the dynamics of the shallow plumbing system of the volcano and the identification of any possible transient before and during volcanic eruptions.

As an example of the joint use of different geophysical parameters, Figure 9 shows the simultaneous changes of magnetic field, gravity and seismic tremor during a period encompassing the 2002-03 Etna eruption. The joint interpretation of these variations allowed the timing of the intrusive event to be described in greater detail but also permitted some constraints to be set on the characteristics of propagation of a shallow dike (Branca et al., 2003; Del Negro et al., 2004).

Finally, we are also developing the further module which aims to achieve the best possible methodology to compare the calculated parameters with prescribed limits and subsequently activate a warning signal if the limits are exceeded. The automation process also requires the results of the analyses to be integrated to provide an estimate on the state of volcano.

References

Branca, S., D. Carbone and F. Greco (2003): Intrusive mechanism of the 2002 NE-Rift eruption at Mt. Etna (Italy) inferred through continuous microgravity data and volcanological evidences, Geoph. Res. Lett., 30, 20, 2077, 10.1029/2003GL018250.

Budetta, G. and D. Carbone (1998): Temporal variations in gravity at Mt Etna (Italy) associated with the 1989 and 1991 eruptions, Bull. Volcanol., 59, 311-326.

Budetta, G., D. Carbone and F. Greco (1999): Subsurface mass redistributions at Mount Etna (Italy) during the 1995-96 explosive activity detected by microgravity studies, Geoph. J. Int., 138, 77-88.

Carbone, D., G. Budetta and F. Greco (2003a): Bulk processes some months before the start of the 2001 Mt. Etna eruption, evidenced through microgravity studies, J. Geoph. Res., 108, B12, 2556, 10.1029/2003JB002542.

Carbone, D., G. Budetta, F. Greco and H. Rymer (2003b): Combined discrete and continuous gravity observations at Mt. Etna, J. Volcanol. Geotherm. Res., 123, 123–135.

Carbone, D., L. Zuccarello, G. Saccorotti and F. Greco (2006): Analysis of simultaneous gravity and tremor anomalies observed during the 2002– 2003 Etna eruption, Earth Planet. Sci. Lett., 245, 616– 629.

Carrozzo, M.T., R. De Franco, L. De Luca, D. Luzio, R. Primiceri, T. Quarta and M. Vitale (2002): Wavelet correlation filter for wide-angle seismic data, Geophysical Prospecting, 2002, 50, 547-564.

Coifman, R.R. and M.V. Wickerhauser (1993): Wavelets and adapted waveform analysis. A toolkit for signal processing and numerical analysis, Proceedings of Symposia in Applied Mathematics, 47, 119-145.

Currenti, G. (2004): An Emerging Strategy for Magnetic Data Complex Processing in Volcanic Monitoring Networks, PhD Thesis, University of Catania, pp. 179.

Davis, P. M., D.D. Jackson, C.A. Searls and R. L. Mcphernon (1981): Detection of tectonomagnetic events using multichannel predictive filtering, J. Geophys. Res., 86, 1731-1737.

Dehant, V. (1987): Tidal parameters for an inelastic Earth, Phys. Earth Planet. Inter., 49, 97–116.

Del Negro, C. and F. Ferrucci (1998): Magnetic history of a dyke on Mt. Etna, Geophysical Journal International, 133, 451-458.

Del Negro, C., R. Di Maio, F. Ferrucci and D. Patella (1998): Magmatic intrusion determined from self-potential and magnetic measurements at Mt. Etna, Proceedings of the second workshop on European Laboratory Volcanoes - Santorini, Greece 2-4 Maggio 1996, 403-414.

Del Negro, C. and F. Ferrucci (2000): Volcanomagnetic effects at Vulcano Island (Aeolian archipelago, Italy), Geophysical Journal International, 140, 83-94.

Del Negro, C., R. Napoli and A. Sicali (2002): Automated system for magnetic monitoring of active volcanoes, Bull. Volcanol., 64, 94-99.

Del Negro, C. and G. Currenti (2003): Volcanomagnetic signals associated with the 2001 flank eruption of Mt. Etna (Italy), Geophys. Res. Letters., 30 (7), 1357.

Del Negro, C., G. Currenti, R. Napoli and A. Vicari (2004): Volcanomagnetic changes accompanying the onset of the 2002-2003 eruption of Mt. Etna (Italy), Earth and Planetary Science Letter, 229, 1-14.

Del Negro, C., F. Greco, R. Napoli and G. Nunnari: Denoising gravity and geomagnetic signals from Etna volcano (Italy), J. Volcanol. Geotherm. Res., submitted.

El Wahabi, A., B. Ducarme, B., M. Vvan Ruymbeke, N. D'oreyè and A. Somerhausen (1997): Continuous gravity observations at Mount Etna (Sicily) and Correlations between temperature and gravimetric records, Cahiers du Centre Européen de Géodynamique et de Séismologie, 14, 105-119.

Fedi, M. and T. Quarta (1998): Wavelet analysis for the regional residual and local separation of the potential field anomalies, Geophysical Prospecting, 46, 507-525.

Merriam, J.B. (1992): Atmospheric pressure and gravity, Geoph. J. Int., 109, 488-500.

POEHLS, K.A., and D.D. JACKSON (1978): Tectonomagnetic event detection using empirical transfer functions, J. Geophys. Res., 83, B10, 4933-4940.

Scintrex Limited (1992): Autograv Operator Manual Version 4.4, Concord, Ontario (Canada).

Steppe, J. A. (1979): Reducing noise in tectonomagnetic experiments by linear regression, J. Geophys. Res., 84, B6, 3063-3067.

Tamura, Y. (1987): A harmonic development of the tide-generating potential, Bull. Inf. Marees Terrestres, 99, 6813–6855.

Utada, H., M. Neki and T. Kagiyama (2000): A study of annual variations in geomagnetic total intensity with special attention to detecting volcanomagnetic signals, Earth Planets Space, 52, 91-103.

WARBURTON, R.J. and J.M. GOODKIND (1997): The influence of barometric–pressure variations on gravity, Geophys. J. R. Astron. Soc., 48, 281-292.

Wenzel, H.G. (1996): The nanogal software: Earth tide data processing package ETERNA 3.30, Bull. Inf. Marees Terrestres, 124, 9425–9439.

Zlotnicki, J. and M. Bof (1998): Volcanomagnetic signals associated with the quasi-continuous activity of the andesitic Merapi volcano, Inodonesia: 1990-1995, Physics of the Earth and Planetary Interiors, 105, 119-130.

Zlotnicki, J. and Y. Nishida (2003): Review on morphological insights of self-potential anomalies on volcanoes. Surveys in Geophysics, 24, 291–338.

GEOFIM: A TOOL FOR GEOPHYSICAL FORWARD AND INVERSE MODELING

*Salvatore Giudice * and Gilda Currenti*

Isitituo Nazionale di Geofisica e Vulcanologia, Sezione di Catania
** Email: giudice@ct.ingv.it*

Abstract

The possibility of defining one or more volcanic sources able to trigger anomalies over different geophysical signals is one of the most challenging issues facing scientists involved in the study and monitoring of active volcanoes. In order to allow the operators to handle a multiple dataset we developed software featuring a user-friendly graphical interface, called GEOFIM (GEOphysical Forward / Inverse Modeling). GEOFIM performs a real-time calculation of the ground deformation, gravity and geomagnetic anomalies generated by a given volcanic source, and allow the user to choose among five different models for every source. Furthermore, the effects due to up to ten sources can be combined in real time into a single result. These features make possible a trial and error inversion of the geophysical data by simply moving some sliders, each controlling a given source parameter. Different medium parameters can also be set. It is also possible to delegate the inversion process to a Genetic Algorithm (GA). In this case, one or more source parameters are fixed, while the others are searched by the GA within a range which is set by the operator on the grounds of geophysical and volcanological constraints. We have implemented the Non-dominated Sorting Genetic Algorithm, (NSGA-II). This choice is due to the fact that NSGA-II can take into account many objective functions at the same time, providing a family of solutions which forms the "Pareto front". So when two or three among ground deformation, gravity and geomagnetic dataset are available for the same period, NSGA-II tries to minimize the misfit between observed and calculated data for all the datasets. GEOFIM includes a graphical representation of the 2D/3D Pareto front and a cursor is placed upon it in order to select every solution belonging to the Pareto front. So, the user can navigate the Pareto front seeing at the same time solution parameters and fitness for each objective function, that is to say misfit for every dataset considered. This allows the user to choose the solution that best fits the available datasets. The selected solution can be immediately transferred to the trial and error module, allowing a real-time comparison between observed and calculated values.

Keywords: forward model, inverse model, gravity data, magnetic data, Genetic Algorithm.

Introduction

One of the most challenging issues in understanding geophysical fenomena is given by the quest for one or more volcanic sources capable of justifying volcanic anomalies shown by monitoring networks (Geophysical Inverse Problem). It's clear that a huge improvement in performing this task is achieved when informations coming from different kinds of data (for example gravity, deformation and geomagnetic data) are taken into account at the same time (Joint Interpretation of Geophysical Data). GEOFIM (GEOphysical Forward / Inverse Modeling) is a software featuring a user-friendly graphical interface, designed to help the user to visualize and invert (by trial and errors or through a genetic algorithm) datasets made up by deformation, gravity and geomagnetic data.

Coordinate system and source models

GEOFIM performs a real-time calculation of the anomalies generated by a volcanic source, allowing the user to choose among five different models for every source and to superimpose the effects of up to ten sources at the same time. The following coordinate system is adopted:

X points towards the geographic North
Y points towards the geographic East
Z is positive downward

as shown in the Fig. 1.

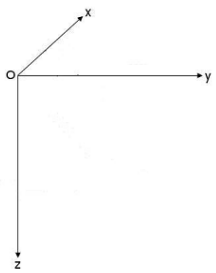

Fig. 1 – Coordinate system in GEOFIM.

Volcanic source models included in GEOFIM are Mogi, Fault, Thermal Sphere, Prism and Prolate Ellipsoid. A general assumption is that earth's crust is an ideal homogeneous half-space. For each model a short description, a schematic representation and a referement to analytical formulations used as computational routines are given.

Mogi Model

The anomaly is caused by a spherical source pressurized hydrostatically from the inside. Even though this is a simple model, it has proven to be useful in many cases. For example, it provides an effective way to represent a magma reservoir (Fig. 2):

- Deformation Mogi Model by Mogi (1958)
- Gravity Mogi Model by Sasai (1986)
- Piezomagnetic Mogi Model by Sasai (1986)

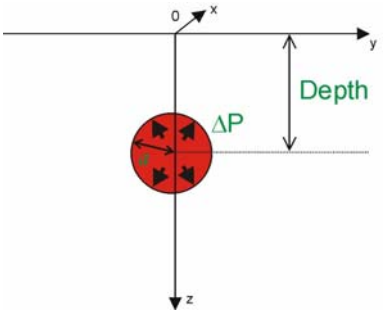

Fig. 2 – Mogi model schematic representation.

Fault Model

A fault is a crack in the rock where the two neighboring parts slip each other so that at the end they are shifted. There are three possible slip ways: dip-slip, strike-slip and tensile (Fig. 3).

- Deformation Fault Model by Okada (1992)
- Gravity Fault Model by Okubo (1992)
- Piezomagnetic Fault Model by Utsugi et al. (2000)
- Electrokinetic Fault Model by Murakami (1989)

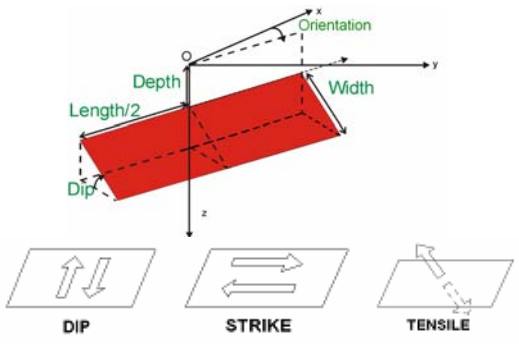

Fig. 3 – Fault model schematic representation.

Thermal Sphere Model

Thermal Sphere is a spherical source which has a magnetization and a density contrast respect to the surrounding medium. So it causes an anomaly (Fig. 4).

- Gravity Thermal Sphere Model by Blakely (1996)
- Termomagnetic Thermal Sphere Model by Blakely (1996)

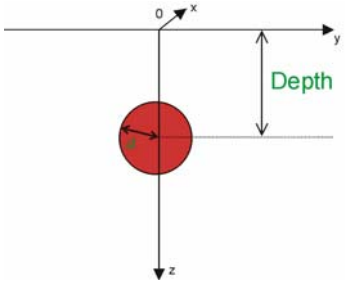

Fig. 4 – Thermal sphere model schematic representation.

Prism Model

Unlike fault, that is a 2-D source, Prism is a 3-D source. It can be useful, for example, in modeling dyke intrusions (Fig. 5).

- Gravity Prism Model by Okubo (1989)
- Termomagnetic Prism Model by Blakely (1996)

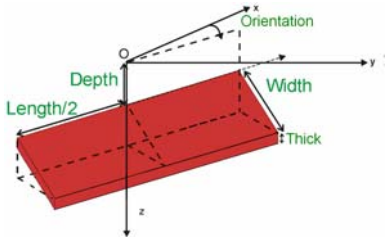

Fig. 5 – Prism model schematic representation.

Prolate Ellipsoid Model

Prolate ellipsoid is a particular restriction applied to the generic triaxial ellipsoid. While in triaxial ellipsoid the three axes may assume different values, in prolate ellipsoid two axes have the same length, and their size is smaller compared to the third one. For this reason his geometry is suitable in order to represent both compact and extended sources (Fig. 6).

- Deformation Ellipsoid Model by Yang and Davis (1988)
- Gravity Ellipsoid Model by Clark et al. (1986)
- Termomagnetic Ellipsoid Model by Clarket al. (1986)

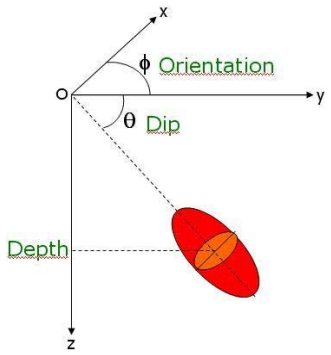

Fig. 6 – Prolate ellipsoid model schematic representation.

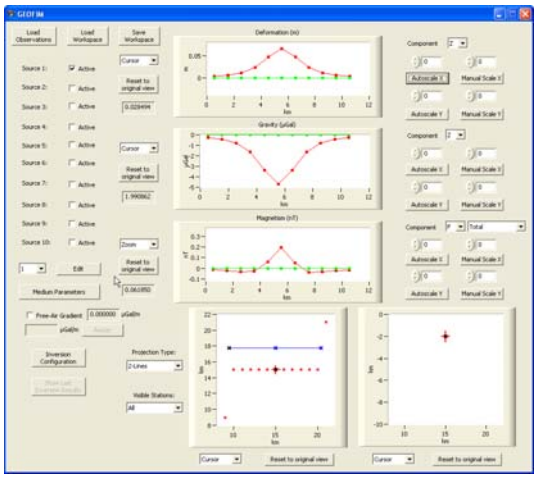

Fig. 7 – GEOFIM forward modeling main window.

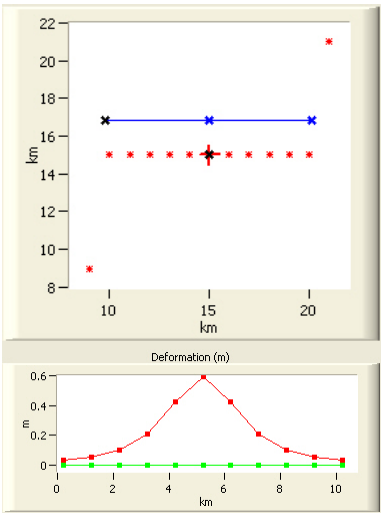

Fig. 8 – Projection on a profile: values at corner points are not shown.

GEOFIM main features

GEOFIM was developed using Microsoft Visual Studio .NET 2003 Enterprise Architect, to be more precise it's a Visual C++/MFC application. Sliders and Visualization Objects are taken from Measurement Studio 7.1 by National Instruments. The Fig. 7 shows GEOFIM main window.

After running the program, two basic operation can be performed, load an observations file or load a previously saved workspace. Observations files are quite simple because they are plain text files in which there's just to write how many deformations, gravity and geomagnetic observation are available. Moreover the following information must be provided:

1) for deformation data, station coordinates and X,Y and Z deformation components,
2) for gravity data, station coordinates and X,Y and Z gravity components,
3) for magnetism, station coordinates, X,Y, and Z magnetic components, F (total field).

Projection on a profile

The Fig. 8 shows how the projection on a profile is done. The upper Fig. 8 shows observation points (red asterisks) and the 2-arms polyline upon which projection is performed (in blue). The black cross on the left of the profile indicates profile beginning, the blue cross in the middle is used to obtain a two-arms projection and the last blue cross is profile end. The second figure shows deformation data calculated using Mogi model. Perpendiculars from the two astherisks at the corners of the upper figure do not cross the profile, so values calculated at those observation points are not shown in the lower figure. Moving the outermost crosses observation points may be included or not, as shown in the Fig.9. Finally the general case of a projection on the 2-arms polyline is shown in Fig. 10. The fourth point from the left (fig. 10, bottom) is the calculated value for the observation point marked with a red asterisk on the bottom-left corner (Fig. 10, top).

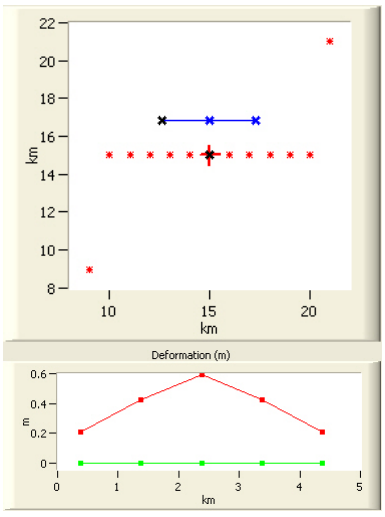

Fig. 9 – Projection on a profile: more points (the outermost ones) have been excluded from projection.

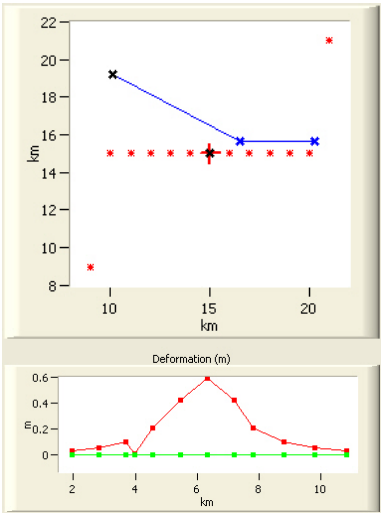

Fig. 10 – Projection on a profile: general case.

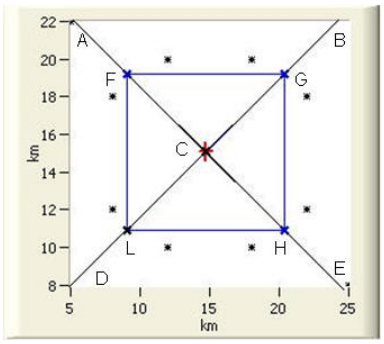

Fig. 11 – How projection on four-sided polygon works.

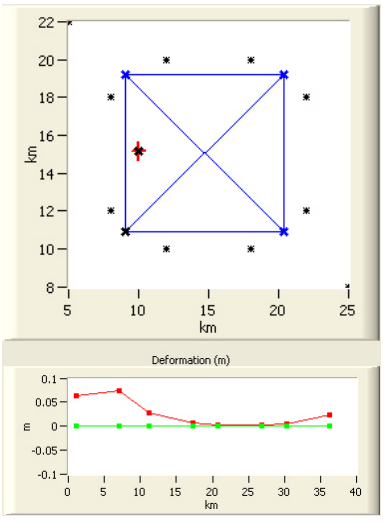

Fig. 12 – Projection on a four sided polygon: source is on the left.

Projection on four-sided polygon

Projection on a four-sided polygon is performed clockwise starting from the black cross marked as "L" (Fig. 11). Observation points in the ACD triangle having perpendicular crossing the FL segment are projected first. Then, observation points in the ACB triangle having perpendicular crossing the FG segment are projected and so on. The Figs. 12, 13, 14 and 15, which differ only for source position, give a better explanation.

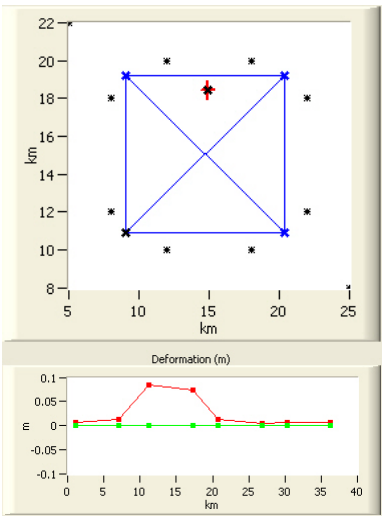

Fig. 13 - Projection on a four sided polygon: source is on top.

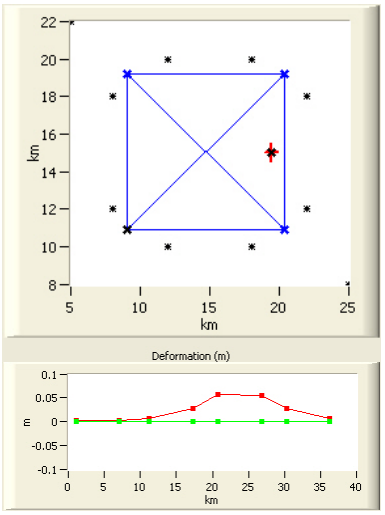

Fig. 14 - Projection on a four sided polygon: source is on the right.

Medium parameters setup

GEOFIM offers a dedicated window in order to set every Elastic, Electrokinetic and Magnetic parameter involved in computational routines, as shown in Fig. 16.

Visible stations selection

GEOFIM allows the user to show just one kind of stations or two or all stations available, by selecting this in the combo box (Fig. 17). In Fig. 18, first only deformation stations (black

asterisks), second only gravity stations (green asterisks), third all stations are visible.

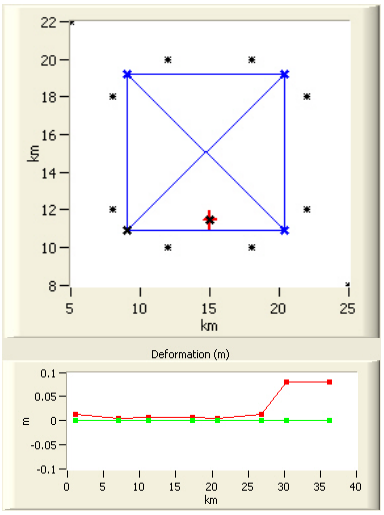

Fig. 15 - Projection on a four sided polygon: source is on the bottom.

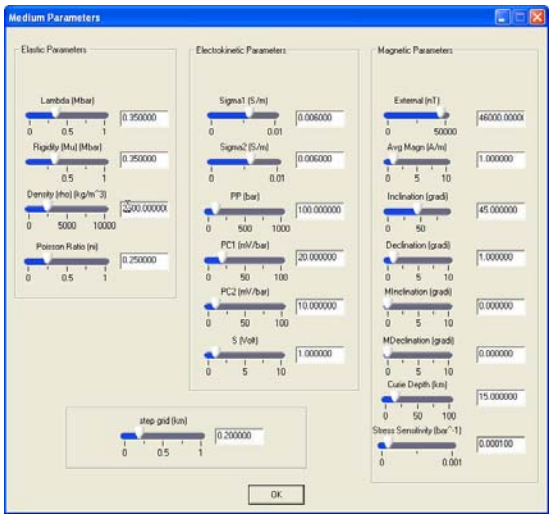

Fig. 16 – Medium parameters setup window.

Fig. 17 – Visible stations selection.

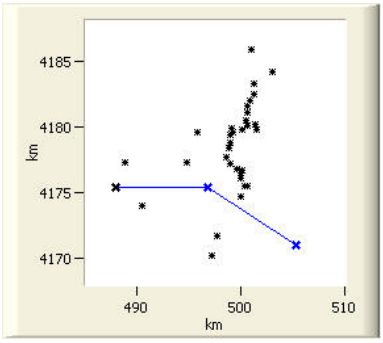

Fig. 18 – Visible station selection: only deformation stations are shown.

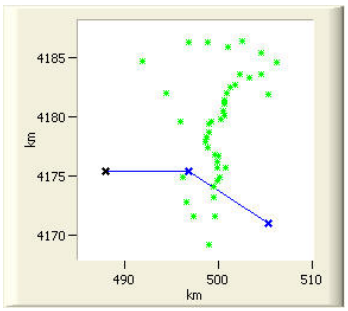

Fig. 19 - Visible station selection: only gravity stations are shown.

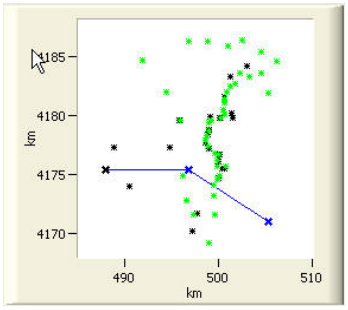

Fig. 20 - Visible station selection: both deformation and gravity stations are shown.

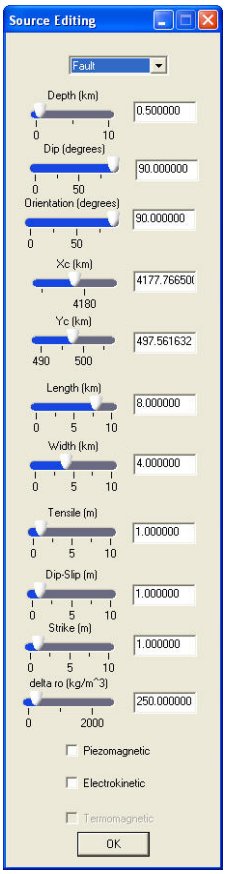

Fig. 21 – Source parameters setup can be performed using sliders or textboxes.

Source parameters setup

GEOFIM real-time calculation allows the user to have immediately an idea about how variations on a source parameter reflect on anomalies. This can be easily obtained moving the sliders. A particular value can also be entered in the textbox next to every slider. This is pretty useful for a fine-tuning when performing a trial and error inversion, or to apply a known solution that was not previously saved as a workspace. A particular attention was given to geomagnetic effects, so it's possible to calculate only piezomagnetic, electrokinetic or termomagnetic effect, as well as a combination or all the available effects.

Genetic Algorithms (GA) and NSGA-II

Genetic algorithms can be classified as non-linear, global and stochastic optimization schemes which are inspired by processes of biological evolution and genetics (Boschetti et al., 1997; Davis, 1996; Gallagher and Sambridge, 1994). Application of a genetic algorithm has several advantages over classical optimization methods. Whereas classical methods such as quasi-Newton or conjugate gradients require the calculation of derivatives (the Jacobian of the model-data mapping) as well as an appropriate

initial guess, genetic algorithms do not require these. Using derivative information, classical minimization techniques are very efficient to locate a minimum with high accuracy but at the same time are prone to be trapped in suboptimal points, that is, to fail the global minimum of a multi-modal function. Genetic algorithms, instead, represent a more global and robust approach (Rana, 1999).

The most interesting features of Genetic algorithms is that they can be adjusted to find a set of solutions to multi-objective optimization tasks (Deb, 2001; Stoffa and Sen, 1991). In particular, an approximation to the Pareto set can be obtained with the Non-dominated Sorting Genetic Algorithm NSGA-2 (Deb and Goel, 2000, Deb et al., 2000; Deb et al., 2006) with no need for linear combination of the objective function's vector components and avoiding linearization of non-linear objective functions. The Fig. 22 may be helpful to understand the way NSGA-II works.

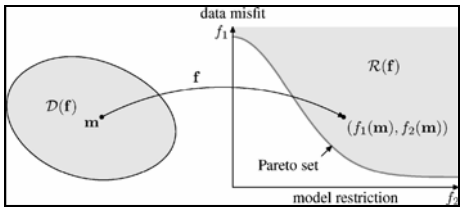

Fig. 22 – Relationship between solution space and objective space.

D(**f**) is the *solution space,* while *R*(**f**) is the *objective space*. **f** is a mapping from model space to the vector space, more precisely from the domain *D*(**f**) to the domain *R*(**f**). The main assumption upon which NSGA-II stands is that a criterion to define the comparison of vectors is established: vector $\mathbf{f}^* = (f_1^*, f_2^*, ... f_n^*)$ is said to be less than vector $\mathbf{f} = (f_1, f_2, ... f_n)$ if:

$$\mathbf{f}^* \prec \mathbf{f}, \quad if \quad \begin{cases} f_i^* \leq f_i & \text{for} \quad i = 1,...,n \\ f_i^* \prec f & \text{for at least one } i \end{cases}$$

To reduce the objective function values of a multi-objective optimization problem to a scalar fitness value, Deb *et al.* (2000) apply a scheme which sorts strings according to their degree of local non-domination. A string S_i is said to be non-dominated if its corresponding objective function $\mathbf{f}(S_i) \prec \mathbf{f}(S_j)$ for all other strings S_j, j≠i, of the considered set of strings. The Fig. 23 shows how non-domination criterion is applied.

S_i is locally non-dominated with respect to the domain *D*(**f**) since the population represents only a subset of *D*(**f**). To perform the sort, first, all non-dominated strings of the population are determined. They are given the rank '1' and called the first non-dominated set (S_2, S_3, S_6 in the figure above). This procedure is repeated for the remaining strings which are not assigned a rank, yet. Thus, rank '2' is given for the second non-dominated set (S_1 in the figure), rank '3' for the third one (S_4, S_5 in the figure), and so on until all strings are assigned a rank. In addition to the ranks assigned according to non-domination, a second, auxiliary fitness value is calculated to distinguish between individuals of the same rank and to obtain as diverse as possible solutions in model or objective function space. The auxiliary fitness is either the distance of a string to its neighbours in objective function space or to all other strings in model space. Comparing two strings, first, the ranks are considered, and second, the auxiliary fitness is used if ranks are equal. Using this procedure coupled with an elitist strategy, the genetic algorithm generates a series of local Pareto sets - local with respect to all strings considered so far - which approximate the global Pareto set increasingly well.

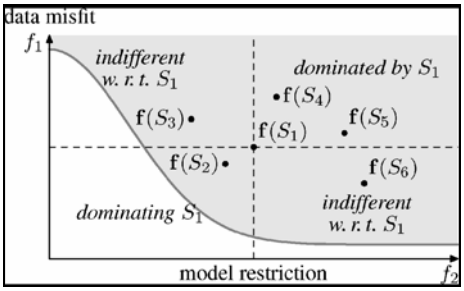

Fig. 23 – Non-domination criterion application.

NSGA-II in GEOFIM

The screenshot in Fig. 24 shows how inversion configuration is performed in GEOFIM.

First column on the left reports tipical GA parameters to be set (population size, generations number and so on), then is possible to make NSGA-II look for up to four sources whose combined effects give an explaination of the observed anomaly. For every source is possible to consider only one among deformation, gravity and magnetic effects, as well as a combination of them. Finally the following screenshot shows a 2D Pareto front.

Two buttons allow to switch from a solution belonging to the Pareto front to the next/previous one (solutions are ordered according to the misfit for one of the objective functions). At the same time, misfit between observed and calculated values for every objective function is shown as

well as solution parameters. Finally it's possible substitute the selected solution in the forward model, obtaining thus an immediate graphical comparison between observed and calculated values, projected in one of the ways above described.

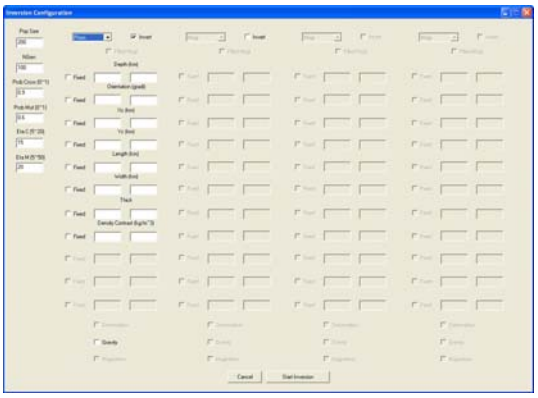

Fig. 24 – Inversion configuration window.

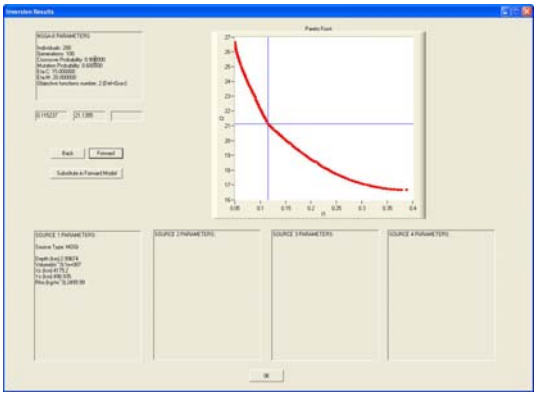

Fig. 25 – 2D Pareto front navigation window.

Conclusions

In this work we described GEOFIM, stressing above all how much his grafical interface and his graphical representation of many types of data make it an easy-to-use software. Real-time calculation and forward modeling module are powerful tools in order to perform trial and error inversions. They can be used just for educational purposes too, because of their simplicity of use.

The way NSGA-II works represents a direct approach to the non-linear and multi-objective minimization task avoiding linearizations and the choice of appropriate starting models as necessary for classical minimization methods. Moreover it offers an ensemble of different solutions to the inverse problem, giving at the same time to the operator a degree of freedom in choosing the solution that best fits according to the hierarchy he establishes among objective functions.

References

Boschetti, F., Dentith, M. & List, R., 1997. Inversion of potential field data by genetic algorithms, *Geophys. Prosp.,* 45(3), 461–478.

Davis, L., 1996. *Handbook of genetic algorithms*, International Thomson Computer Press, London.

Deb, K., 2001. *Multi-Objective Optimization Using Evolutionary Algorithms*, Wiley, Chichester.

Deb, K. & Goel, T., 2000. Controlled elitist non-dominated sorting genetic algorithms for better convergence, Tech. Rep. 2000004, Kanpur Genetic Algorithms Laboratory (KanGAL), Kanpur, India.

Deb, K., Agrawal, S., Pratap, A. & Meyerivan, T., 2000. A fast elitist nondominated sorting genetic algorithm for multi-objective optimization: NSGA-II, Tech. Rep. 2000001, Kanpur Genetic Algorithms Laboratory (KanGAL), Kanpur, India.

Deb, K., Zope, P. & Jain, A., 2002. Distributed computing of Pareto optimal solutions using multi-objective evolutionary algorithms, Tech. Rep. 2002008, Kanpur Genetic Algorithms Laboratory (KanGAL), Kanpur, India.

Gallagher, K. & Sambridge, M., 1994. Genetic algorihtms: a powerful tool for large-scale nonlinear optimization problems, *Computers & Geosciences,* 20(7/8), 1229–1236.

Parker RL 1977 Understanding inverse theory. Ann Rev Earth Planet Sci,5: 35-64.

Rana, S., 1999. Examining the role of local optima and schema processing in genetic search, *PhD thesis*, Department of Computer Science, Colorado State University, Fort Collins, Colorado.

Sambridge M 1998 Exploring multidimensional landscapes without a map. Inverse problems, 14: 427-440.

Scales, J.A. & Snieder, R., 2000. The anatomy of inverse problems, *Geophysics,* 65(6), 1708–1710.

Stoffa, P.L.&Sen, M.K., 1991. Nonlinear multiparameter optimization using genetic algorithms: inversion of plane-wave seismograms, *Geophysics,* 56(11), 1794–1810.

Tarantola A 1987 Inverse problem theory. Elsevier, Amsterdam, New York.

Kozlovskaya, E. 2001, Theory and application of joint interpretation of multimethod geophysical data, Oulu University Press.

Clark D. A., Saul S. J., Emerson D. W. 1986. Magnetic and gravity anomalies of a triaxial ellipsoid. Exploration Geophysics 17, 189-200

Okubo S., 1992. Gravity and potential changes due to shear and tensile faults in a half-space. Journal of geophysical research. Vol. 97, no. B5, pages 7137-7144.

Okubo S., Watanabe H., 1989. Gravity changes caused by a fissure eruption. Geophysical research letters, Vol. 16, No. 5.

Okada Y., 1992. Internal deformation due to shear and tensile faults in a half-space. Bulletin of the seismological society of America, Vol. 82, No. 2, pp. 1018-1040.

Murakami H., 1989. Geomagnetic Fields produced by electrokinetic sources. J. Geomag. Geoelctr. 41, 221-247

Utsugi M., Nishida Y., Sasai Y., 2000. Piezomagnetic potentials due to an inclined rectangular fault in a semi-infinite medium. Geophys. J. Int. 140, 479-492.

Sasai Y., 1986. Multiple tension-crack model for dilatancy: surface displacement, gravity and magnetic change. Bulletin of the earthquake research institute, university of Tokio, Vol. 61 pp 429-473

Sasai Y., 1984. Predominance of the Piezomagnetic effect in tectonomagnetic field of the mogi model. J. Geomag. Geoelectr., 37**,** 159-167.

Dieterich J. H., 1988. Deformation from inflation of a dipping finite prolate spheroid in an elastic half-space as a model for volcanic stressing. Journal of geophysical research, Vol. 93 No. B5, pages 4249-4257.

Mogi K., 1958. Relations between the eruptions of various volcanoes and the deformation of the ground surfaces around them. Bulletin of the earthquake research institute, Vol. 38, pp. 99-134.

ORGANIZATION

People

The researchers of *UFGM* have a diverse background and bring with them a broad range of expertise covering theory, physical modeling, inversion, and practical applications of gravity, magnetic, and electrical methods in order to track the spatial and temporal evolution of volcanic processes based on geophysical observations. The *Division* has approximately 13 regular and affiliated members (Tab. 1).

Name	Position	Email
Budetta, Gennaro	Director of Research	budetta@ct.ingv.it
Carbone, Daniele	Researcher	carbone@ct.ingv.it
Ciraudo, Alessia	Ph.D. Student	ciraudo@ct.ingv.it
Currenti, Gilda	Junior Researcher	currenti@ct.ingv.it
Del Negro, Ciro	Senior Researcher	delnegro@ct.ingv.it
Ganci, Gaetana	Ph.D. Student	ganci@ct.ingv.it
Giudice, Salvatore	Ph.D. Student	giudice@ct.ingv.it
Greco, Filippo	Technologist	greco@ct.ingv.it
Herault, Alexis	Research Associate	herault@ct.ingv.it
Napoli, Rosalba	Researcher	napoli@ct.ingv.it
Scandura Danila	Ph.D. Student	scandura@ct.ingv.it
Sicali, Antonino	Technician	sicali@ct.ingv.it
Vicari, Annamaria	Junior Researcher	vicari@ct.ingv.it

Tab. 1 - Alphabetic list of people at the UFGM.

Structure

The days where just one type of data is used to illustrate physical processes are long gone. Multiparameter data (i.e. diverse data) use is now the norm. The research in *Volcano Geophysics* is fundamentally multidisciplinary, and we employ a variety of observational, experimental, and theoretical approaches to investigate the structure and dynamics of the active volcanoes.

With the aim of achieving better planning for areas of application, the *UFGM* is organized into *Laboratories*, for guaranteeing the monitoring and training activities, and *Working Groups (WGs)*, for assuring the study and research activities (Fig. 1).

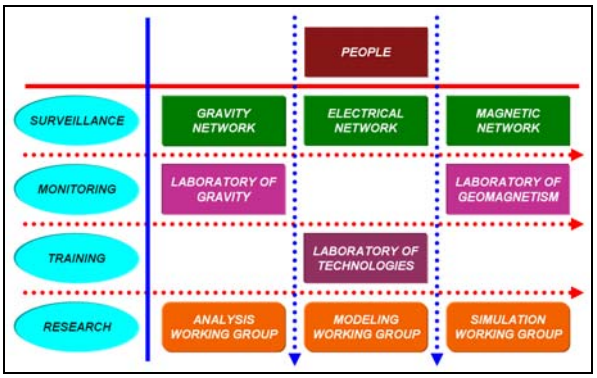

Fig. 1 – *UFGM* organization chart.

The *UFGM* makes use of the *Laboratory of Gravity* (*GravLab*) and *Laboratory of Geomagnetism* (*MagLab*), for the management of permanent networks for gravity, magnetic, and electrical monitoring of Sicilian active volcanoes, and of the *Laboratory of Technologies* (*TecnoLab*), for the scientific and technologic training of junior researchers.

Interdisciplinary research is organized into science focus areas. There are currently three active *Working Groups* devoted to: (i) Identification and characterization of precursor signals (*Analysis Working Group*); (ii) Modeling of pre-eruptive processes by using multiparameter data (*Modeling Working Group*); and (iii) Numerical simulation and hazard assessment of eruptive phenomena (*Simulation Working Group*).

The *Laboratories* and *Working Groups* are listed below in chronological order of their founding.

Laboratory of Gravimetry (GravLab)

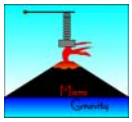

GravLab is the oldest organized laboratory within the *UFGM* established in 1986. Actually, it is mainly concerned with the possibilities of continuous measurements by spring gravimeters for monitoring active volcanoes. It is active in the development of technology for gravity monitoring in order to: (i) to establish the mid- to long-term relative stability and the accuracy of the instruments, (ii) to estimate the contribution of instrumental effects to gravity data measurements and (iii) to quantify the amplitude of the time variations of the gravity field that might be detected with such instruments. The members of the *GravLab* are:

- Filippo Greco (Chair)
- Gennaro Budetta
- Daniele Carbone

Laboratory of Geomagnetism (MagLab)

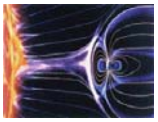

MagLab was founded in 1994 to strengthen the Institute's traditional interest in magnetic monitoring of active Sicilian volcanoes. The sectors of application include the development of methods, hardware and know-how for the automated acquisition and management of data simultaneously acquired at a variety of remote magnetic and electrical stations. To provide a basis for real-time response during eruptive events, the Laboratory designed and developed the automated system called *MagNet*. This system represents the state-of-the-art in magnetic monitoring of active volcanoes. The first application of the *MagNet* system was the permanent network for magnetic monitoring of Mt Etna. The members of the *MagLab* are:

- Rosalba Napoli (Chair)
- Salvatore Giudice
- Antonino Sicali

PhD Student	Cycle	Task	Tutor	University
Gilda Currenti	2000/2003	Multi-methodological and multi-level architecture	L. Fortuna	Engineering - University of Catania
Claudia Bonomo	2001/2004	Application of IPMC in geophysics	S. Graziani	Engineering - University of Catania
Annamaria Vicari	2002/2005	Numerical Simulation of lava flows	L. Fortuna	Engineering - University of Catania
Alexis Herault	2003/2006	Physical modeling of eruption processes	C. Paoli	Information Theory – University of Marne la Vallée, Paris XIII
Gaetana Ganci	2004/2007	Numerical modeling of interdisciplinary geophysical data	L. Fortuna	Engineering - University of Catania
Salvatore Giudice	2005/2008	Joint interpretation of multimethod geophysical data	L. Fortuna	Engineering - University of Catania
Alessia Ciraudo	2005/2008	Smoothed Particle Hydrodynamics Models	G. Russo	Mathematics - University of Catania
Danila Scandura	2006/2009	Stress interaction between magmatic intrusions and tectonic processes	G. Russo	Mathematics - University of Catania

Tab. 2 – List of Ph.D. students at the TecnoLab.

Laboratory of Technologies (TecnoLab)

TecnoLab began in May 2001 establishing a convention with the University of Catania (Electrical, Electronic and Systems Engineering Department). The Laboratory of Technologies and Dynamic Systems for the Volcanoes Geophysics (Fig. 2) bridges the gap between the experience of Earth sciences researchers and the knowledge of engineering researchers. The aim of this laboratory is to become the scientific and technical training centre of specialized people working full-time in the monitoring of active Sicilian volcanoes. Since foundation of the *TecnoLab* over twenty-five degree theses in Engineering and Earth Sciences have been completed, as well as five PhD theses in Electronic Engineering and Automation, one PhD theses in Information Theory, and two PhD theses in Mathematics have been assigned (Tab. 2).

Analysis Working Group

This *WG* is focused on the identification and characterization of precursory signals and therefore is strongly applied on the quantitative analysis of data coming from monitoring activity. Complete and long time-series of geophysical data are indeed available at Mt. Etna. An objective of this *WG* is to combine multi-disciplinary real-time data (such as seismic, geodetic, magnetic, electric, gravity, electromagnetic, resistivity) and analyze them applying methods ranging from the classical ones (i.e. cross-correlation analysis) to multivariate methods (i.e. ANFIS and ICA).

The main goals are quantification of precursors (in terms of threshold values, time-window of validity) as well as validation of precursors (in terms of number of successes, false alarms, and failed predictions). Attention is also paid to the definition of the "background level" of a given parameter, as well as the "criticality levels" that define the transition between different stages of activity of the volcano. The members of the *Analysis WG* are:

- Gennaro Budetta
- Salvatore Giudice
- Filippo Greco
- Rosalba Napoli
- Antonino Sicali

Modeling Working Group

This *WG* is devoted to the development, validation and application of theoretical models of pre-eruptive processes. The physical-mathematical models represent an effective tool to better interpret the monitoring data during pre-eruptive phases. In fact, in order to identify and interpret correctly the sources of a great variety of geophysical signals associated to volcanic activity, it is of the uttermost importance to properly model the deformation, seismic, gravity, magnetic, and electric fields, as well as their changes with time. To this aim, several advanced numerical tools are available today.

The primary goal is to develop joint models of multimethod data able to correlate the surface deformation and local potential fields to a specific source, including the perturbations due to the topography and medium elasto-visco-plastic properties. The *Modeling WG* members are:

- Daniele Carbone
- Gilda Currenti
- Gaetana Ganci
- Danila Scandura

Simulation Working Group

The mission of this *WG* is the development, validation and application of accurate and robust physico-mathematical models able to forecast the spatial and temporal evolution of the eruptive phenomena. In particular, given the most common styles of activity exhibited by Mt. Etna, the development of lava flow models has a high priority. Innovative models based on different physical formulations and approaches (deterministic versus probabilistic, Eulerian vs Lagrangian, one-dimensional versus multidimensional, homogeneous versus multiphase, etc.) have been developing and applying to real cases in order to make model inter-comparisons and more robust forecasts of the phenomena.

The overall goal is the production of tools able quantitative estimates of the lava flow hazard at Mt Etna. These include hazard maps able to identify the most dangerous areas surrounding the volcano as well as numerical forecasting simulations to be used during the crisis for the quantitative description of the phenomena. The members of the *Simulation WG* are:

- Alessia Ciraudo
- Alexis Herault
- Annamaria Vicari

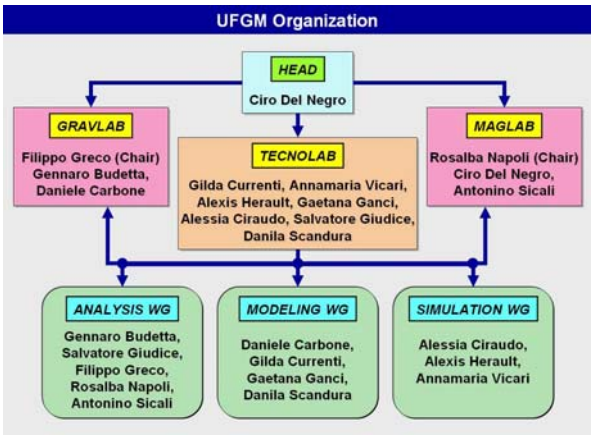

Fig. 2 – Members of *Laboratories* and *WGs* at *UFGM*.

PROJECTS

The *UFGM* is currently involved in these interdisciplinary research projects and initiatives:

VOLcanoes: Understanding subsurface mass moveMEnt (VOLUME)

The rationale behind this project is to increase our understanding of how subsurface mass movement manifests itself at the surface, in turn revealing the significance of such movements as precursors to impending eruptions. In this project, we employ and integrate seismic, gravimetric, geochemical, terrestrial and space based deformation data. We undertake joint inversions of these datasets through iterative numerical forward modeling of coupled processes (e.g. multi-phase fluid pulses with elastic wave radiation in solids; gas and temperature with ground deformation and seismicity).We will utilize existing data from permanent installations for a suite of test sites comprising different volcano types at differing times in their activity cycle.

A research project funded by *European Commission* under the *Sixth Framework Programme* (Sustainable development, global change and ecosystems FP6-2004-Global-3).

Geophysical and Volcanological Observatory of Monte Melbourne, Antartide

This multidisciplinary project represents the continuation and upgrading of monitoring and research initiatives on the Melbourne volcano, begun in 1986. In particular, the current geophysical observation systems based on 5 tilt stations and 5 seismic stations will be revised and upgraded with the aim of pursuing and notably augmenting knowledge on the geodynamics of Melbourne volcano. Moreover, 4 permanent GPS stations, 3 broad-band seismic stations, 2 magnetic stations will be set up and the 5 tilt stations operating since 1989 will undergo maintenance. The purpose of this observatory will be for geophysical and volcanological studies, but the relevance of a number of results (temperature at three levels of permafrost and GPS and geomagnetic data) is equally important for in-depth climate and atmosphere studies.

Funding is provided by the *Ministero dell'Istruzione dell'Università e della Ricerca* (*MIUR*) in the framework of the *Programma Nazionale di Ricerche in Antartide* (*PNRA*).

Project V3_6 – Etna. Research on active volcanoes, precursors, scenarios, hazard, and risk

The project focuses on the hazard assessment at Etna through the development of geophysical and geochemical techniques, the investigation of chemical and physical properties of magmas, the quantitative analysis of monitoring signals for the identification of precursors, the reconstruction of the eruptive history, and the development of physical and numerical models of pre-eruptive and eruptive processes. The variety of the project tasks has lead to the creation of a project consortium including many different expertise from a large number of research Institutes (INGV, CNR, etc.) and Universities. Therefore, the main target of this 2-year project is to make a substantial step forward in the understanding of the different behaviors and critical levels of Mt Etna and, as a consequence, in the assessment of the different hazards it poses.

Funding is provided by the *Dipartimento della Protezione Civile* (*DPC*) in the framework of the INGV-DPC Project 2005-2006.

Simulation of lava flows and associated hazard

The quantitative description of the dynamics of the eruptive phenomena requires the development, validation and application of accurate and robust physico-mathematical models able to forecast the spatial and temporal evolution of the volcanic processes. In particular, given the most common styles of activity exhibited by Mt. Etna, the development of lava flow models has a high priority. Existing and new models based on different physical formulations and approaches will be developed and applied to real cases in order to make model inter-comparisons and more robust forecasts of the phenomena. Models will also use, as much as possible, data deriving from the other tasks such as observational data, for model validation, and experimental data, for constitutive equations. This project is also aimed at the carrying out of products able to provide quantitative estimates of the lava flow hazard at Mt. Etna. These include hazard maps able to identify the most dangerous areas surrounding the volcano as well as numerical forecasting simulations to be used during the crisis for the quantitative description of the phenomena. Forecasting simulations should be used in quasi real-time in order to predict the evolution of the phenomena and their hazard on the surroundings.

A research project funded by *Regione Siciliana* in the framework of the Three-Year Programme 2006-2008 for the *Volcanological and Seismological Monitoring of Sicily*.

Consortium COMETA (COnsortium Multi agEncies for promoting and adopting Tecnhologies for Advanced computing)

The mission and task of the Consortium are the realization and management of an advanced centre of research for realizing two goals.

a) To encourage research projects and technological applications for the development of new computing high level system, of innovative systems concerning the data bank's managment, and new systems oriented to the multimedia simulations.

b) To promote the development and the dissemination of new computing technologies, especially with the adoption of the GRID;

Funding is provided by Istituto Nazionale di Fisica Nucleare (*INFN*), Istituto Nazionale di Astrofisica (*INAF*), Istituto Nazionale di Geofisica e Vulcanologia (*INGV*), *University of Catania*, *University of Messina*, *University of Palermo*, and *Consortium SCIRE*.

SOFTWARE

A main issue with our *Laboratories* and *Working Groups* is technology transfer; we are committed to delivering program packages. The objective is to shear the products of our research with the scientific community.

These packages are not the typical research programs. Instead, we take the codes generated from the research phase and further develop them into near-commercial quality software that are fully tested and documented. The included *Graphic User Interface* (GUI) enables these delivered programs to be used directly in surveillance projects without the need to integrate them into existing software.

Thus far, we have delivered the following major packages:

MADAP (MAgnetic DAta Processing)
A Program Library for Estimating and Removing Noise from Magnetic Time Series (Fig. 1).

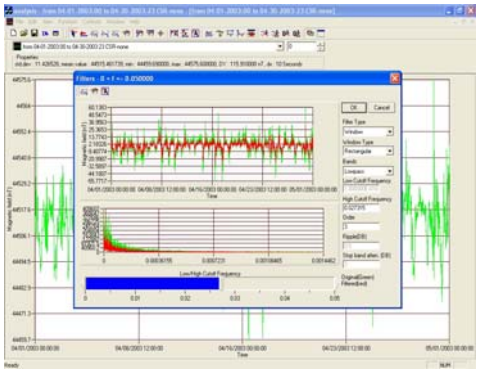

Fig. 1 – Magnetic time series analysis using MADAP.

VMM (VolcanoMagnetic Modeling)
A Program Library for Modeling Volcanomagnetic Fields.

GEODAP (GEOphysical DAta Processing)
A Program Library for Estimating and Removing Noise from different Geophysical Time Series.

GRAVERSE
A Program Library for Modeling of Gravity Data.

GRAVISUAL
A Program Library for Handling Long Gravity Time Sequences (Fig. 2).

Fig. 2 – 3D Gravimetric Inversion computed with GRAVERSE.

GEOFIM (GEOphysical Forward / Inverse Modeling).
A tool for performing a real-time calculation of the ground deformation, gravity and geomagnetic anomalies generated by different volcanic sources.

MAGFLOW
A Cellular Automata Model for Lava Flow Simulations.

HOTSAT
Automatic system to detect thermal anomalies and to compute effusion rate using satellite data (Fig. 3).

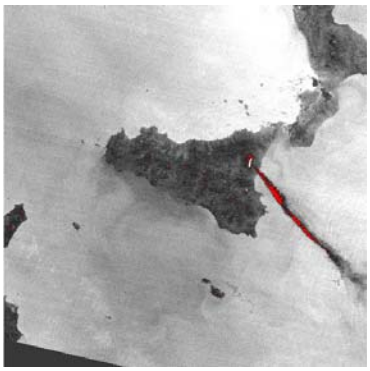

Fig. 3 – Ash path detected using HOTSAT tool.

The manual/documentation for each software package is available for download. A demo version for the *MAGFLOW* simulator software package is also available for download.

PUBLICATIONS

If you have trouble reading any of the papers or abstracts please contact greco@ct.ingv.it or napoli@ct.ingv.it and ask for a copy in a different format.

List of publications

Andò, B., Carbone, D., 2006. A new computational approach to reduce the signal from continuously recording gravimeters for the effect of atmospheric temperature. Phys. Earth Plan. Int., 159, 247–256.

Bonforte, A., Carbone, D., Greco, F., Palano, M., 2007. Intrusive mechanism of the 2002 NE-rift eruption at Mt Etna (Italy) modelled using GPS and gravity data. Geophys. J. Int., 169, 339–347.

Carbone, D., Zuccarello, L., Saccorotti, G., Greco, F. Analysis of simultaneous gravity and tremor anomalies observed during the 2002-2003 Etna eruption. Earth Plan. Sc. Lett., 245, 616–629.

Carbone, D., Budetta, G., Greco, F., Zuccarello, L., 2007. A data sequence acquired at Mt. Etna during the 2002–2003 eruption highlights the potential of continuous gravity observations as a tool to monitor and study active volcanoes. Journal of Geodynamics, 43, 320–329.

Carbone, D., Greco, F., 2007. Review of Microgravity Observations at Mt. Etna: A Powerful Tool to Monitor and Study Active Volcanoes. Pure appl. geophys.,164, 1–22.

Carbone, D., Currenti, G., Del Negro, C., 2007. Elastic model for the gravity and elevation changes prior to the 2001 eruption of Etna volcano. Bull. Volcanol., 69, 553–562

Carbone, D., Currenti, G., Del Negro, C., Multi-objective Genetic algorithm inversion of ground deformation and gravity changes spanning the 1981 eruption of Etna volcano. J. Geoph. Res. (Submitted 2006).

Carbone, D., Currenti, G., Del Negro, C., (2007). Elastic model for the gravity and elevation changes before the 2001 eruption of Etna volcano. Bull. Volcanol., 69, 553-562, DOI 10.1007/s00445-006-0090-5.

Cocchi, L., Caratori Tontini, F., Carmisciano, C., Stefanelli, P., Anzidei, M., Esposito, A., Del Negro, C., Greco, F., Napoli, R. An integrated model of Panarea Island (Aeolian Archipelago) inferred from new potential field data, Annals of Geophysics, submitted.

Currenti, G., Del Negro, C., Fortuna, L., Ganci, G. (2006). Integrated inversion of ground deformation and magnetic data at Etna volcano using a genetic algorithm technique. Annals of Geophysics, 49:6, 1325-1334.

Currenti, G., Del Negro, C., Ganci, G. (2007). Modelling of ground deformation and gravity fields using finite element method: an application to Etna volcano. Geophys. J. Int., doi: 10.1111/j.1365-246X.2007.03380.x.

Currenti, G., Del Negro, C., Johnston, M., Sasai, Y. (2007). Close temporal correspondence between geomagnetic anomalies and earthquakes during the 2002-2003 eruption of Etna volcano. J. Geophys. Res., in press.

Currenti, G., Napoli, R., Carbone, D., Del Negro, C., Ganci, G. (2007). Inverse modeling in geophysical applications. Applied and Industrial Mathematics in Italy - II, in press.

Currenti, G., Del Negro, C., Ganci, G. (2006). Finite Element Modeling of Ground Deformation and Gravity Fields at Etna Volcano, Annals of Geophysics, submitted.

Del Negro, C., Fortuna, L., Herault, A., Vicari, A. (2007). Simulations of the 2004 lava flow at Etna volcano by the MAGFLOW Cellular Automata model, Bull. Volcanol., in press.

Greco, F., Budetta, G., Carbone, D., Panepinto, S., Luzio, D. The application of a denoising method aimed at reducing continuous gravity data. Applied and Industrial Mathematics in Italy – II (Submitted 2006).

Greco, F., Carmisciano, C., Del Negro, C., Loretti, I., Sicali, S., Stefanelli, P. (2006). Seismic-induced accelerations detected by two coupled gravity meters in continuous recording with a high sampling rate at Etna volcano, Annals of Geophysics, submitted.

Herault, A., Vicari, A., Ciraudo, A., and Del Negro, C. (2007). Forecasting Lava Flow Hazard During the 2006 Etna Eruption: Using the Magflow Cellular Automata Model, Computer & Geosciences, in press.

Napoli, R., Currenti, G., Del Negro, C., (2007). Internal structure of Ustica volcanic complex (Italy) based on a 3D inversion of magnetic data. Bull. Volcanol., DOI 10.1007/s00445-007-0115-8.

Panepinto S., F. Greco F., D. Luzio, B. Ducarme (2006). An overview on wavelet multi-resolution decomposition compared with traditional frequency domain filtering for continuous gravity data denoising. Bull. Inform. Marèes Terrestres 141, 11213-11224.

Vicari, A., Herault, A., Del Negro, C.; Coltelli, M., Marsella, M., Proietti, C. (2007). Modelling of the 2001 Lava Flow at Etna Volcano by a Cellular Automata Approach, Environmental Modelling & Software, 22, 1465-1471.

Meetings attendance

Budetta G., D. Carbone, G. Currenti, C. Del Negro, F. Greco, R. Napoli, A. Sicali. The role of potential fields in imaging the intrusive mechanisms of recent eruptions on Mt Etna. Convegno MGMEESV 2006 Catania, 27-29 settembre 2006 (presentazione orale).

Budetta G., D. Carbone, G. Currenti, C. Del Negro, F. Greco, A. Herault, R. Napoli, A. Sicali, A. Vicari. Magnetic and gravity observations at Stromboli volcano. Convegno MGMEESV 2006 Catania, 27-29 settembre 2006 (poster).

Carbone, D., Currenti, G., Del Negro, C., Ganci, G., Giudice, S. (2006). Insights into the internal dynamics of active volcanoes through joint inversion of deformation and gravity data, General Assembly of the European Geophysical Society, Vienna (Austria), 02–07 April (oral presentation).

Carbone, D., Greco, F., Andò, B., Budetta, G., Del Negro, C. (2006). Continuous gravity measurements at Mt. Etna, AGU Fall Meeting, San Francisco, USA, 11-15 December (oral presentation).

Carbone, D., Currenti, G., Del Negro, C., Ganci, G., Napoli, R. (2006). Inverse Modeling in Geophysical Applications, VIII Conference SIMAI (Italian Society of Mathematics Applied to Industry), Baia Samuele (Ragusa), 22-26 May (oral presentation).

Ciraudo A., C. Del Negro, A. Herault, A. Vicari, Advances in modelling methods for lava flows simulation, SIMAI, Baia Samuele (Ragusa), 22-26 Maggio 2006.

Ciraudo, A., Del Negro, C., Vicari, A., Herault, A. (2006). Mapping of lava flows for hazard assessment, VIII Conference SIMAI (Italian Society of Mathematics Applied to Industry), Baia Samuele (Ragusa), 22-26 May (oral presentation).

Colangelo, G., Currenti, G., Del Negro, C., Lapenna, V, Napoli, R., Telesca, L. (2006). Self-potential network at Etna volcano and Stromboli Island, IAVCEI – Fourth Conference Cities on Volcanoes (COV4), Quito (Ecuador), 23-27 January (poster session).

Currenti, G., Del Negro, C., Ganci, G. (2006). Modeling of ground deformation and gravity field by using finite element method: an application to Etna volcano, Community Finite Element Models (CFEM) Workshop, Golden, CO (USA), 26-30 June (poster session).

Currenti, G., Ganci, G., Del Negro, C. (2006). Finite Element Modeling of Ground Deformation and Gravity Data Observed at Mt Etna During the 1993-1997 Inflation Phase, AGU Fall Meeting, San Francisco, USA, 11-15 December (oral presentation).

Currenti, G., Del Negro, C., Ganci, G., Williams, C. (2006). Effects of Topography and Elastic Heterogeneity in Modeling Ground Deformation for the 2002-2003 Mt Etna Eruption Using the Finite Element Method, AGU Fall Meeting, San Francisco, USA, 11-15 December (poster session).

Currenti, G., Del Negro, C., Fortuna, L., Ganci, G. (2006). Finite element modeling of potential fields induced by pressure sources: the Etna case study, General Assembly of the European Geophysical Society, Vienna (Austria), 02–07 April (poster session).

Currenti, G., Del Negro, C., Napoli, R., Sicali, A. (2006). Ground magnetic anomaly images of Ustica Island, General Assembly of the European Geophysical Society, Vienna (Austria), 02–07 April (poster session).

Del Negro, C., Vicari, A., Herault, A. (2006). Advances in modelling methods for lava flows simulation, VIII Conference SIMAI (Italian Society of Mathematics Applied to Industry), Baia Samuele (Ragusa), 22-26 May (oral presentation).

Del Negro, C., Herault, A., Vicari, A. (2006). Simulations of lava flows at Mt Etna for hazard assessment, General Assembly of the European Geophysical Society, Vienna (Austria), 02–07 April (poster session).

Del Negro, C., Herault, A., Vicari, A. (2006). Physically based modelling of lava flows at Mt. Etna, General Assembly of the European Geophysical Society, Vienna (Austria), 02–07 April (poster session).

Di Mauro, D., Del Negro, C., Masci, F., Meloni, A., Napoli, R., Palangio, P. (2006). Geomagnetic Observations in Seismic and Volcanic Areas in Italy, XII IAGA Workshop on Geomagnetic Observatory Instruments, Data Acquisition and Processing, Belsk (Poland), 19-24 June (poster session).

Ganci, G., Currenti, G., Del Negro, C., Fortuna, L. (2006). Modeling of Potential Fields by using Finite Element Method: The Etna Case Study, VIII Conference SIMAI (Italian Society of Mathematics Applied to Industry), Baia Samuele (Ragusa), 22-26 May (oral presentation).

Greco F., Napoli R., Sicali A., Currenti G., Del Negro C., Budetta G., Carbone D., Ganci G., Giudice S. A geophysical data processing tool for active volcanoes monitoring: the 2006 Etna eruption case study. Convegno Nazionale MGMEESV – Catania , 26-29 settembre 2006.

Greco F., G. Budetta, D. Carbone, S. Panepinto. The application of an denoising method aimed

at reducing continuous gravity data. VIII Congresso Società di Matematica Applicata e Industriale (SIMAI 2006). Baia Samuele (Ragusa), 22-26 Maggio 2006 (presentazione orale).

Greco F., G. Budetta, D. Carbone, C. Carmisciano, C. Del Negro, I. Loretti, A. Sicali, P. Stefanelli. Experimentation of two coupled gravity meters in continuous recording with a high sampling rate at Etna volcano Convegno MGMEESV 2006 Catania, 27-29 settembre 2006 (poster).

Greco F., G. Budetta, D. Carbone, C. Carmisciano, C. Del Negro, I. Loretti, A. Sicali, P. Stefanelli. Experimentation of two coupled gravity meters in continuous recording with a high sampling rate at Etna volcano, European Geosciences Union – General Assembly 2006 Vienna, Austria, 02 – 07 April 2006 (poster).

Herault A., C. Del Negro, A. Vicari, GIS Based tool for volcanic hazard assessment and support decision, 20th International CODATA Conference, Scientific Data and Knowledge within the Information Society, 22-25 October 2006, Beijing

Napoli R., G. Currenti, and C. Del Negro: Ground magnetic field monitoring: a lesson from 20 years experience at Mt. Etna. DEMETER International Workshop – Toulouse, June 14 – 16, 2006.

Napoli R., Del Negro C., Greco F., Nunnari G. Multivariate methods applied to gravity and geomagnetic time sequences from Etna volcano. Convegno Nazionale MGMEESV – Catania , 26-29 settembre 2006.

Napoli, R., Currenti, G., Del Negro, C., Herault, A., Sicali, A., Vicari, A. (2006). Magnetic Observations at Stromboli Volcano, XII IAGA Workshop on Geomagnetic Observatory Instruments, Data Acquisition and Processing, Belsk (Poland), 19-24 June (poster session).

Panepinto S., F. Greco, D. Luzio, B. Ducarme. An overview on wavelet multiresolution decomposition compared with traditional frequency domain filtering for continuous gravity data denoising. “Workshop on Analysis of Data from Superconducting Gravimeters and Deformation Observations regarding Geodynamic Signals and Environmental Influences”. Jena, Germany, March 27-31, 2006 (presentazione orale).

Panepinto S., F. Greco, M. van Ruymbeke, B. Ducarme, D. Luzio. Tidal Gravity Observations at Mt. Etna and Stromboli: results concerning the modeled and observed tidal factors Convegno MGMEESV 2006 Catania, 27-29 settembre 2006 (presentazione orale).

Panepinto S., F. Greco, M. van Ruymbeke, B. Ducarme, D. Luzio. Results concerning the modeled and observed tidal factors at Mt. Etna and Stromboli volcanoes (Italy), AGU Fall meeting 11–15 December 2006, San Francisco, USA (poster).

Vicari, A. Del Negro, Fortuna, L., Herault, A. (2006). Simulations of lava flow at Etna volcano using CA and SPH models, IAVCEI – Fourth Conference Cities on Volcanoes (COV4), Quito (Ecuador), 23-27 January (oral presentation).

Theses

Buscemi Giordano. Strumenti per la simulazione di flussi lavici basati su CNN, Parte II, Tesi di Laurea, Università degli Studi di Catania – Facoltà di Ingegneria, Dipartimento di Ingegneria Elettrica, Elettronica e dei Sistemi (DEES) – Corso di Laurea in Ingegneria Informatica, Relatori L. Fortuna, C. Del Negro, M. Frasca, A. Vicari, a.a. 2005-2006.

Carambia Benedetto, Tesi di Laurea, Strumenti per la simulazione di flussi lavici basati su CNN, Relatori L. Fortuna, C. Del Negro, M. Frasca, A. Vicari, a.a. 2005-2006.

Romano Roberto, Filtraggio di segnali gravimetrici, magnetici e di potenziale spontaneo mediante algoritmi wavelet e FastICA. Università degli Studi di Catania – Facoltà di Ingegneria Dipartimento di Ingegneria Elettrica, Elettronica e dei Sistemi (DEES) – Corso di Laurea in Ingegneria Informatica, pp. 149.

Saglimbene Silvana. Modelli Viscoelastici del campo piezomagnetico in aree vulcaniche, Tesi di Laurea in Ingegneria Informatica, Università di Catania, Relatori G. Nunnari, G. Currenti, C. Del Negro, a.a. 2005-2006.

Villadoro Giovanni, Filtraggio di dati geofisici in aree vulcaniche mediante tecniche neuro-fuzzy. Università degli Studi di Catania – Facoltà di Ingegneria Dipartimento di Ingegneria Elettrica, Elettronica e dei Sistemi (DEES) – Corso di Laurea in Ingegneria Informatica, pp. 164.

Coordinamento editoriale e impaginazione
Centro Editoriale Nazionale | INGV

Progetto grafico e redazionale
Laboratorio Grafica e Immagini | INGV Roma

Via di Vigna Murata, 605
00143 Roma
Tel. +39 06518601 Fax +39 065041181

http://www.ingv.it

Istituto Nazionale di Geofisica e Vulcanologia